Trapping ultracold argon atoms

Peter David Edmunds

A thesis submitted to University College London
in partial fulfilment of the requirements for the
degree of Doctor of Philosophy

Department of Physics and Astronomy
University College London
November 2014

I, Peter David Edmunds, confirm that the work presented in this thesis is my own. Where information has been derived from other sources, I confirm that this has been indicated in the thesis.

Signed .... Date ....

Abstract

This thesis describes the dipole trapping of both metastable and ground state argon atoms. Metastable argon atoms are first Doppler-cooled down to $\sim$80 μK in a magneto-optical trap (MOT) on the $4s[3/2]_2$ to $4p[5/2]_3$ transitions. These were loaded into dipole traps formed both within the focus of a high-power CO_2 laser beam and within an optical build-up cavity. The optical cavity's well depth could be rapidly modulated: allowing efficient loading of the trap, characterisation of trapped atom temperature, and reduction of intensity noise. Collisional properties of the trapped metastable atoms were studied within the cavity and the Penning and associative losses from the trap calculated.

Ground state noble gas atoms were also trapped for the first time. This was achieved by optically quenching metastable atoms to the ground state and then trapping the atoms in the cavity field. Although the ground state atoms could not be directly probed, we detected them by observing the additional collisional loss from co-trapped metastable argon atoms. This trap loss was used to determine an ultra-cold elastic cross section between the ground and metastable states. Using a type of parametric loss spectroscopy we also determined the polarisability of metastable argon at the trapping wavelength of 1064 nm.

Contents

Acknowledgments

At the time of writing, I have been at UCL for over eight (!) years. It is therefore with a sense of nostalgia that I recall events over the course of both my undergrad and postgrad years. I arrived as a fresh-faced 18 year-old and leave as a 26 year-old with slightly less hair and a slightly larger knowledge of physics. It will feel very peculiar to not come into the Gower Street campus every morning.

During this time I have met many people and made many friends, of which there are too many to mention. Special thanks must go the "vertices" Chris Perry and Naïri Usher for being there for frivolities ("balloon-ball" immediately comes to mind) and more serious activities alike ("emergency drinks" at midday in Birkbeck union). Their support has been invaluable in helping me through the darker days whenever anything in my experiment would inexplicably break.

Of course, I extend my deepest thanks to Professor Peter Barker for proposing the experiment and for having faith in me as a PhD student. His enthusiasm, support and creative solutions to experimental problems have been vital to my successes. Within the group, special thanks should be reserved for Dr. Conor Maher-McWilliams (or is that Maher-McWillams?) and Dr. Peter Douglas. I also undertook my master's degree at UCL, and Peter was vital in teaching me how to use the various pieces of experimental equipment, and for his advice generally. Conor worked with me on the CO_2 laser trapping experiment, a period that was invaluable while I learnt how to operate the MOT. Other thanks must go to Ilhan, James, Alexandros, Lia, Giacomo and Manish for providing moments of levity and support in the lab.

I also have gratitude for the friendship of those outside of academia, in particular those I know from Highgate Harriers athletics club. The athletics track was the perfect place in which I could vent my stresses, and I am eternally grateful to my coach Greg Smith for making me the best athlete I could possibly be. I hope to return to sprinting once my injury problems have abated. More importantly, Faye Morgan deserves a medal for putting up with me over these last four years. She was always there to comfort me after a hard or frustrating day and I have the utmost gratitude for her loyalty and love. I hope that I can repay you one day for everything that you've done.

Finally, I cannot possibly express enough thanks towards my mother and father. Without their support (moral, financial or otherwise) and love, I certainly wouldn't have been able to get to where I am today. I owe all of my academic, sporting or any other successes to them.

Publications

1. P. D. Edmunds and P. F. Barker, *A deep optical cavity trap for atoms and molecules with rapid frequency and intensity modulation*, Review of Scientific Instruments **84**, 083101, (2013)
2. P. D. Edmunds and P. F. Barker, *Trapping cold ground state argon atoms*, Physics Review Letters **113**, 183001, (2014)

Chapter 1

Introduction

To a non-scientist, laser cooling can seem a confusing concept. After all, the popular consensus would be that lasers are generally used to heat things up; think of laser surgery, machining and weaponry. However, in the right arrangement, lasers can also be used to cool things down. An atom or molecule's temperature is inextricably linked to its velocity. Hot particles move around very quickly, while very cold ones are nearly stationary. Touch something hot, and the heat you feel is due to the fast motion of the particles. This is where the basic concept behind laser cooling comes into play. To cool particles down we simply need to slow them down, and we can do this by only using one tool: light.

Light is made up of individual pieces of energy called photons. These photons carry momentum: an extremely small amount of momentum, but still significant enough to matter. Say a hot atom is whizzing towards you at hundreds of miles an hour. You're armed with only a laser to stop it, and aim the beam towards the atom. Momentum from the massive amounts of photons produced by the laser is transferred to the atom and slows it down. Eventually the atom comes to a stop. As its motion has been reduced, it is now "*cold*". This is the main principle behind laser cooling.

In practice cooling is more complicated than this. The laser beam needs to be close to resonance with an atomic transition, and photons are absorbed by exciting the atom up to a higher energy level. This excited level then decays back down to the original level, with the emission of a photon. This photon is ejected in a random direction though, and over many cycles these randoms emissions average themselves out in momentum. There is therefore a *net momentum transfer* against the atom, which leads to a cooling of it. This is known as *Doppler cooling.*

For a collection of atoms, three sets of counter-propagating beams need to be set up to cool all of the atoms (as they will all be moving in random and different directions). This is the basis behind *optical molasses* and *magneto-optical traps* (MOTs) that will be expanded upon in much greater detail in chapter 2.

The advent of laser cooling first came about in the mid 1970's, when Hänsch and Schawlow came up with the theoretical idea to cool atoms with red-detuned light[1]. This soon led to techniques both for slowing atomic beams[2,3] and for their cooling and trapping[4–6]. Particular milestones that should be noted include the first optical molasses experiment[5] created by Steven Chu et al. and also the magneto-optical trap[6] by Raab et al.

Several years later a peculiar phenomenon was discovered. It was previously believed that an atom could not be cooled below a lower limit set by the temperature gained from the random walk caused by the recoil kicks from absorbed photons-known as the *Doppler temperature limit.* However the advent of *sub-Doppler cooling*[7,8] changed this perception.

Moreover, in 1995 another method for further cooling atoms was developed. This was *evaporative cooling*[9], where the trap depth is lowered to allow the warmest trapped atoms to escape. With this, the prospect of creating a *Bose-Einstein condensate* (BEC) increased, and this was soon achieved by first cooling Rubidium in a MOT and then transferring the cold atoms to a magnetic trap. Here they were evaporatively cooled to form the very first BEC[10], a piece of work that culminated in the award of the 2001 Nobel prize to E. A. Cornell, W. Ketterle and C. E. Wieman.

To this day, magneto-optical traps form the basis of many cold atom experiments. Densities of up to 10^{11} atoms/cm^3 are readily obtainable, and temperatures of $\sim$100 μK can be reached. These properties make the resultant cold atomic clouds ideal candidates to load into a variety of traps, where the trapping dynamics can be precisely studied.

1.1 Optical dipole traps

While Doppler cooling techniques were developing, attention was also turning to the development of techniques for trapping atomic clouds. One such method was the dipole trap, which utilises the Stark effect to spatially confine atoms. While traps like MOTs have the ability to create well depths of several Kelvin and therefore trap a portion of even thermal distributions the achievable trap densities are limited by the presence of near-resonant light. Therefore light-assisted collisions can be induced, with the trapping light perturbing the atomic cloud.

As dipole traps generally operate with far-detuned light, such effects do not limit the attainable densities. However, as the Stark effect is a weak interaction, light of high intensity is often required to trap atoms for long periods. Atoms are therefore generally cooled using Doppler cooling techniques first, before being loaded into a dipole trap.

Historically, the first experiment involving the dipole force on neutral atoms was in 1978 when Bjorkholm, Freeman, Ashkin and Pearson successfully focussed and steered an atomic beam of sodium[11]. Progress continued over the following years until the first all-optical trap was developed in 1986 by Chu, Bjorkholm, Ashkin and Cable. Here, sodium atoms were first cooled in an optical molasses before being trapped by a single focussed beam detuned several hundred gigahertz below resonance[12]. The first far-off-resonance trap (FORT) was then developed in 1993 by Miller, Cline and Heinzen where Rubidium atoms were first cooled in a MOT before being loaded into a focussed laser beam detuned 65 nm away from resonance[13].

The use of CO_2 lasers for FORTs was first proposed by Takekoshi et al. in 1995[14]. CO_2 lasers often make ideal candidates for the trapping of atoms as they produce powerful, intensity-stable outputs[15,16]. Moreover, the wavelength output (10.6 μm) is far detuned from atomic resonances, and the optical scattering rates are extremely low. Shortly afterwards, the same group successfully trapped caesium atoms within a focussed CO_2 beam[17] and later detected trapped caesium dimers[18].

Since these periods, dipole traps have been used for a variety of experiments including the creation of BECs of caesium[19], ytterbium[20], chromium[21], strontium[22], calcium[23] and dysprosium[24], the all-optical production of a rubidium BEC[25], the all-optical production of a degenerate Fermi gas of lithium[26] and to create molecular BECs[27–29].

Moreover, dipole traps are not exclusively limited to trapping atoms. As the attainable well depth simply relies on the polarisability of a particle, molecules can also be trapped. As a result of this, atoms and molecules can be co-trapped together and the intra-trap collisions studied[30,31]. Similarly, mixtures of different atomic species can be trapped together. These studies have allowed the study of both spin-exchange and elastic collisions[32,33].

1.2 Molecular cooling

The cooling of molecules is generally more experimentally complex than well-established atomic cooling techniques. Doppler-cooling is less applicable to molecules as molecular energy level structures are more complex. Because of this there is a lack of closed cycling transitions for molecules, greatly complicating the laser setup and cooling scheme. While laser cooling of diatomic molecules like strontium fluoride (SrF)[34], calcium fluoride (CaF)[35] and yttrium oxide[36] has been demonstrated there are very few alternative molecules that can be laser cooled. This is primarily because a molecule that is electronically excited can decay to a variety of different vibrational levels in the ground state, thereby requiring a large number of cooling laser frequencies. Therefore, a variety of alternative molecular cooling techniques have been developed over the past few years.

1.2.1 Methods of producing cold molecules

Feshbach resonances

Magnetically tuneable Feshbach resonances can be used to combine two constituent ultracold atoms and create a bound molecule of comparable temperature. Feshbach resonances occur when the total energy of the initially colliding atoms is equal to that of a resultant bound molecular state. By applying a magnetic field to an atom, Zeeman shifts of the energy level structure are induced. If the two initially colliding atoms have only a small energy difference, this shift can be used to resonantly enhance coupling to a bound state. In this way, an ultracold Feshbach molecule can be created.

Experimentally a wide variety of cold homonuclear and heteronuclear Feshbach molecules have been created, and this work has led to the production of a molecular BEC[37]. Although these molecules ordinarily have short lifetimes (as they are weakly bound) they can be optically pumped down to the electronic ground state to produce a more deeply bound and long-lived molecule[38,39].

While the use of Feshbach resonances allows for the production of ultracold molecules, the range of possible resultant molecules is limited as both of the constituent atoms must be laser cooled (and, of course, that suitable Feshbach resonances must exist).

Photoassociation

Photoassociation is very similar to the use of Feshbach resonances with the exception that a resonantly absorbed photon is used to bond the constituent atoms together to a bound molecular state in an electronically excited state:

$$A + B + \gamma \rightarrow (AB)^{*}. \tag{1.1}$$

Again, both initial atoms (A and B) must be laser cooled and so the range of obtainable ultracold molecules is limited by the set of atoms that can be cooled. The first photoassociation experiments culminated in the production of Na_2 molecules[40]. Optical pumping techniques similar to those described for Feshbach molecules are also applied to de-excite the molecule into an electronic ground state. This has been successfully achieved for a variety of molecules including the production of K_2[41],RbCs[42] and LiCs[43] molecules at sub-milliKelvin temperatures.

Molecular beams

Supersonic molecular beams can be produced by expanding a high-pressure molecular gas through a nozzle. If the mean free path of the molecules is much larger than the diameter of the nozzle then molecules can escape without undergoing collisions and therefore an effusive beam is produced (where the velocity distribution as well as the distribution over the rotational and vibrational internal degrees of freedom are the same as in the high-pressure molecular source). If, however, the mean free path is smaller than the size of the nozzle then the opposite is true. Here, a supersonic beam is produced as many collisions take place within the expansion region[44].

The effect of these collisions is to adiabatically cool all of the degrees of freedom and the energy for each molecule in the gas is transferred to kinetic energy in the direction of travel of the molecular beam. The consequence of this is to narrow the velocity distribution in this direction, and the gas is therefore cooled[45]. After this period, there are comparatively few collisions (due to both the cooling and reduction of density) and the beam has directed flow. The beam can then be passed through a skimmer to remove the divergent and warmer molecules. The molecular beam can also be seeded with noble gas atoms to increase the efficiency of this internal cooling.

Stark and Zeeman deceleration

While these molecular beams can produce internally cold molecules (of the order of 1 K), the beam itself is moving quickly within the laboratory frame (∼400 m/s). Methods have therefore been developed to slow these beams down, of which Stark and Zeeman deceleration are two of the most recent examples.

Electrostatic Stark deceleration utilises a time-varying inhomogeneous electric field to bring a supersonic molecular beam to rest[46–48]. If a molecule is low-field seeking (i.e. it is attracted to a region of low electric field), then it will be decelerated as it moves from an area of low electric field to an area of high electric field. Electric potential hills can be created along the molecular beam. If the electric field is shut off at a peak of one of these electric hills, then the kinetic energy that has been lost during the deceleration procedure will not be gained again as a molecule falls back down the potential hill. This is repeated until the molecules can be brought to rest.

This method was experimentally demonstrated in 1999, when a beam of metastable CO molecules were decelerated from an initial velocity of 225 m/s to a final velocity of 98 m/s[46]. Since this time the scheme has been used on a variety of molecules[49–53], decelerating beams to zero velocity with densities somewhere between 10^6 and 10^9 cm^{-3}. Rydberg molecules have also been successfully decelerated[54], and are ideal candidates for Stark deceleration as a large Stark shift can be easily induced. Therefore lower electric fields can be used. More recently, hydrogen molecules have been both slowed using this method and loaded into an electrostatic trap[55,56].

Zeeman deceleration is the magnetic equivalent to Stark deceleration where an external inhomogeneous magnetic field is applied to decelerate a molecular beam. While this method has been applied to a large variety of atoms[57–60], to date the only molecular species it has been successfully applied to is oxygen[61]. Here, a beam of oxygen molecules was decelerated from an initial velocity of 389 m/s down to a final velocity of 83 m/s. However, the method is experimentally applicable to any species with a permanent magnetic moment (any paramagnetic molecule). Zeeman deceleration has also been used for the stopping of a supersonic beam of metastable neon[62] and for the deceleration of atomic hydrogen into a magnetic trap[63].

Optical Stark deceleration

An attractive alternative to either Stark or Zeeman deceleration is that of optical Stark deceleration. With this technique two intense ($\sim 10^{16}$ Wm^{-2}) far off-resonance beams are overlapped such that they almost counter-propagate. They therefore produce an optical lattice interference pattern whose well depths can be used to trap atoms or molecules by the dipole force. If there is a frequency difference between the two beams the lattice can be made to travel at a certain velocity, with the effect of decelerating a portion of the molecular beam. An advantage to this method over electrostatic Stark or Zeeman deceleration is its applicability to any molecular species, as the attainable well depths simply rely on the polarisability of the molecule.

This technique has been demonstrated with constant velocity lattices that travel at a slower speed than the initial molecular beam. Nitric Oxide molecules have been successfully decelerated[64] from 400 to 321 ms^{-1}, while Benzene molecules have been brought to rest by a lattice travelling at half the initial speed of the molecular beam[65].

By frequency-chirping one of these beams the optical lattice be made to decelerate or accelerate, thereby decelerating or accelerating any molecules or atoms trapped within the lattice[66]. Decelerating the lattice offers various advantages over using a constant velocity lattice (where precise timings and switching can be technically challenging), including the ability to achieve narrower final velocity spreads than constant velocity lattices.

Work towards the chirped optical Stark deceleration of molecular hydrogen is currently being performed within our research group. A custom laser system has been designed such that two high intensity ($10^{12} - 10^{14}$ Wm^{-2}) beams at 1064 nm can be created, and one beam chirped in frequency with respect to the other[67]. Moreover, this laser system has recently been used to accelerate metastable argon[68] cooled within an magneto-optical trap to velocities of up to 191 ms^{-1}, thereby proving its suitability for molecular deceleration.

Buffer gas and sympathetic cooling

Both buffer gas and sympathetic cooling techniques are conceptually simple. They both involve utilising thermalising elastic collisions between the atomic or molecular sample and another species that is initially colder. The two species thermalise and therefore lead to a cooling of one (the sample that is of interest) and, conversely, a heating of the other. Of vital importance to this method is to have a high elastic cross-section between the two species, and a good ratio of elastic to inelastic collisions.

Helium is regularly used for buffer gas cooling as it is inert and can be readily cooled to temperatures down to several hundred milli-Kelvin in a cryostat. The first molecular species to be cooled by a buffer gas was calcium monohydride (CaH) which was successfully cooled to 400 mK by thermalising collisions with helium[69]. Once cooled, the molecules were then loaded into a magnetic trap.

Sympathetic cooling involves initially laser cooling an atomic species instead of a cryostat. This technique has previously been used to cool ^{6}Li fermions to 9 μK by collisions with ^{7}Li atoms that were initially cooled in a magneto-optical trap[70]. In similar work, sympathetic cooling was used to form a BEC of potassium with evaporatively cooled rubidium[71] and also to cool molecular ions in ion traps[72].

Since these initial experiments, there have been various proposals and theoretical studies into the sympathetic cooling of molecules. In these studies, it is vital to fully understand and model not only the expected elastic cross-sections but also the elastic to inelastic collision ratio to ensure effective cooling. The majority of these proposals involve electrostatic or magnetic trapping of a molecular species with a laser-cooled alkali metal[73,74]. However, these studies also highlight that maintaining a good elastic to inelastic collisional ratio may not be achievable over the whole range of temperatures required for effective sympathetic cooling. Inelastic collisions could promote the molecules to an untrappable state and therefore limit possible trap lifetimes. Moreover, as alkali metals are particularly reactive, chemical reactions could lead to another trap loss channel[74].

However, an alternative proposal is to trap molecules and a laser-cooled ground state noble gas together in an optical dipole trap[75] (where all species can be trapped in their ground state-unlike magnetic or electrostatic trapping). The work presented in this thesis describes work towards such an experiment.

Sympathetic cooling with laser cooled rare gas atoms

Sympathetic cooling with rare gas atoms offers offers some advantages over alkali metals: they are inert and the losses due to state changing collisions should be minimised. Moreover, by optically trapping the atoms or molecules instead of using an electrostatic or magnetic trap, all ro-vibrational levels in the molecule's electronic ground state can be trapped. The experimental work undertaken and described during the course of this thesis outlines the creation of an ultracold and inert atomic source for sympathetic cooling.

This sympathetic cooling scheme first involves laser cooling a rare gas in its lowest lying metastable state ($ns[3/2]_2$). Laser cooling is not feasible in the absolute ground state as the closed cycling transitions are in the ultra-violet range and are inaccessible by current laser technology. However, all metastable atoms can be optically quenched down to the ground state (apart from helium, where Stark-induced transitions can instead be used). The ground state atoms can then be co-trapped in an optical dipole trap along with the molecular species which has been slowed by optical Stark deceleration (previously simulated[66] for molecular iodine, by modelling the evolution of the velocity distribution function, to provide stationary molecules at temperatures in the hundreds of milliKelvin and at densities of $\sim 10^{12}$ cm^{-3}).

All of the noble gas atoms (except for radon) have previously been laser cooled in a metastable state[76–83], but selecting one for sympathetic cooling experiments initially took some care. Theoretical work was undertaken[84] to calculate the elastic cross-sections between para-H_2 and various noble gases to assess the feasibility of sympathetic cooling. Here, the collisional cross-section was largest between H_2 and both helium species He_3 and He_4 (in the $10^4 - 10^5$ Å^2 range). However, the recoil temperature from returning metastable helium to its electronic ground state is over a milliKelvin and therefore makes the sympathetic cooling of molecules down to the "ultracold" range impossible. However, the next largest cross-section was found to be argon at $\sim 10^3$ Å^2. Indeed, argon has a Doppler temperature of 203 μK and a recoil temperature from optical quenching of only 66 μK therefore making it the ideal candidate for sympathetic cooling. Krypton, neon and xenon all have similar Doppler and recoil temperatures but have lower elastic cross-sections. Sympathetic cooling would therefore be less efficient as the thermalisation times would be longer.

Moreover, some simulations of Ar-H_2 and Ar-C_6H_6 (benzene) interactions were carried and showed thermalisation between the two species on a timescale of several seconds[85]. In this work, various initial atomic and molecular density conditions were considered and final temperatures of 330±30 μK (calculated for 250 atoms and 25 molecules per lattice site) and 600±100 μK (500 atoms and 300 molecules per lattice site) were calculated for molecular hydrogen and benzene respectively.

As the polarisability of ground state noble gases is at least an order of magnitude lower than metastable noble gases, a deep optical trap must be used to provide sufficient trap well depths. Moreover, a deep trap is required to efficiently trap the initially "hotter" molecular species (in the tens of milliKelvin range). Utilising an optical cavity for its power enhancement properties (amplification of input power up to two or three orders of magnitude) is an attractive option to provide sufficient trap depths as creating such a deep dipole trap is not feasible with a single focussed beam.

1.2.2 Applications of cold molecules

High resolution spectroscopy

By internally cooling a molecular sample, the spectroscopic resolution can be dramatically increased. As has already been discussed, internally cold samples can be prepared in supersonic beams. However, as the molecules travel at a high velocity (with respect to the lab frame) the interaction time between the molecular sample and an applied laser field is very short (of the order of several hundred milliseconds). By Stark or Zeeman decelerating the beam, the interaction time can be increased. Indeed, one of the first molecular spectroscopic experiments involved the Stark deceleration of $^{15}ND_3$ where the interaction time was increased such that the hyperfine structure could be resolved[86]. In related work, metastable CO and cold vibrationally excited OH molecules have both been Stark decelerated before being electrostatically trapped. The radiative lifetime of both species was then studied[87,88].

Importantly, the increased resolution from internally cooling molecules has led to various proposals to more accurately measure the electron electric dipole moment and to study the time variation of fundamental constants (for example the fine structure constant[89] and the ratio of m_p/m_e[90]). Making an accurate measurement of the electron electric dipole moment is particularly significant as it would imply that an extension beyond the standard model (which predicts a non-zero but very small electric dipole moment of $\sim 10^{-38}$ e.cm) would be necessary. If the electron dipole moment is bigger than that predicted by the standard model then this would imply violation of both parity and time-reversal invariance[91]. To date, the most recent measurement has been achieved by using cold thorium monoxide and this work resulted in the electric dipole moment being calculated to have an upper limit of 8.7×10^{29} e.cm[92].

Cold chemistry and collisions

The ability to cool molecules to ultracold temperatures opens up a new avenue for the study of chemical reactions within this previously unobtainable temperature range. Here, quantum mechanical effects can dominate the reaction process as at ultracold temperatures there is not enough thermal energy to overcome the chemical reaction activation energy. Indeed, at ultracold temperatures the reaction rate can even increase as quantum tunnelling effects allow the repulsive barrier to be overcome[93]. Moreover, these quantum effects and therefore the reaction rates can be precisely controlled[94] by manipulating the quantum state. This has been experimentally shown by spin polarising cold KRb molecules to achieve reaction rates that are 10-100 times slower than for a spin-mixed sample[95].

Moreover, molecular beams make ideal candidates for crossed-beam collision experiments. While the collisional energy could be tuned by varying the relative angle between the beams, the resolution of early experiments was limited by the velocity spread of the beams[96]. Upon the advent of Stark and Zeeman deceleration the attainable resolutions improved significantly and the molecular beams could be readily tuned in velocity. This increased resolution has been used to display quantum threshold and resonant effects. One experiment displaying these effects involved the magnetic trapping of Stark-decelerated OH molecules which were collided with velocity-tuneable beams of He and molecular D_2[97]. Another involved the tuneable inelastic scattering of OH radicals with Xe atoms, where the near-threshold inelastic cross-sections were precisely measured[96].

1.3 Thesis overview

The motivation behind the work presented in this thesis is to create an ultracold and inert source for the sympathetic cooling of molecules. With the exception of direct laser cooling of molecules (which is only applicable for a small variety of species), sympathetic cooling has the potential to bridge the gap between the milli-Kelvin barrier and into the micro-Kelvin regime that is currently unattainable by other methods. By cooling and trapping an inert gas to ultracold temperatures at densities of $\sim 10^9$ cm^{-3}, the atomic cloud can be used as a coolant for a wide variety of molecules to below the milli-Kelvin barrier[85].

Generally, this thesis describes the dipole trapping of both metastable and ground state argon (an ideal candidate for use as a coolant for the sympathetic cooling molecules). A brief breakdown of each individual chapter can be described as follows:

Chapter 2 In this chapter I describe the theory behind the laser cooling of atoms (and specifically argon) and the theory of the optical dipole trap.

Chapter 3 The operation and characterisation of the metastable argon magneto-optical trap are also described. The vacuum system, optical layout and experimental layout are described as well as measurements of the atomic cloud temperature and density.

Chapter 4 Metastable argon atoms are loaded into a dipole trap formed within the waist of a focussed CO_2 laser beam. The alignment of the trap and characterisation of the trap lifetime are described.

Chapter 5 Here, we discuss the theory behind optical cavities, including the origins of the power build-up and the theory behind Pound-Drever-Hall locking a cavity onto resonance.

Chapter 6 The work presented in this chapter describes the work that was published in our 2013 *Review of Scientific Instruments* paper[98]. Here, the construction and design of an optical cavity are described and metastable argon atoms are loaded into a trap formed within the cavity. A variant of the Pound-Drever-Hall method was used to lock the cavity on resonance and allowed rapid modulation of the trapping intensity and frequency. The cavity and resultant trap were fully characterised.

Chapter 7 Metastable argon atoms are quenched down to the ground state and trapped within the cavity. Ground state argon and metastable argon are co-trapped together and the intra-trap collisional dynamics studied to detect the ground state atoms. This chapter formed the basis of our 2014 *Physics Review Letters* publication[99].

Chapter 8 This chapter consists of the conclusion: summarising the results presented and exploring the opportunities for future work.

Chapter 2

Laser cooling and trapping theory

The main body of work in this thesis involves the cooling and trapping of both metastable and ground state argon. This chapter outlines the basic theoretical concepts behind the cooling and trapping of an atomic species and, in particular, for the case of argon. Thorough derivations can be found in Harold J. Metcalf and Peter van der Straten's book "Laser cooling and trapping"[100].

2.1 Laser cooling

As we already discussed in the introduction; photons carry momentum equal to $\hbar\boldsymbol{k}$ (where $\boldsymbol{k} = \left(\frac{2\pi}{\lambda}\right)\hat{z}$ is the photon wavevector). If the light is near-resonant to an atomic transition, ω_0, then photons can be absorbed by the atom (which is then excited from a lower level $|g\rangle$ to an upper level $|e\rangle$). This absorption of incoming photons leads to a net momentum "kick" against the atom. Decay of the atom back down to state $|g\rangle$ from $|e\rangle$ due to spontaneous emission also imparts momentum onto the atom. This process, however, averages out to zero over many cycles as photons are emitted in a random direction. If the atom is counter-propagating to the laser light, then there will therefore be a net slowing effect on the atom. As temperature is directly linked to velocity, the atom is therefore cooled.

The photon scattering rate depends on the detuning of the light from resonance, Δ, the intensity of the light and also the natural linewidth ($\Gamma = 1/\tau$) of the atomic transition:

$$\Gamma_{scatt} = \frac{s_0\Gamma/2}{1 + s_0 + (2\Delta/\Gamma)^2} \tag{2.1}$$

Here s_0 is the on-resonance saturation parameter and is equal to I/I_s, where I_s is the saturation intensity and is equal to:

$$I_s = \frac{\pi hc}{3\lambda^3\tau} \tag{2.2}$$

Any movement of the atoms leads to a Doppler shift and therefore a different detuning from resonance, making the scattering force dependent on the atomic velocity v. If we re-write the laser detuning, Δ, as $\omega_L - \omega_0 - \boldsymbol{k}v$ where ω_L is the frequency of the laser and ω_0 is the transition frequency then the force on an atom can be written as:

$$F_{scatt} = \hbar k \frac{s_0\Gamma/2}{1 + s_0 + (\frac{2(\omega_L - \omega_0 - \boldsymbol{k}v)}{\Gamma})^2} \tag{2.3}$$

As this force is velocity dependent it can lead to (for atoms counter-propagating with red-detuned light) dissipation of the atomic kinetic energy and is the basis for laser cooling. It should also be noted that this force saturates to a value of $\hbar k\frac{\Gamma}{2}$ for high beam intensities. The most conceptually simple application of a velocity-dependent force is simply to decelerate an atomic beam. Indeed, the early Doppler cooling experiments involved the slowing of sodium beams[2,3] with near-resonant light.

If we assume that the average velocity of an atom within the beam is equal to v, then a counter-propagating laser beam with detuning $\Delta = -kv$ (to compensate for the Doppler shift of the atoms and keep the beam on resonance) can be used to decelerate it. However, as the atoms are slowed the Doppler shift correspondingly reduces. The atoms therefore shift out of resonance with the laser light and the probability of a photon being absorbed by the atom decreases. Therefore to efficiently decelerate an atomic beam, this change in Doppler shift must be compensated for. There are two main methods with which to successfully achieve this: by frequency chirping the slowing beam or by using a spatially varying magnetic field to Zeeman shift the atoms back onto resonance.

Of course, by using only one beam we can slow atoms in one direction only. By instead using three sets of counter-propagating beams we can slow and therefore cool atoms in all directions. If all beams are red-detuned, then if an atom is moving towards one of the beams, it is Doppler-shifted up in frequency and therefore becomes closer to resonance with this beam. Conversely, the atom is Doppler-shifted down in frequency with respect to the beam that is travelling in the same direction as the atom. This leads to the atom being further from resonance with this beam and therefore less likely to absorb a photon.

The atom therefore preferentially absorbs photons from the beam that is travelling against the atom's motion and experiences a force that counteracts its movement. This technique is known as *optical molasses*.

While optical molasses are an effective tool for atomic cooling, they cannot be considered to be a trap as the force is only dependent on the velocity and not the position of the atoms. Atoms can therefore slowly diffuse out of the range of the cooling beams and be lost. For both trapping and cooling, a spatially-varying force is required. By combining optical molasses (consisting of σ^+ and σ^- polarised light) with a spatially-varying magnetic field (causing Zeeman splitting of the magnetic sub-levels), a position-dependent force can be created and atoms can be simultaneously trapped and cooled. This is called a *magneto-optical trap*.

It was initially believed that Doppler cooling techniques could not cool atoms below a lower limit (the Doppler temperature limit) set by the temperature gained from the random walk caused by the recoil kicks from absorbed photons. In the limit of low intensity (i.e. $s_0 << 1$) and with a detuning equal to $-\Gamma/2$, this temperature limit is equal to[100]:

$$T_{\text{Doppler}} = \frac{\hbar\Gamma}{2k_B} \tag{2.4}$$

As can be seen, the Doppler temperature depends solely on the decay rate of the atomic species being cooled. For metastable argon, the decay rate $\Delta = (2\pi) \times 5.87$ MHz and the Doppler temperature is therefore 140.96 μK[100].

Soon after the advent of Doppler cooling, it was discovered that optical molasses and magneto-optical traps could readily achieve temperatures an order of magnitude lower than the Doppler limit. This exposed limitations within the Doppler cooling theory, and a new theory that allowed for sub-Doppler cooling using polarisation gradients was developed[7,8].

Doppler cooling theory doesn't take into account an atom having multiple ground-state sublevels which can each have different light shifts. With a polarisation gradient of the cooling light present, these lights shifts spatially vary over distances of the order of the optical wavelength and can lead to both efficient cooling of the atomic sample and localisation within potential wells.

The lowest possible attainable temperature was found to not be dictated by the Doppler limit, but instead by the momentum "kick" given to an atom that has spontaneously emitted a photon. This is known as the recoil limit, and is given by:

$$T_{\text{recoil}} = \frac{(\hbar k)^2}{2m} \tag{2.5}$$

2.2 Cooling noble gases

Laser cooling a noble gas is experimentally quite different from that of the more commonly cooled alkali metals. While alkali metals have closed transitions (from the electronic ground state) at wavelengths readily accessible by laser diodes, the same is not true for the noble gases. Indeed, for noble gases, the closed cooling transitions from the ground state are between 8-20 eV away and require cooling wavelengths in the vacuum ultraviolet (where no available CW laser sources exist).

Noble gases do, however, have high-lying metastable states (with lifetimes of between 15 and nearly 8,000 seconds) that can act as an effective ground state with nearby and accessible cooling transitions. Due to these metastable atoms having high internal energy they are both difficult to produce (typically done by either electron bombardment or by using a radio-frequency discharge) and fragile. As their internal energy is large, collisions between two metastable species typically leads to ionisation. However, this ionisation means that collisions between the atoms is easy to detect as the released electron can be efficiently detected by using an electron multiplier or micro-channel plate.

However, unlike alkali metals, as noble gases do not have nuclear spin they therefore do not have hyperfine structure (with the exception of ^{3}He*). Alkali metals have multiple ground states, and an atom that is laser-cooled can therefore decay to a ground state that is not resonant with the cooling beam. A re-pumper laser is therefore required to optically pump the atom back to a level resonant with the cooling light. The cooling process is simpler for a noble gas, as they have a single ground state and therefore do not require a re-pumper laser.

All of the noble gases (except for radon) have been cooled within a magneto-optical trap in their lowest lying metastable state[76–79,81,82]. In particular, the collisional processes between metastable atoms has been extensively studied and the minimisation of ionisation processes in ^{4}He* led to the production of a Bose-Einstein condensate[101,102]. Table 2.1 shows the cooling wavelengths, Doppler and recoil temperature limits for all metastable noble gas species.

	^{3}He*	^{4}He*	^{20}Ne*	^{22}Ne*	^{40}Ar*	^{84}Kr*	^{132}Xe*
Laser cooling wavelength (nm)	1083.46	1083.33	640.40	640.40	811.75	811.51	882.18
Doppler limit (μK)	38.95	38.95	203.29	203.29	140.96	133.40	115.64
Recoil limit (μK)	5.433	4.075	2.335	2.125	0.727	0.346	0.186

Table 2.1: Here, the wavelengths (in vacuum) for laser cooling the metastable noble gases are shown along with the Doppler and recoil cooling limits[100].

2.2.1 Atomic properties of argon

The ground state of argon is a completely filled $3p^6$ orbital, producing a symmetric $^1S_0$ state. As with the other noble gases, argon must be cooled in a high-lying metastable state. This is achieved by exciting a single valence electron from the 3p shell, leaving behind a $3p^5$ core. As this electron is high-lying (11.5 eV) and close to the ionisation potential (at 15.8 eV), the atom can be treated as a one-electron atom whose core and outer electron have spin and orbital angular momentum.

The LS coupling scheme that is used for the alkali metals is less applicable to argon and the other noble gases. While it describes the ground state well, it breaks down for higher energy levels. We instead apply the jl coupling scheme to argon. Here, the core angular momentum, L, and the core spin, S, are coupled together to give $j = L + S$ where j is the total angular momentum of the core. The orbital angular momentum, l, of the valence electron is then coupled to j to give $K = j + l$ which, in turn, is coupled to the spin of the valence electron, s, to give the total angular momentum $J = K + s$.

The spectroscopic notation used during the course of this thesis is based on the jl coupling and is of the form:

$$nl[K]_J \tag{2.6}$$

where n is the principal quantum number of the valence electron.

A simplified Grotrian energy level diagram for argon is shown in figure 2.1. Here, the $4s[3/2]_2$ is the metastable state from which the atoms are cooled. Indeed, the cooling transition is from the $4s[3/2]_2$ to the $4p[5/2]_3$ state at a wavelength of 811.5 nm (in air). To optically quench the metastable atoms to the ground state involves a laser operating at 801.4 nm. This will firstly pump the atoms from the $4s[3/2]_2$ metastable state to the $4p[5/2]_2$ state. From here, the atom can decay to the ground state by two possible routes: either via the $4s[1/2]_1$ state or the $4s[3/2]_1$ state.

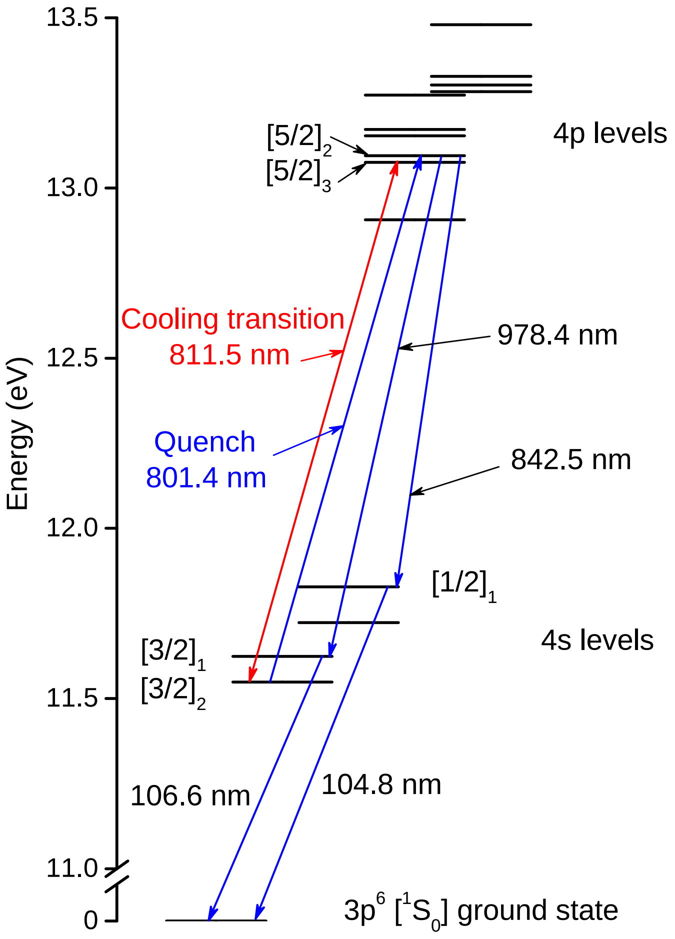

Figure 2.1: Grotrian energy level diagram for argon. Here, we can see the cooling transition between the 4s$[3/2]_2$ metastable state and the 4p$[5/2]_3$ state at a wavelength of 811.5 nm. Also shown is the optical quenching process, involving a laser operating at 801.4 nm. All wavelengths listed are given in air and are taken from the NIST atomic spectra database[103].

2.3 Optical dipole trapping

If a light field is particularly intense it can induce an electric dipole moment in an atom. This, in turn, can induce what's known as a *Stark shift* which is the founding principle of the dipole force. If we consider an atom within a laser field, an electric dipole moment of the form $\boldsymbol{p} = \alpha \boldsymbol{E}$ is induced and oscillates at the driving frequency ω. Here, $\boldsymbol{p}(\boldsymbol{r}, t) = \boldsymbol{\epsilon} p(\boldsymbol{r})\exp(-i\omega t) + c.c.$, and $\boldsymbol{E}(\boldsymbol{r}, t) = \boldsymbol{\epsilon} E(\boldsymbol{r})\exp(-i\omega t) + c.c.$ where $\boldsymbol{\epsilon}$ is the unit polarisation vector, and α is the complex polarisability of the atom.

The induced dipole moment interacts with the electric field to produce a potential of the form (if α is taken to be a scalar quantity):

$$U_{\mathrm{dip}} = -\frac{1}{2}\langle \boldsymbol{p}.\boldsymbol{E}\rangle = -\frac{1}{2\epsilon_0 c}\mathrm{Re}(\alpha) I \tag{2.7}$$

where the angular brackets denote the time average of the oscillating induced dipole moment and electric field and an expression for the intensity of the light field can be given as $I = \frac{1}{2}\epsilon_0 c|E|^2$. Moreover, the factor $\frac{1}{2}$ takes into account that the dipole moment is not permanent but instead is induced.

This expression shows how the potential is directly proportional to both the laser field intensity and the real portion of the atomic polarisability. We can now derive an expression for the dipole force by taking the gradient of this interaction potential to yield:

$$\boldsymbol{F}_{\text{dip}}(\boldsymbol{r}) = -\nabla U_{\text{dip}}(\boldsymbol{r}) = \frac{1}{2\epsilon_0 c}\text{Re}(\alpha)\nabla I(\boldsymbol{r}) \tag{2.8}$$

where we have now shown that the dipole force is dependent on the incident intensity gradient.

Absorption of power from the laser field is caused by the out of phase component of the dipole oscillation, and can be re-emitted as dipole radiation from the atom:

$$P_{\text{abs}} = \langle \dot{\boldsymbol{p}}.\boldsymbol{E} \rangle = \frac{\omega}{\epsilon_0 c}\text{Im}(\alpha(\omega))I(\boldsymbol{r}) \tag{2.9}$$

We can now use this to give an expression for the photon scattering rate:

$$\Gamma_{\text{scatt}} = \frac{P_{\text{abs}}}{\hbar\omega} = \frac{1}{\hbar\epsilon_0 c}\text{Im}(\alpha(\omega))I(\boldsymbol{r}) \tag{2.10}$$

To put this in a more understandable form, we have to fully define the polarisability of a particle which requires using the Lorentz model of a classical oscillator. An excellent summary of this process is given in Grimm, Weidemüller and Ovchinnikov's dipole trapping review[104]. The result of this is to obtain an expression for the complex polarisability:

$$\alpha_0 = 6\pi\epsilon_0 c^3 \frac{\Gamma/\omega_0^2}{\omega_0^2 - \omega^2 - i(\omega^3/\omega^2)\Gamma} \tag{2.11}$$

where Γ is the spontaneous decay rate from the excited state (also equal to the damping rate at resonance: $\Gamma = \left(\frac{\omega_0}{\omega}\right)^2\Gamma_\omega$). While equation (2.11) is not valid when a significant number of atoms are in the excited state and saturation occurs, for far-detuned dipole traps this situation is never reached.

We can now substitute the real and imaginary portions of the complex polarisability into equations (2.7) and (2.10) respectively to obtain:

$$U_{\mathrm{dip}}(\boldsymbol{r}) = \frac{3\pi c^2}{2\omega_0^3}\left(\frac{\Gamma}{\omega_0 - \omega} + \frac{\Gamma}{\omega_0 + \omega}\right) I(\boldsymbol{r}) \tag{2.12}$$

and

$$\Gamma_{\mathrm{scatt}}(\boldsymbol{r}) = \frac{3\pi c^2}{2\hbar\omega_0^3}\left(\frac{\omega}{\omega_0}\right)^3 \left(\frac{\Gamma}{\omega_0 - \omega} + \frac{\Gamma}{\omega_0 + \omega}\right)^2 I(\boldsymbol{r}) \tag{2.13}$$

When the atom is in the presence of a near-resonant optical field, (i.e when $\Delta \equiv \omega - \omega_0 << \omega_0$), then the rotating wave approximation can be applied to simplify these expressions to:

$$U_{\mathrm{dip}}(\boldsymbol{r}) = \frac{3\pi c^2}{2\omega_0^3}\frac{\Gamma}{\Delta} I(\boldsymbol{r}) \tag{2.14}$$

and

$$\Gamma_{\mathrm{scatt}}(\boldsymbol{r}) = \frac{3\pi c^2}{2\hbar\omega_0^3}\left(\frac{\Gamma}{\Delta}\right)^2 I(\boldsymbol{r}) \tag{2.15}$$

These two equations describe the behaviour of dipole traps in general. Specifically, it should be noted that the sign of the potential depends on the sign of the detuning of the trapping field. For the case where $\Delta < 0$ (i.e. red-detuning), the potential is of negative sign and therefore attracts atoms into the area of maximum light field. The opposite is true of a blue-detuned field.

These equations can also be used to note how the dipole potential and scattering rate depend on both the intensity of the light field, and the detuning from resonance. As can be seen, both quantities are directly proportional to the trapping intensity and while the potential is inversely proportional to the detuning, the scattering rate is inversely proportional to the square of the detuning. Therefore, while a laser that is further detuned from resonance will require higher powers to produce the same trapping depths, the scattering rates will be dramatically reduced. It is for this reason that far-off resonance traps created by fields such as those produced by CO_2 lasers (at a wavelength of 10.6 μm) are frequently used. With such a scheme both high trapping intensities and extremely low scattering rates (of the order of 10^{-3} s^{-1}) are achievable.

2.3.1 Far-off resonance dipole trap

The rotating-wave approximation no longer holds valid for far-off resonance dipole traps. Frequently, dipole traps are produced by laser fields detuned by hundreds of nanometres from the nearest atomic resonance. Because of this, we can no longer neglect the second term in equations (2.12) and (2.13). The interaction potential and scattering rate can now simplify (by using the fact that $\omega << \omega_0$) to give:

$$U_{\text{dip}}(\boldsymbol{r}) = \frac{3\pi c^2}{2\omega_0^3}\frac{\Gamma}{\omega_0}I(\boldsymbol{r}) \tag{2.16}$$

and

$$\Gamma_{\text{scatt}}(\boldsymbol{r}) = \frac{6\pi c^2}{\hbar\omega_0^3}\left(\frac{\omega}{\omega_0}\right)^3\left(\frac{\Gamma}{\omega_0}\right)^2 I(\boldsymbol{r}) \tag{2.17}$$

In this case, the dipole potential is well-approximated by a quasi-electrostatic trap (QUEST) potential which is of the form:

$$U_{\text{dip}}(\boldsymbol{r}) = -\frac{1}{2}\alpha_{\text{stat}}|E(\boldsymbol{r})|^2 \tag{2.18}$$

Here, α_{stat} is the static polarisability of the atomic species. Because the trapping potential only depends on this polarisability and the applied electric field, it is applicable to any particle that can be polarised. It can therefore be used for atoms and molecules alike. Due to the extremely low scattering rates achievable in a QUEST, the trapping potential can be assumed to represent a good approximation of a conservative trap (i.e. any atom loaded into the trap will remain trapped until an external influence will cause it to leave).

Chapter 3

Metastable argon magneto-optical trap

Cooling noble gases has some experimental complexities compared to those encountered with the more commonly cooled alkali metals. As closed cooling transitions from the ground state are in the vacuum ultraviolet, where no available CW laser sources exist, noble gases have to be cooled in a high energy metastable state[76–79,81,82]. Experimentally this means that, while MOTs for other species can be loaded by evaporation from an oven, either electron bombardment or a radio-frequency (RF) discharge[105,106] is required to first excite atoms to their metastable state. This process is usually inefficient (promoting only 1 in $\sim 10^5$ atoms to the metastable state), leaving the vast majority of atoms in the ground state. Moreover, as metastable atoms have high internal energy, inelastic collisions between trapped atoms lead to ionisation and therefore to strong loss from a MOT or trap.

This chapter presents the experimental layout behind our metastable argon MOT, which was originally constructed by Dr Conor Maher-McWilliams[107] and Dr Peter Douglas. Various upgrades and changes to the experimental layout of the MOT have been implemented during the course of the work presented in this thesis. These changes will be highlighted in the text.

More specifically, the first portion of this chapter is dedicated to discussing the vacuum and laser systems, along with details of the necessary magnetic fields to produce a magneto-optical trap. Techniques for locking the cooling lasers onto the correct frequencies, including the use of a variant of the dichroic atomic vapour laser lock (DAVLL)[108] and injection locking techniques, are also described and characterised. In the latter half of the chapter, the methods with which we count the number of trapped atoms (including fluorescence and absorption imaging) are discussed and used to provide one and two-body loss rates from the MOT.

3.1 Experimental set-up

3.1.1 Vacuum system

For any atomic cooling experiment, having a low pressure vacuum is vital. Collisions from background gases within any vacuum system limit the attainable lifetimes of any trap. To create an ultra-high vacuum (UHV), two types of pump are usually used: a turbo-molecular pump and an ion pump. Out of these two options an ion pump is arguably the more attractive option as there are no moving parts within the pump itself and therefore no vibrations are produced. Such pumps also have the ability to reach pressures of less than 10^{-11} mbar. However, ion pumps are generally inefficient for noble gases and so are not the ideal candidate for pumping argon.

Due to this, we have to use four turbo-molecular pumps to reach a sufficiently low pressure to create a MOT and to trap atoms. The drawback of turbo pumps is primarily that they are noisy and cause a large amount of vibrations. For the work presented in this thesis, the vibrations caused problems that took considerable effort to overcome. The vibrations imposed frequency noise on any laser locks and made it difficult to trap atoms for any length of time. This will be explained in further detail in both chapters 4 and 6.

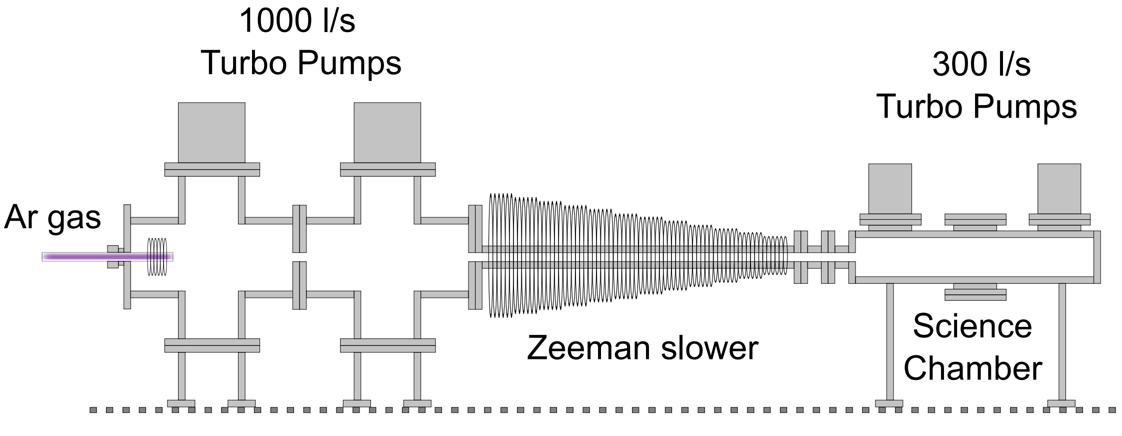

Figure 3.1: Differentially pumped vacuum system, reaching a pressure of 3×10^{-9} mbar in the science chamber when the atomic beam is shuttered.

The schematic for the vacuum system is depicted in figure 3.1. It consists of three main differentially pumped chambers. The system is pumped by two 1000 l/s and two

300 l/s turbo-molecular pumps, which are backed by two Edwards XDS10 scroll pumps. The argon gas is introduced via a glass tube into the first chamber. The pressure inside the glass tube is generally in the mid 10^{-2} mbar range, as this is where the RF discharge efficiency of production of metastable argon peaks. The first chamber is pumped by a 1000 l/s Edwards STP-1033 turbo pump and the pressure here is $\sim 10^{-5}$ mbar. At the end of the chamber is a shutter to block the atomic beam and a skimmer to collimate the effusive beam.

The second chamber is pumped by a 1000l/s Shimadzu TMP-1030M turbo pump, which reduces the pressure in this chamber to $\sim 10^{-8}$mbar. From here the atomic beam the travels through the Zeeman slower, at the end of which is another skimmer. The Zeeman slower is then attached to the science chamber, which is pumped by a Shimadzu TMP-303M and an Edwards STP-301 (both 300 l/s turbo pumps). The pressure in this chamber is measured by an Edwards EBEAM ion gauge. When the atomic beam was unshuttered, the pressure was in the low 10^{-8} range which reduced to $\sim 3 \times 10^{-9}$ mbar when the atomic beam is shuttered.

Despite the fact that all of our turbo pumps were magnetically levitated and designed for low vibrations, the vibrational noise was significant. To reduce this we installed vibration isolators in between the pumps and the chamber. While this helped to reduce the vibrations, fast bandwidth feedback schemes were still required to compensate for the vibrational effects on the laser locks.

3.1.2 Optical layout

The output of the ECDL we used for locking to the atomic transition was not powerful enough to provide for all beams in the experimental MOT set. The following beams were required:

- The pump and probe beams used for locking the ECDL.
- A Zeeman slower beam to decelerate the atomic beam that is formed by the RF discharge (to within the capture velocity of the MOT).
- MOT beams for the actual laser cooling of the metastable argon.
- An optional resonant beam for absorption imaging of the MOT.

In order to boost our total available power, we used the ECDL as a master laser to injection lock a higher power slave laser[109,110]. Here, while a majority of the ECDL light was sent to the pump and probe beams, a small fraction (∼5 mW) of the light was used for injection locking. During the original construction of the MOT, a custom-built mechanical mount was used to house a commercial laser diode (Sanyo DL-8141-035A) that was to be injection locked. However, during the course of this work this combination was found to be too unstable in frequency and was replaced with a Thor Labs temperature controlled laser diode mount (TCLDM9) in combination with a Thor labs 150 mW single mode diode (M9-808-0150) with centre frequency at 808 nm. Presumably the frequency instability in our custom-built mount can be attributed to it not being as stable in temperature as the commercially-built one. As the centre wavelength of the slave diode was 808 nm, the diode needed to be tuned up in temperature to raise the wavelength to the cooling wavelength of 811.5 nm. Out of the diodes that were tested, this was found to be anywhere from 30 to 50 °C. Usually, for longevity, the diode that required the lowest temperature to reach 811.5 nm was selected.

The optical layout for the injection locking is shown in figure 3.2. Here, the majority of the master laser goes to the locking optics and is used to lock the laser onto resonance. The rest of the master beam passes through an AOM, where it is shifted up by 80 MHz. The first diffracted order is then retro-reflected back and is shifted up by another 80 MHz while travelling through the AOM again. This beam is then reflected from the polarising beam-splitter and is used to injection lock the slave laser (detuned 160 MHz away from resonance). A fraction of the slave beam is then picked off to be used directly from the Zeeman slower beam (about 20 mW is needed for this). The rest is again aligned through a double-pass AOM and shifted up in total by ∼140 MHz. This beam is then used for the MOT beams, which have about ∼20 mW in total.

At times during this work (while working on the CO_2 laser dipole trap presented in chapter 4 for example) two injection locked lasers were used to further boost the power. However, this was not a permanent addition as it added an extra instability to the experiment.

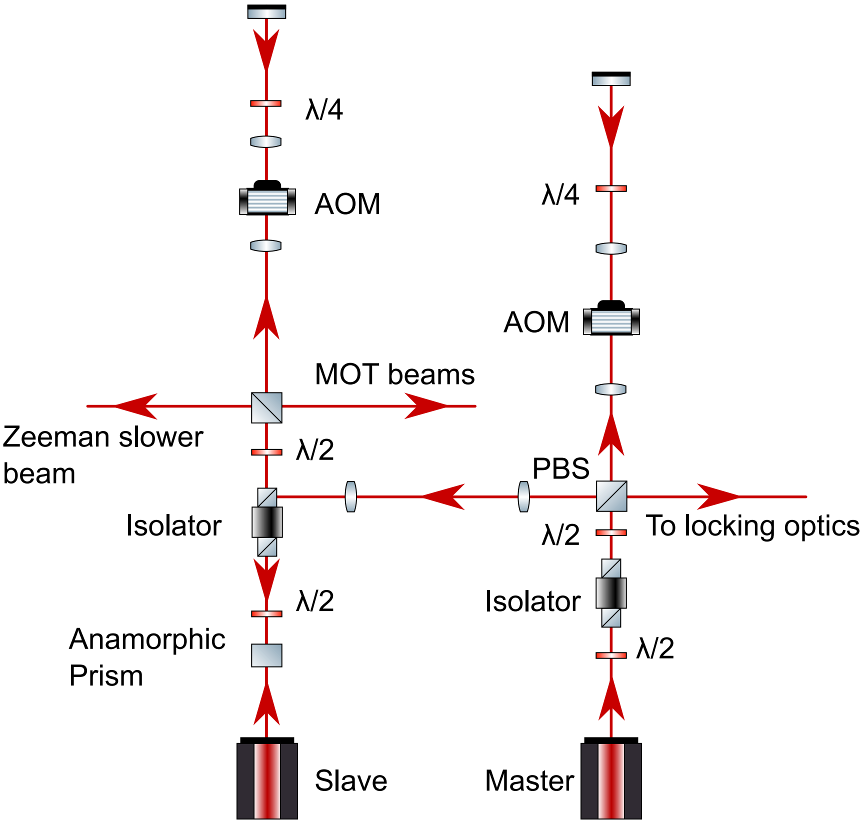

Figure 3.2: Optical diagram showing the injection locking system that was used. Here, a majority of the master beam is used for locking and a small fraction goes towards locking the slave laser. The slave laser is used for both the Zeeman slower and MOT beams. The AOM in the master beam's path shifts the frequency up by 80 MHz in both directions. This frequency then locks the slave and is directly used for the Zeeman slower. The slave AOM shifts the frequency back up by 70 MHz in both directions and so leads to an overall MOT beam detuning of ∼20 MHz.

3.1.3 Radio-frequency discharge and laser locking

To first excite argon to its $4s[3/2]_2$ metastable state we use an RF discharge[105,106], which also serves as a cell which we use to implement a laser stabilisation scheme[111]. Argon gas is introduced to the vacuum chamber through a glass tube with an outer diameter of 12mm, and a needle valve is used to carefully control the pressure within the tube. The glass tube continues inside the first vacuum chamber and is surrounded by a helical coil of copper wire. This coil was driven by an impedance matched circuit at $\sim$ 155 MHz.

To ignite the discharge the impedance matching is carefully tuned until the discharge glows purple (this extends some 10/20 cm from the vacuum chamber and can be easily seen by eye). The discharge is generally operated at pressures of $\sim 5\times10^{-2}$ mbar, as this is where the efficiency of the production of metastable atoms peaks at a ratio of $N_{ar}/N_{ar^*} \sim 10^5$.

As with any atomic cooling experiment, it was necessary to tightly lock our cooling beams to the relevant transition. To do this, we used a variant of the dichroic atomic vapour laser lock (DAVLL)[108]. In our case, we stabilise our lasers using magnetic dichroism within the RF discharge[111].

The laser that we lock to the cooling transition is a Toptica DL 100 external-cavity diode laser (ECDL). These types of lasers have two methods by which you can lock to a certain frequency. The first is to send a control voltage to a piezo-electric transducer (PZT) which controls the angle of a diffraction grating inside the laser. The first diffraction order of this grating is directed back into the diode itself and frequency stabilises the laser while reducing the linewidth to less than 1 MHz. By adjusting the angle of the grating using the PZT, the frequency of emission can be varied up to a maximum of half the free spectral range of the external cavity. The bandwidth of this method depends on the PZT, and is usually of the order of several kHz. The second method of locking the laser is simply to modulate the current that is applied to the laser diode. While this method usually does not have as much frequency-travel as varying the PZT, the bandwidth is much higher. Indeed, if modulation to the current is applied directly to the diode, the bandwidth can be in excess of 1 MHz.

The locking scheme itself (shown in figure 3.3) involves first splitting the output of the ECDL in two: into a pump beam and a probe beam. These beams are overlapped through the RF discharge tube and are used to perform saturated absorption spectroscopy. Here, the pump beam is far more intense than the probe beam and causes saturation of the relevant transition-i.e. there are approximately half of the atoms in the metastable state and the other half excited to a higher level. As the pump beam is scanned in frequency an absorption profile is created over the transition frequency. This profile is Doppler broadened due to the thermal motion of the atoms. As the transition is saturated, when a probe from the probe beam interacts with the atoms there is a high probability that it will cause stimulated emission from the excited state. In this way, the probe beam will cause a peak (free of Doppler broadening) in the absorption profile.

To create an error signal with which to lock the ECDL, we utilise the magnetic dichroism of the atoms in the discharge. Here, we first apply a magnetic field to the discharge (using a pair of Helmholtz coils) and then we split the polarisation of the probe beam into its σ^+ and σ^- components. The magnetic field causes a Zeeman splitting of the resonant

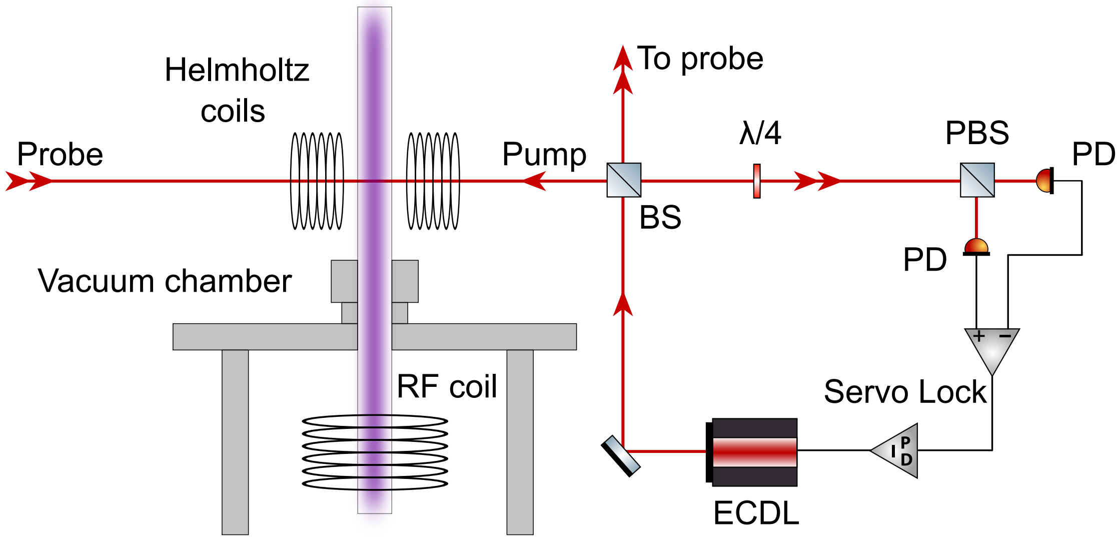

Figure 3.3: Schematic showing the RF discharge and associated locking optics and electronics. Here, the laser beam is split into two parts: a pump and a probe beam. These are used to perform saturated absorption spectroscopy and allow us to lock the ECDL onto a Doppler-free peak.

transition. The σ^+ light pumps the $\Delta m_J = +1$ transitions, while the σ^- light pumps the $\Delta m_J = -1$ transitions.

This splits the absorption profiles for the σ^+ and σ^- light by equal and opposite amounts. To create an error signal for locking, one profile is subtracted from the other. This is similar to the error signal that is created for locking an optical cavity to be discussed in section 5.2. If the ECDL beam is on resonance, the error signal should be at zero and the control voltage sent to either the cavity PZT or the diode current should remain constant. If, however, the beam drifts off resonance then the error signal voltage will increase and force a re-adjustment of the frequency until the laser is back on resonance. In this way an electronic feedback loop is successfully formed and the laser is locked to the relevant transition. A “lockbox” which generally consists of either a proportional-integral or a proportional-integral-derivative controller is then used for stable locking. Here, the amplitude of the error signal and the locking bandwidth can be adjusted. The error signal will be shown experimentally in section 3.2.5.

3.1.4 MOT and Zeeman slower magnetic fields

The construction of the MOT and Zeeman slower magnetic field is described in full in Dr Conor Maher-McWilliams’ PhD thesis[107] and only the main details will be discussed here.

Two anti-Helmholtz coils were required to produce the necessary quadrupole magnetic field to create a MOT. Each of these coils contains 94 turns of 1 mm thick enamelled copper wire and has a radius of 94 cm. At a current of 7 A, these produced a magnetic field gradient of ∼10 Gcm^{-1}. To prevent the coils from overheating they were attached to copper pipes, which were in turn attached to a water chiller.

Background magnetic fields have the potential to effect the position of magnetic zero, and therefore the position of the MOT. These fields also had the potential to adversely effect some necessary MOT operations, for example the temperature measurement described in section 3.2.5. To counter this, three sets of Helmholtz "compensation" coils were created out of 15-way ribbon cable attached onto a square frame of side length 58 cm. By careful adjustment of the current into each set of coils, any undesirable background magnetic field could be effectively cancelled out.

A Zeeman slower was required to initially slow the metastable atoms produced in the RF discharge to within the capture velocity of the MOT (∼ 60 m/s). The Zeeman slower was constructed out of a segmented structure consisting of tapering magnetic field coils of enamelled copper wire. As there are multiple coils, this allowed straightforward tuning of the magnetic field. The Zeeman slower beam itself consisted of ∼ 15-20 mW of σ^+ polarised light at a detuning of -160 MHz from resonance.

3.1.5 Experimental timing

An eight-channel digital pulse delay generator (Quantum Composer 9520) was used for timing control of most of the experimental apparatus. This delay generator was used to trigger the following components:

- Old hard drives were cannibalised for the use of their high speed arms to use as an economical shutter[112,113]. These were ideal candidates for applications where a high-speed switch-off was not required. Both the atomic beam and Zeeman slower beam were shuttered using hard drive arms, and both were extinguished within 0.5 ms. A circuit[113] was created to drive the shutter arms so that a simple TTL pulse could trigger the shutter.

- For the switching-off of laser beams where a fast extinction was of more critical importance, the RF power input into AOMs was switched off. Various AOM drivers (Gooch & Housego 1080AF-AENO-2.0) and RF switches (Mini-Circuits ZX80-DR230-S+) were used for this purpose. This could be achieved by triggering by TTL pulse or control signal sent to the AOM driver. The MOT cooling beams and optical cavity beams were controlled by this method.

- The anti-Helmholtz MOT magnetic field was switched off by sending a TTL signal to a high-power MOSFET solid-state relay (Power IO HDD-06V75). This allowed us to switch off the magnetic field completely within ∼200 μs.
- The EMCCD camera was triggered by a TTL signal.

3.2 Characterisation

3.2.1 Error signal and locking

In section 3.1.3 we discussed the theory and optical layout of implementing our Doppler-free laser stabilisation scheme. The absorption profile of the narrow Doppler-free peak to which the ECDL laser is locked is shown in figure 3.4 a).

While the natural linewidth of the cooling transition is 5.87 MHz, the measured width of the Doppler-free peak is 26 MHz. This broader than expected value can be attributed to laser frequency jitter, power broadening, Zeeman broadening and pressure broadening. Of these, the most significant is power broadening. As the probe intensity (∼4 mWcm^{-2}) is higher than the saturation intensity of 1.44 mWcm^{-2}, 11 MHz can be attributed to power broadening. The next most significant contribution is that of the frequency jitter of the master laser. This jitter is primarily caused by vibrations of the optical table caused by the turbo-molecular pumps, and amounted to ∼10 MHz of broadening.

Vibrations on the optical table caused problems for many areas of the work presented in this thesis. As far as the ECDL master laser goes, initially the error signal was sent to the diffraction grating PZT to lock to the cooling transition. The bandwidth of this locking was, however, only 2 kHz and therefore not sufficient to compensate for the oscillations on the optical table. While it was possible to obtain a MOT (and the MOT was run in this configuration for several years until the middle of my PhD), this meant that the 10 MHz of laser broadening was present and therefore limited the MOT density as a result. It was first noticed that this broadening was causing problems when it was impossible to detect an absorption imaging signal (as described in section 3.2.3).

To counter this, a higher bandwidth lock was implemented on the current of the laser. To do this the error signal was sent to the Toptica DCC 110 current control module, which

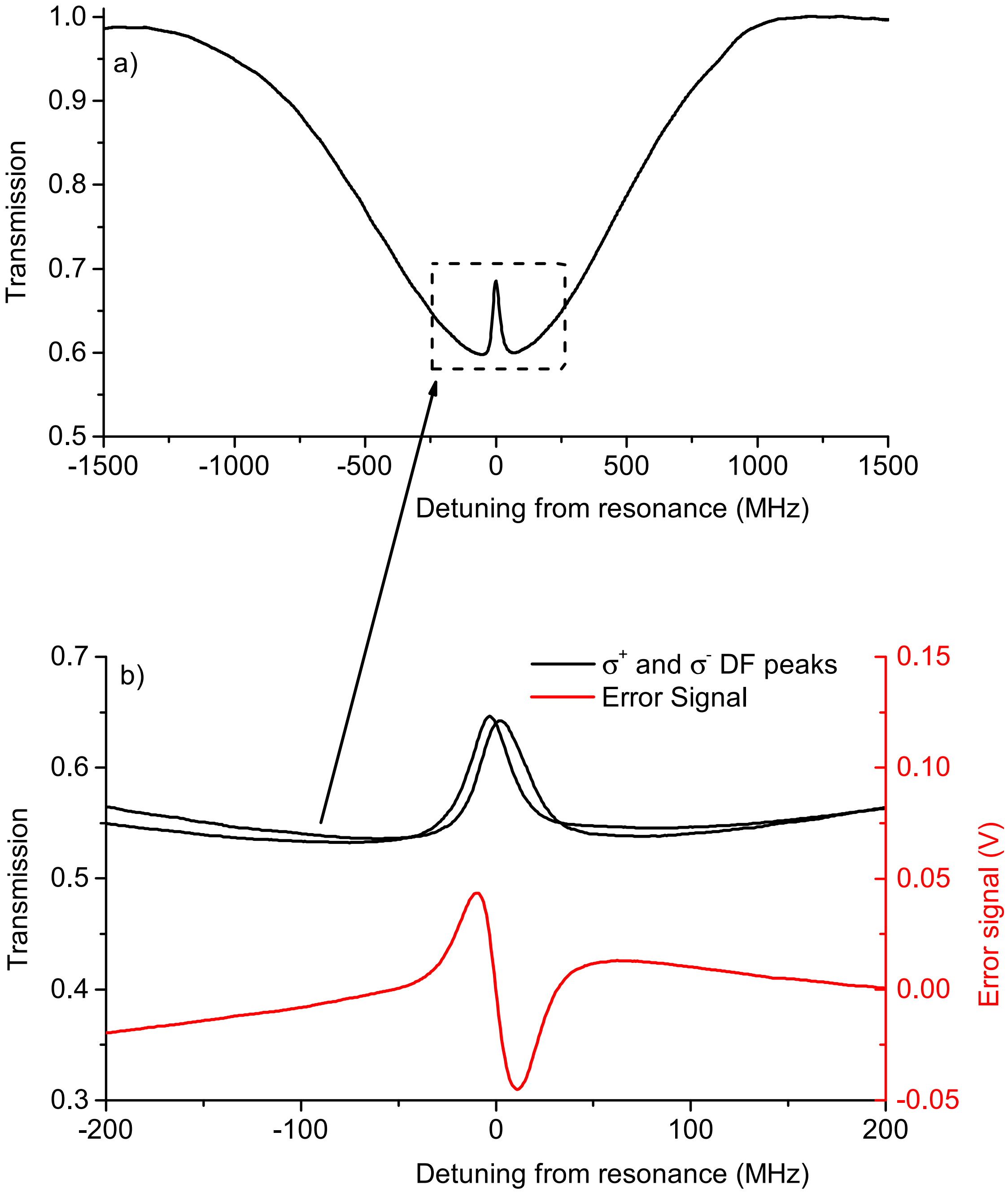

Figure 3.4: The top graph shows the saturation absorption spectroscopy signal, including the Doppler-broadened absorption profile and the Doppler-free peak in the centre of this profile. b) shows both the Zeeman shifted σ^+ and σ^- absorption profiles, as well as the error signal produced by subtracting one from the other.

had a maximum bandwidth of 7 kHz. While this is only a small increase in bandwidth, it proved sufficient to compensate for the vibrational noise on the laser.

3.2.2 Injection locking

In section 3.1.2 we discussed how the ECDL master laser did not have sufficient power output for all MOT beams and how an injection locking scheme[109,110] was used to overcome this. The initial setup of the injection locking involved both aligning and mode-matching the master beam into the slave laser aperture and finding the right temperature and current settings for the slave to be successfully injection locked. In order to tell when the slave laser was locked onto resonance, the output of the slave laser was then aligned through the glass RF discharge tubing and directed onto a photodiode.

When the slave laser is on resonance some light should be absorbed and would be noted as a dip in the photodiode signal. While on resonance the slave beam also causes fluorescence through the discharge, due to spontaneous emission, and can be noted using an IR viewer.

The first stage in setting up the injection locking involved careful overlap of the master laser beam onto the facet of the slave diode. Once the was achieved, the temperature and current of the slave diode were systematically changed until absorption through the RF discharge was noted. From here, the alignment was carefully adjusted until the injection locking range was optimised.

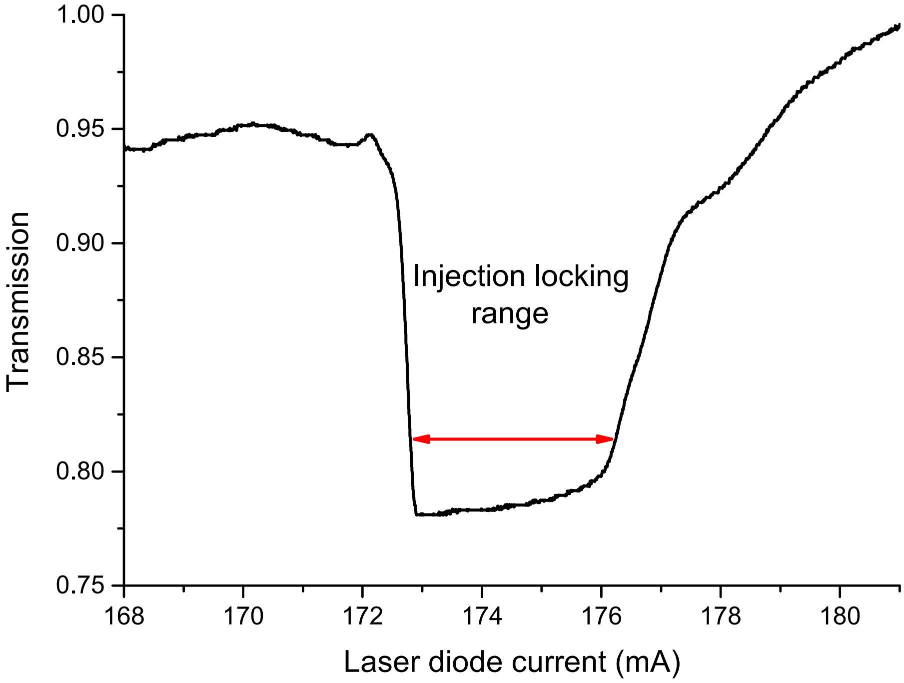

Figure 3.5: Graph of the slave diode laser being scanned in current and showing the injection locking range. This signal is of the slave beam directed through the glass RF discharge tube and aligned onto a photodiode. The dip in signal on the photodiode corresponds to where the slave laser is injection locked and therefore on resonance (where light from the slave is absorbed by metastable atoms).

As can be seen in figure 3.5, the injection locking range is of the order of 3-4 mA. If the temperature of the lab is stable, this range is usually sufficient to keep the slave laser locked for several days. Slight changes in temperature can cause the slave laser to come out of lock, but this is usually rectified by tweaking the current of the slave diode.

3.2.3 Fluorescence and absorption imaging

To calculate the number and density of trapped atoms, two main methods are used in this thesis: fluorescence and absorption imaging. Fluorescence imaging is arguably experimentally more straightforward as it simply involves detecting the scattered photons from the MOT on a CCD camera. This method, however, involves a larger number of sources of error.

The largest error can be attributed to calibrating the pixel units on the CCD chip to number of photons that are incident on it. This was done by aligning a strongly attenuated MOT beam (whose power was carefully measured) onto the CCD chip, and converting the measured pixel count to the known amount of photons incident on the chip. Throughout the course of the work presented in this thesis, a thermo-electrically cooled Andor iXon+ electron multiplying CCD (EMCCD) camera was used along with a Computar MLH-10X zoom lens. The camera efficiency, η, was determined to be 3.8±0.6 photon/pixel count.

To calculate the number of metastable argon atoms in the MOT, we use an equation that arises from the photon scattering rate given in equation 2.1:

$$N_{Ar^*} = \frac{1 + 6s_0 + (2\Delta/\Gamma)^2}{6s_0(\Gamma/2)\Omega_d l} \frac{N_{\text{counts}}\eta}{t_{\text{exp}}} \tag{3.1}$$

where $s_0 = I/I_s$ and I is the intensity of a single MOT beam (and I_s is the saturation intensity, equal to 1.44 mWcm^{-2}). Δ is the detuning from resonance, Γ is the natural linewidth (5.87 MHz), N_{counts} is the number of measured counts by the camera, η is the camera efficiency, Ω_d is the total fraction of light emitted that falls on the imaging lens, l is an attenuation factor that accounts for absorption/scatter of light from the imaging optics and t_{exp} is the exposure time.

To calculate Ω_d we need to evaluate the fraction of photons that are scattered isotropically from the MOT that reach the imaging lens within a solid angle $d\Omega$. In this way, we can calculate the fraction detected by using $\Omega_d = d\Omega/4\pi$. Given that the lens that was used had a radius of 1.63 cm and was a distance of 16 cm away from the MOT, we calculate Ω_d to be 2.6×10^{-3}.

Figure 3.6 shows an example of a fluorescence image taken by the EMCCD camera.

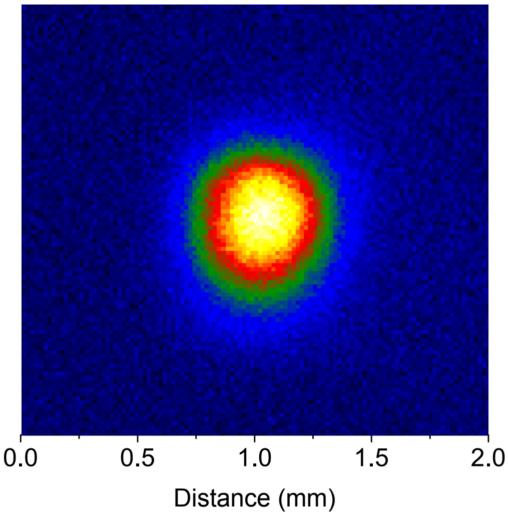

Figure 3.6: Typical fluorescence image of the MOT cloud.

This image shows a MOT of $1/e^2$ radius 230 μm, containing 3.3×10^5 atoms at a density of $\sim 6\times10^9/\mathrm{cm}^3$. The width of each pixel on the camera was determined by keeping the focal length of the lens set at what is necessary to have the MOT in focus, and then taking a picture of a ruler at this distance. In this way the number of pixels/cm can be accurately measured (in our case, each pixel equated to 12.5 μm).

Absorption imaging involves passing a resonant laser beam through the atomic cloud and using the absorption of light to measure the trapped atom number. To derive an equation for this, we first recall the photon scattering rate from equation (2.1):

$$\Gamma_{\mathrm{scatt}} = \frac{\Gamma}{2}\frac{s_0}{1+s_0+(2\Delta/\Gamma)^2} \tag{3.2}$$

If we note that the amount of scattered power per unit volume is $\rho\hbar\omega\Gamma_{\mathrm{scatt}}$, where ρ is the density of trapped atoms, then we can write the rate of change in the absorption imaging beam intensity as:

$$\frac{dI}{dy} = -\rho\hbar\omega\Gamma_{\mathrm{scatt}} \tag{3.3}$$

where the y axis is defined as the direction of travel of the beam. In the limit of $I \ll I_{\mathrm{sat}}$ the resonant absorption cross section can be written as $\sigma_0 = 3\lambda^2/2\pi$ for a two-level atom. Substituting I_{sat} into this expression, we obtain:

$$\sigma_0 = \frac{\Gamma}{2}\frac{\hbar\omega}{I_{\mathrm{sat}}} \tag{3.4}$$

By putting this into equation (3.3), we find:

$$\frac{dI}{dy} = -\rho\sigma_0 \frac{I}{1 + s_0 + (2\Delta/\Gamma)^2} \tag{3.5}$$

Now if we integrate this equation with respect to y, then we can find the amount of light absorbed. To do this, we first assume that the MOT density can be described by a normalised Gaussian:

$$\rho(x, y, z) = \rho(x, z) \frac{1}{\sigma_y\sqrt{2\pi}} \exp\left(-y^2/2\sigma_y^2\right) \tag{3.6}$$

where σ_y relates to the $1/e^2$ radius of the MOT cloud along the y axis. We can now therefore integrate equation (3.5)

$$\int_{I_0}^{I} \frac{1 + s_0 + (2\Delta/\Gamma)^2}{I} dI = -\sigma_0 \int_{-\infty}^{\infty} \rho(x, z) \frac{1}{\sigma_y\sqrt{2\pi}} \exp\left(-y^2/2\sigma_y^2\right) dy \tag{3.7}$$

to obtain:

$$\left(1 + \frac{4\Delta^2}{\Gamma^2}\right) \ln\left(\frac{I}{I_0}\right) + \left(\frac{I - I_0}{I_{\text{sat}}}\right) = -\sigma_0\rho(x, z) = -\text{OD}(x, z) \tag{3.8}$$

where $\text{OD}(x, z)$ is the optical depth of the MOT cloud and the density can be expressed as

$$\rho(x, z) = \frac{N \exp\left(\frac{-x^2}{2\sigma_x^2} - \frac{-z^2}{2\sigma_z^2}\right)}{2\pi\sigma_x\sigma_z} \tag{3.9}$$

To integrate the right-hand side of equation 3.7, we have used the fact that the integral of a normalised Gaussian is unity. While on resonance and in the limit of low laser intensity, equation (3.8) can be simplified as:

$$I = I_0 \exp(-\text{OD}(x, z)) \tag{3.10}$$

which is analogous to the Beer-Lambert law.

By combining and rearranging equations (3.8) and (3.9), we can use the optical depth to obtain the number of atoms within the MOT cloud:

$$N = \frac{2\pi\text{OD}(x, z)\sigma_x\sigma_z}{\sigma_0} \exp\left(\frac{(x - x_c)^2}{2\sigma_x^2} + \frac{(z - z_c)^2}{2\sigma_z^2}\right) \tag{3.11}$$

and at the centre of the atomic cloud (coordinates (x_c, z_c)) this simplifies to:

$$N = \frac{2\pi \mathrm{OD}_{\mathrm{peak}} \sigma_x \sigma_z}{\sigma_0} \tag{3.12}$$

Experimentally, a short pulse of low-intensity (< 1 μW) resonant laser light is required. A short low-intensity pulse ($\sim$10 μs) is needed so we do not destructively perturb the MOT. Two separate methods of calculating the trapped atomic number by absorption were used. The first involved using a beam that is much larger than the MOT and was simply aligned through the MOT and onto the EMCCD chip. The result of this is to produce an image that displays the "shadow" of the MOT due to absorption of the resonant light. To do this, three images were taken: one of the absorption beam when there are no atoms present (I_{initial}), one when the beam is passed through the atomic cloud (I_{atomic}) and the other is a background image (with the absorption beam blocked) ($I_{\mathrm{background}}$) to account for stray light. These three images allow us to calculate the optical depth as:

$$\mathrm{OD} = \ln \left(\frac{I_{\mathrm{initial}} - I_{\mathrm{background}}}{I_{\mathrm{atomic}} - I_{\mathrm{background}}} \right) \tag{3.13}$$

Figure 3.7 shows a typical absorption signal detected by the EMCCD chip, and inset is the actual image recorded by the camera. As can be seen, the peak absorption through the MOT cloud is $\sim 8\%$. The $1/e^2$ radius of the atomic cloud gave a similar result to that of fluorescence imaging and measured 240 μm. This was simply calculated by noting that the width of each individual pixel on the camera measured 8 μm, and by assuming that the resonant imaging beam was well collimated. The slightly larger width as measured by this absorption technique can possibly be attributed to a slight divergence of the imaging beam.

A subtly different method was also used to get not only density information about the atomic cloud, but also about the stability of our imaging and cooling beams. To achieve this, we focus the resonant beam down to $\sim 50\mu$m and align it through the centre of the MOT cloud. To check that the beam is correctly aligned, the power is turned up until a stripe is seen through the MOT.

In this method, this beam is set to a low enough intensity as so to not perturb the MOT and is pulsed through the MOT for a period of $\sim 200\mu$s. During this time the detuning of the beam is swept from ~ -20 MHz to ~ 20 MHz by sending a control voltage to

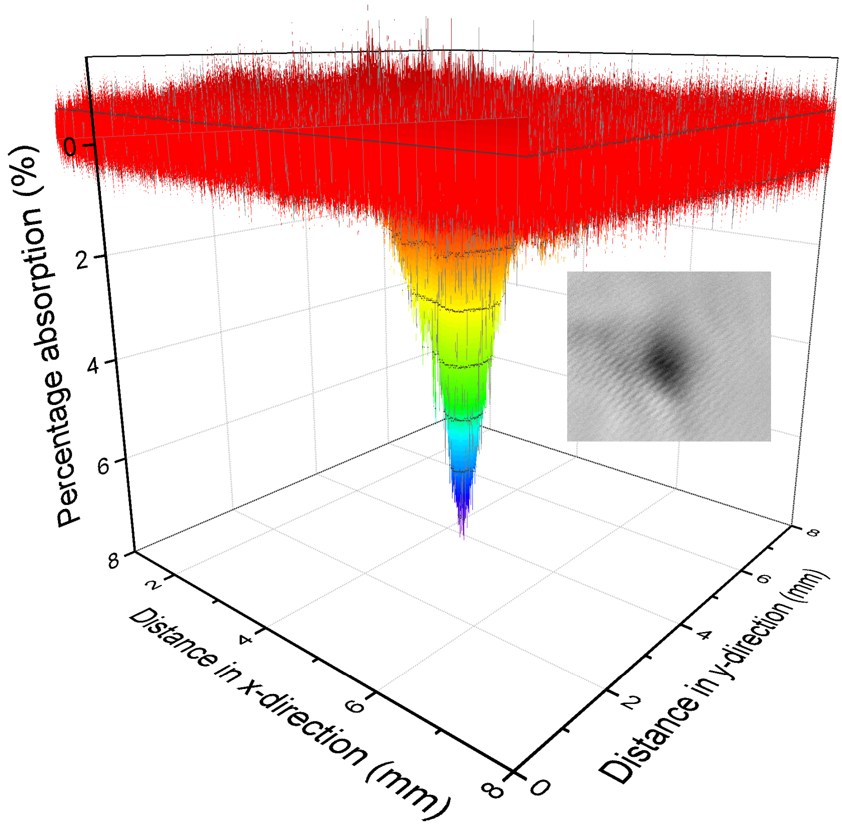

Figure 3.7: Percentage absorption of the resonant beam through the MOT cloud. Inset is the actual image recorded by the EMCCD camera.

a voltage-controlled oscillator (VCO) that sends a signal to an acousto-optic modulator (AOM) amplifier. In this way, we can map out the lineshape of the transition and assess how stable our beams are.

Figure 3.8 shows the result of this, where we can see two pulses corresponding to when there is a MOT present and when there is not. As can be seen, the case where the MOT is present shows absorption when the beam is close to or on resonance. From this we can again work out the optical depth of the optical cloud, and can also calculate the linewidth of the cooling transition by fitting a Lorentzian to the absorption spectrum.

Figure 3.9 shows the fractional absorption through the MOT cloud as the frequency is scanned. Interestingly, the linewidth of this was measured to be 5 ± 1 MHz which compares favourably to the accepted linewidth of 5.87 MHz for the transition. The large error is due to the comparatively noisy data, and some laser intensity fluctuation which accounts for the fractional absorption not reducing to zero in figure 3.9.

Indeed this shows how the current locking removes the effect of frequency jitter on our master laser, as described in section 3.2.1. The absorption beam was initially taken from the undeflected portion of the slave laser AOM (as shown in figure 3.2), and then

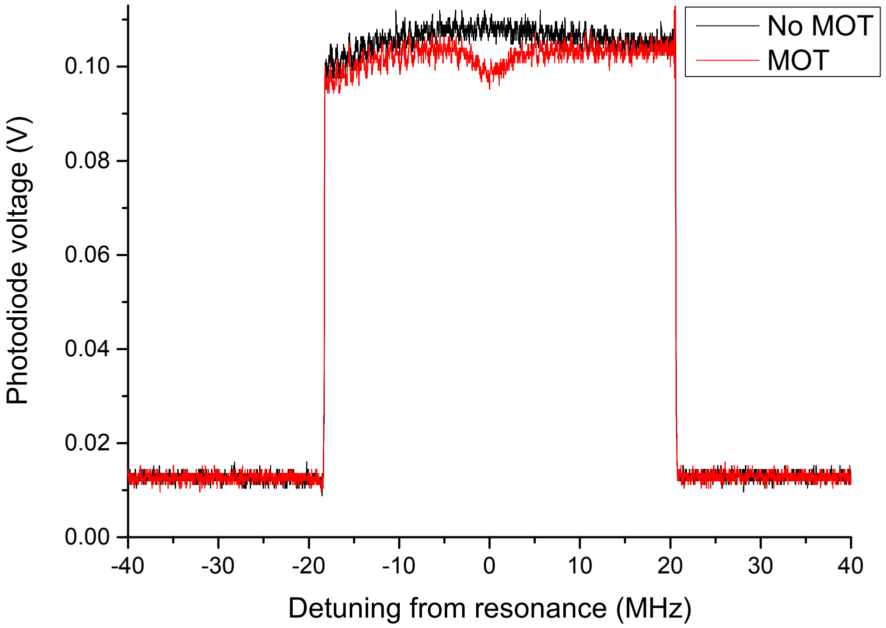

Figure 3.8: Graph showing absorption of light through the MOT cloud. Here, the light is pulsed on and swept through in frequency. The dip in the red curve corresponds to absorption when the beam is on resonance.

passed through a separate AOM to bring the detuning of the beam from -160 MHz back to resonance. In this way, the stability of the absorption beam directly reflects on the stability of the cooling beams.

If the master was locked using the lower bandwidth piezo locking, then the absorption profile is smeared out over an extra 10 MHz. As such, the dip equivalent to that observed in figure 3.8 is extremely difficult to make out. Absorption imaging was not possible at all with piezo locking.

Using these absorption imaging techniques, we calculate the MOT atomic number to be $(2.7\pm0.4)\times10^5$ at a density of $(4.6 \pm 0.6) \times 10^9/\text{cm}^3$. While this value is slightly lower than the case calculated during fluorescence imaging, this can possibly be attributed to an under-estimation of the light loss through the imaging optics or a slight error in measurement of the width of the atomic cloud.

It should also be noted that these density measurements provide only one example of the density at a given time. In practice, the density varied from $\sim 10^9$ to $\sim 10^{10}/\text{cm}^3$ and depended on various parameters such as the strength of the MOT magnetic field and the size and alignment of the cooling beams.

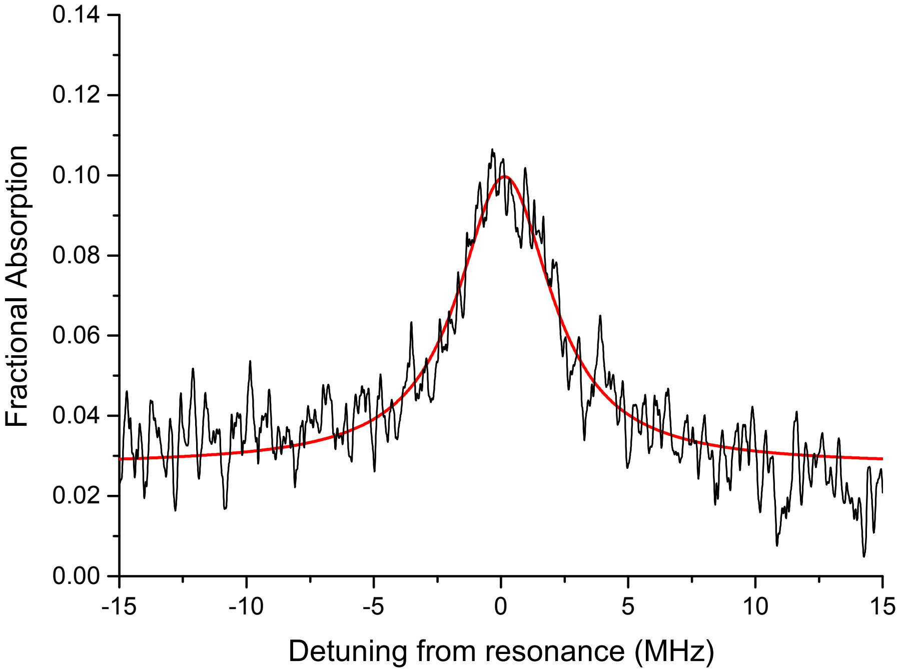

Figure 3.9: Graph of fractional absorption against detuning. A Lorentzian curve was fitted to the data to give a linewidth of 5±1 MHz.

3.2.4 MOT lifetime

As with any MOT, there is only a limited lifetime during which atoms can be trapped. This is primarily due to two main factors: collisions with "hot" background gases and intra-trap collisions. During an intra-trap collision, both metastable atoms are lost in either a Penning or an associative ionisation process:

$$\text{Penning: } Ar^* + Ar^* \rightarrow Ar + Ar^+ + e^- \tag{3.14}$$

$$\text{Associative: } Ar^* + Ar^* \rightarrow Ar_2^+ + e^- \tag{3.15}$$

While background losses can be reduced by ensuring a low vacuum pressure, intra-trap collisions are strongly density dependent and limit the maximum attainable density of the MOT. By taking a lifetime curve of the MOT, we can calculate the contribution of background and intra-trap losses. To do this we can model loss from the MOT by a differential equation:

$$\dot{\rho_e} = -\Gamma\rho_e(t) - \gamma_{ee}\rho_e(t)^2, \tag{3.16}$$

where ρ_e is the density of trapped metastable atoms, Γ is the one-body loss coefficient (i.e. mostly caused by collisions with background atoms) and γ_{ee} is the two-body loss coefficient (caused by metastable intra-trap collisions). If the effective trap volume is not time-dependent, the density of trapped atoms is given by

$$\rho_e(t) = \frac{\Gamma \rho_e(0) e^{-\Gamma t}}{\gamma_{ee} \rho_e(0)(1 - e^{-\Gamma t}) + \Gamma}, \tag{3.17}$$

where $\rho_e(0)$ is the initial density of metastable atoms.

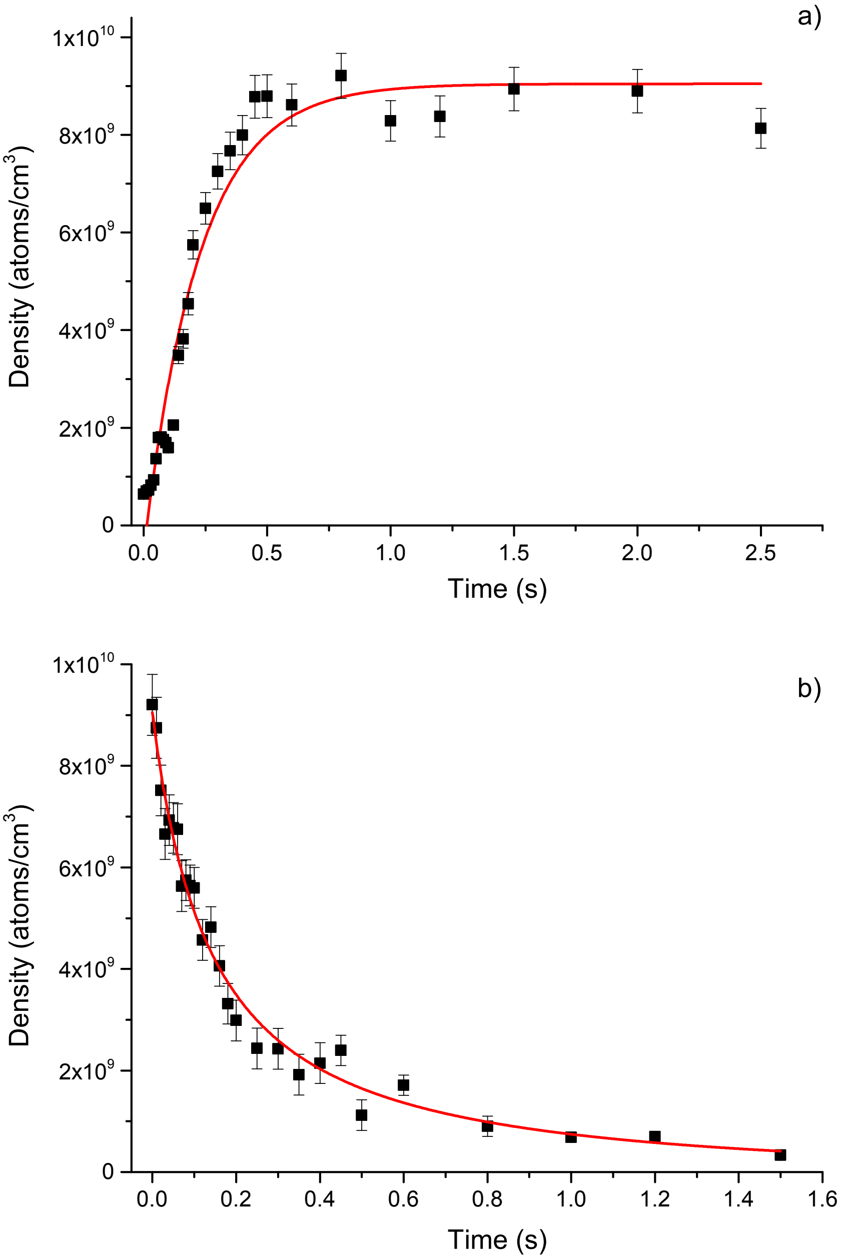

Figure 3.10: a) shows a typical MOT loading curve. Here we can see that the MOT takes ~ 0.5 seconds to load fully. The fit is a simple exponential curve to guide the eye. b) shows a typical lifetime curve. Loss from the trap is predominantly due to ionising intra-trap collisions and due to background gases. Equation 3.17 is used to fit the curve to the data.

Figure 3.10 shows a typical loading and lifetime curve of the MOT. The loading curve was simply taken by switching on all relevant cooling beams and the MOT magnetic field and then taking a fluorescence image after a variable loading period. The loading curve was taken by first allowing the MOT to reach maximal density and then shuttering both the atomic beam and Zeeman slower beam. After a variable period of trapping, the remaining atoms were counted by fluorescence.

As can be seen from the figure, the MOT takes ∼0.5 seconds to load fully. This is important to be noted for future experimental timing sequences. Equation (3.17) was fitted to figure 3.10 b) and allowed us to calculate the contribution of background and intra-trap collisions to the overall lifetime. From this fit, we established a one-body loss coefficient of 0.8±0.2 s^{-1} and a two-body loss coefficient of $(7 \pm 1) \times 10^{-10}$ cm^3s^{-1}. Using these numbers we can calculate the lifetime limitation of solely intra-trap collisions (which is equal to $1/(\gamma_{ee}\rho_e)$) to be ∼160 ms. In comparison, collisions with background gases limit the lifetime to $1/\Gamma = 1.25$ s. From this, we can see that intra-trap ionisation processes dominate the initial loss from the MOT.

Our two-body loss coefficient, γ_{ee}, compares favourably to the only previously measured value[80] of $(5.8 \pm 1.7) \times 10^{-10}$ cm^3s^{-1}. Both our measured value and this value, however, were taken in MOTs with no extrapolation to vanishing cooling beam intensity. This may explain the small difference between these two values as the cooling beam intensity was likely different for both experiments.

In chapters 6 and 7 we will discuss this in much greater detail. As our experiment has the ability to trap atoms "in the dark" at far-off-resonance frequencies, we can monitor the loss from the trap in a similar way without the influence of light-assisted collisions.

3.2.5 Temperature

It was important to characterise the temperature of the atoms within the MOT to estimate the well depths required for dipole trapping of them. A time-of-flight expansion technique[114] was used to calculate the temperature within the MOT. To do this, we load the MOT fully and simultaneously switch off the atomic beam, all cooling beams and the MOT magnetic field. We then monitor the width (by fluorescence) of the expanding clouds over a period of time. The atomic cloud expands over time as:

$$\sigma^2(t) = \sigma_0^2 + \frac{k_B T}{m} t^2 \tag{3.18}$$

where $\sigma(t)$ is the $1/e^2$ radius of the atomic cloud at time t, σ_0 is the initial radius, T is the temperature of the trapped atoms and m is the atomic mass of the trapped species (40 a.u. for argon).

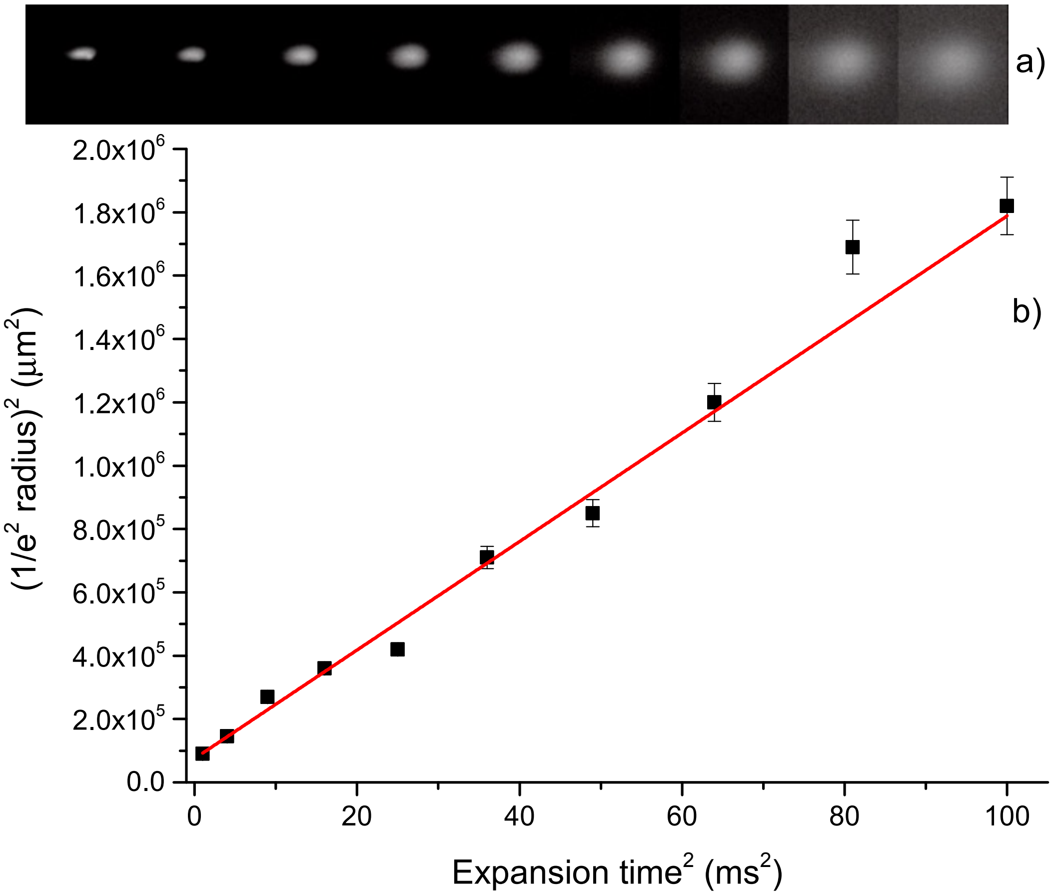

Figure 3.11: a) shows some typical fluorescence images that show expansion of the atomic cloud over time. b) shows a plot of the $1/e^2$ radius squared against the expansion time squared. A linear fit is added to the data, and the gradient of $k_B T/m$ allows us to calculate the temperature of the atomic cloud to be 82±4 μK.

Figure 3.11 shows the result of a typical time-of-flight expansion temperature measurement. Part a) displays the fluorescence images that were taken at 1 ms intervals. Here we can see not only the expansion of the atomic cloud, but also that the cloud begins to fall under the influence of gravity. Gaussian profiles were obtained from each image and were used to calculate values of the $1/e^2$ radius. Figure 3.11 b) shows the result of calculating the radii at various times and gives a plot of the $1/e^2$ radius squared against the expansion time squared. As can be seen a linear fit is added to the data. By using equation (3.18) we can see that the gradient of this fit is equal to $k_B T/m$ and allows us to measure the temperature of the atomic cloud to be 82±4 μK. This temperature, while still lower than the Doppler limit, is larger than a previously measured value[115] of ~40 μK taken in a MOT with similar parameters. This increased temperature is possibly due to frequency noise on the cooling lasers.

It should be noted that during the acquisition of this data the background magnetic field needed to be as close to zero as possible. If a significant background magnetic field was present then, during the process of switching off the MOT cooling beams, the background field would cause a "kick" to be given to the trapped atoms. This is due to the stray fields causing a Zeeman shift which, in turn, leads to an unbalanced scattering force between the retro-reflected σ^+ and σ^- beams. To prevent this, the currents into the three compensation coils as described in section 3.1.4 were carefully tuned until the MOT expanded symmetrically and slowly, with no undesired "kick".

Chapter 4

CO_2 laser dipole trap

This chapter describes the trapping of metastable argon in a single beam dipole trap, formed by the focussed output of a CO_2 laser. This experiment was designed to give us a more simple trapping environment than in the case with an optical build-up cavity; and therefore work out any complexities with trapping. Initially it was jointly set up with Dr. Conor Maher-McWilliams[107], with the author of this thesis in sole charge of the experiment once the first trapping signal was detected.

4.1 Introduction

CO_2 lasers often make ideal candidates for the trapping of atoms as they produce powerful, stable outputs[15,16]. Moreover, the wavelength output (10.6 μm) is far detuned from atomic resonances. As the optical scattering rates scale as $\Gamma \propto U_0/\Delta^2$ (where U_0 is the well depth of the trap, and Δ is the detuning from atomic resonance), this means that the scattering rates are extremely low and are typically of the order of 10^{-3} photons per atom per second.

For the case of a CO_2 laser, the detuning is so large that the trap can be considered to be quasi-electrosatic and any optical heating is negligible. The potential, U, of a quasi-electrostatic trap is given by

$$U = -\frac{1}{2}\alpha_{\text{stat}}E(x, y, z)^2 \tag{4.1}$$

where α_{stat} is the static polarisability of the trapped particle, and $E(x, y, z)$ is the electric field distribution of the light field. For the case of a trap formed within a single focussed laser beam, the optical potential can be written as:

$$U(r,z) = -\frac{\alpha P}{\pi \epsilon_0 c w^2(z)} \exp\left(-\frac{2r^2}{w^2(z)}\right) \tag{4.2}$$

Here, the incoming beam is Gaussian and the waist is described along the z axis by $w(z) = w_0\sqrt{1-(z/z_R)^2}$ where z_R is the Rayleigh range and is equal to $\pi w_0^2/\lambda$. The power of the trapping beam is P, and r is the radial coordinate.

A CO_2 laser fulfils the criteria of having both large detuning and high powers. They have been shown to produce very stable outputs[15,16] which do not limit trap lifetimes by parametric excitation out of the trap[116,117]. They have therefore been used in various cold atom trapping experiments[18,25,26].

4.2 The CO_2 laser

The laser itself was a Coherent DEOS GEM Select 100, which was bought second-hand from Durham University and previously used for dipole trapping of Rb[118,119]. The same kind of laser (also a Coherent DEOS laser) was subject to extensive stability testing by Michael Gehm[120]. For trap frequencies up to 7 kHz it was found that $1/\Gamma \gtrsim 10^4$ s, making the laser an ideal candidate for atomic trapping.

The power output was measured to be ~120 W, and a Gaussian spot-size of 3.8 mm was produced. The laser's discharge was powered by a water-cooled 2 kW power supply (Coherent Deos D1000L), which was itself powered by a 35 V, 60 A power supply (Agilent 6573A). As the most commonly used optical materials strongly absorb beams in the far-infrared, Zinc Selenide (ZnSe) lenses and windows were used throughout the path of the trapping beam.

4.3 Optical layout

The optical path was comparatively simple, and is shown in figure 4.1. The beam inside the CO_2 laser itself became misaligned over time and damaged some internal mirrors. The damaged mirrors were therefore removed, and the output aperture of the laser was moved from the front of the laser to the side. An opening was drilled through the side of the laser, and was covered using a ZnSe window. The CO_2 laser was raised to approximately the height of the MOT cloud itself, and so very little vertical adjustment of the beam path was required.

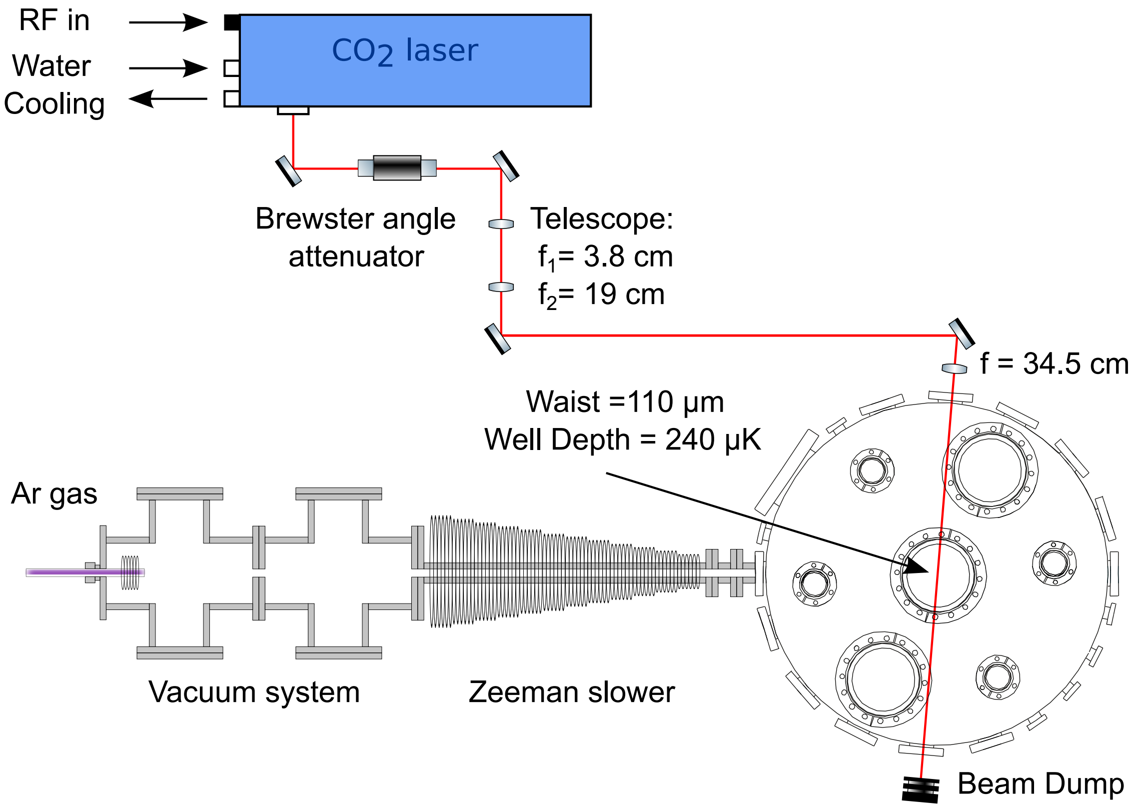

Figure 4.1: Optical layout of the CO_2 laser dipole trap.

A Brewster angle attenuator was used to permit easy control over the power of the beam, and therefore the trapping well depths. To allow us to get the smallest possible focus, the beam was first expanded by a telescope to a diameter of 1.9 cm. This beam was then directed towards the science chamber and focussed towards the MOT cloud by a lens of focal length 34.5 cm. This focussing lens was mounted onto a three-dimensional translation stage, so that the position of the focus could be easily adjusted. Once the beam has passed through the trapping chamber, it is absorbed by a high-power beam dump.

4.4 Alignment process

Although the optical alignment consists of only a few optics, the actual alignment of a CO_2 laser is more complex. As the power of the beam was high, one had to be careful of the associated dangers. Moreover, detection of the position of the beam is problematic due to its far-infrared wavelength. It also would not be generally safe to align the laser at full power, so the first issue was how to reduce the power of the beam. The Brewster angle attenuator was not able to turn down the power sufficiently for safe alignment. It also became very hot if it was attenuating the beam too much, and so had to be cooled by a powerful fan.

To reduce the power further, we ran the RF power that was supplied to the laser discharge on a low duty cycle. A TTL signal at 10 Hz was sent to a control pin on the RF power supply. By adjusting the length of the TTL signal, the average power could be adjusted anywhere from 0.1% to full power. While this method was useful for rough alignment, anything precise was problematic as the cavity takes several seconds to thermalise fully. When the RF power is reduced in this way, higher order TEM modes are present. For more precise alignment the CO_2 laser was run at 100% power and the Brewster angle attenuator was used to turn the power down, albeit to a lesser extent. In this way, the cavity can thermally stabilise to the correct length and only the TEM_{00} mode is present.

To detect where the beam was, a thermal imaging plate (Macken Instruments) was used. These work by using a thermally-sensitive phosphor which fluoresces when illuminated by ultraviolet light. The hotter the phosphor gets, the more intense the fluorescence becomes and so detection of a beam is straightforward.

To begin the alignment process, a HeNe laser was aligned along the approximate path (through the vacuum chamber and back to the CO_2 laser) that will be used for trapping. The CO_2 laser beam was then overlapped with this beam (using the thermal imaging plate) as precisely as possible.

As the Rayleigh range of the focus is only $\sim$3.7 mm, the first step in alignment was to characterise the position of the focus (including through the ZnSe window on the vacuum chamber). To do this we used a knife-edge technique, which simply involves mounting a razor blade onto a translation stage, and measured the power of the transmitted light as a function of the razor blade position. This was done at various points along the direction of beam travel to ascertain the distance of the focus from the lens itself. The beam was strongly reduced in power by using the Brewster angle attenuator.

Figure 4.2 shows the knife-edge measurement at the focus of the beam. To fit the curve to the data, we assumed the beam was Gaussian and used the following equation to give the power of the beam that was unobscured by the razor blade:

$$P = \frac{P_0}{2}\left[1 - \mathrm{Erf}\left(\frac{\sqrt{2}}{w}(z - z_0)\right)\right]. \tag{4.3}$$

Here, P_0 is the power of the full beam, Erf is the error function, w is the $1/e^2$ beam radius and z_0 is the position of the centre of the beam. By fitting this to the data, we found the radius of the beam to be 112±3 μm. Perhaps more importantly, we also determined that the focus of the beam was 35.8 cm from the focussing lens. This could be due to either the beam not being perfectly collimated, or caused by the passage of the beam through the vacuum window.

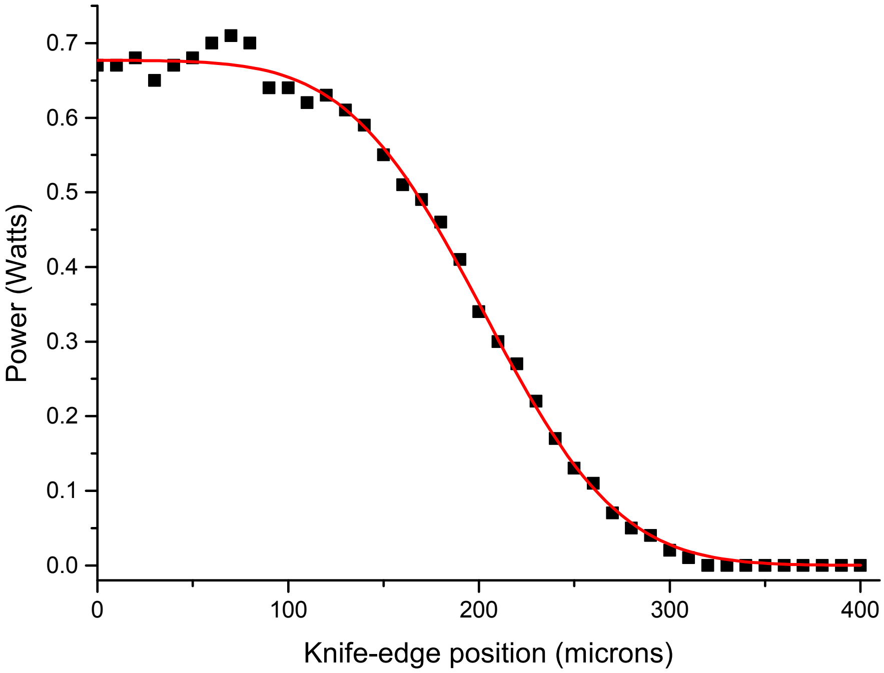

Figure 4.2: Knife-edge measurement of the focus of the trapping beam. The waist was measured to be 112±3 μm, calculated by fitting equation 4.3 to the data.

Once the distance of the focus from the lens had been determined, overlap of the trapping beam with the MOT cloud was challenging. In many of these types of experiments, alignment is achieved by keeping all of the MOT cooling beams turned on and moving the trapping beam until a Stark shift can be witnessed through the MOT cloud. This Stark shift causes the MOT cooling beams to be shifted off resonance and so manifests itself as a dark stripe through the detected fluorescence of the MOT.

In our case, as the polarisibilites of the both the closed cycle cooling levels $4s[3/2]_2$ and $4p[5/2]_3$ are very similar, the Stark shift was only of the order of several hundred kHz. This was not sufficient to observe a stripe through the MOT, and so the only way to tell if the trap was aligned was to actually load the trap itself and image the trapped atoms by fluorescence. In practice, the focussing lens was systematically translated in a grid until a trapping signal was detected (initially after a trapping period of only 5 ms so there was a large signal). This signal was then peaked up by adjusting the position of the lens in all three directions and also adjusting the experimental timings.

4.5 Experimental timing

As we already discussed in section 3.1.5, all experimental timing is controlled by a Quantum Composer 9520 digital delay pulse generator. The timing sequence for loading and imaging the trap is briefly summarised in table 4.1. We first start by loading the MOT for 2.5 seconds by turning on the MOT cooling beams, magnetic field coils, Zeeman slower, and atomic beam. The atoms are then subjected to a 5 ms optical molasses phase, before which the MOT beams are then turned off and a period of trapping within the CO_2 beam occurs. Untrapped atoms expand freely out of the trapping region. To image the atoms afterwards, the MOT beams are simply turned back on and a TTL trigger signal is sent to the EMCCD camera to detect the atoms by fluorescence. Exposure times for the imaging varied from 1 to 5 ms. The timing sequence is repeated to average over 20 fluorescence images for each trapping time.

	MOT loading (2.5 s)	Molasses phase (5 ms)	Variable trapping time	Imaging (1-5 ms)
MOT beams	▨	▨		▨
MOT mag. field	▨			
Zeeman slower	▨			
Atomic beam	▨			
Trapping beam	▨	▨	▨	▨
Camera trigger				▨

Table 4.1: Experimental timing of loading metastable argon into the CO_2 laser dipole trap. Here, the shaded cells depict periods when a piece of apparatus is turned on.

It should be noted that during these times, the CO_2 laser trapping beam is always on. This is, firstly, because the trapping beam has no adverse effect on the operation of the MOT while it is on. Secondly, we initially acquired an AOM to use with this experiment so we could rapidly shutter the trapping beam to turn the trap on/off. We found, however, that as the AOM changed in temperature it significantly moved the position of the beam further down the beam path. This was despite the AOM being water-cooled by a chiller, and so we decided to abandon using it and just keep the CO_2 laser on permanently.

4.6 Results and characterisation of the trap

Atoms were successfully loaded into the dipole trap using this method, and an example image of the trap is shown in figure 4.3. As can be seen, there is a streak of trapped atoms through the background halo of expanding MOT atoms. This presents a problem, as we have to be able to separate out the trapped atoms from those that are untrapped but still in the imaging plane.

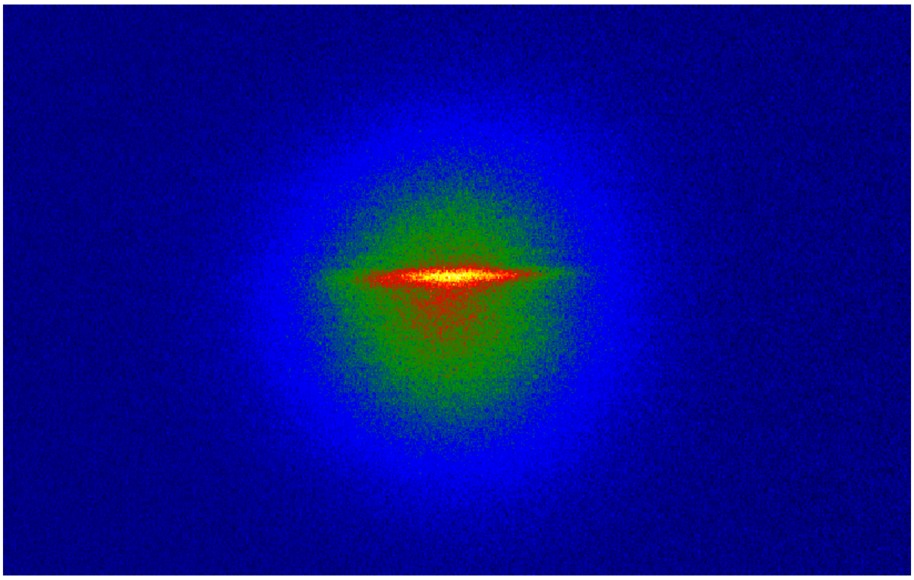

Figure 4.3: Example fluorescence image of the CO_2 laser dipole trap after 10 ms of trapping. The streak at the centre of the image depicts the trapped atoms, while the halo of atoms around the outside show untrapped MOT atoms which are expanding.

We used two methods to do this; firstly we simply took a cross-sectional profile of the atoms and fitted two Gaussian curves to it. The cross sectional profile of the image in figure 4.3 is shown in figure 4.4. From this we calculate (by taking the area under each individual Gaussian curve) that approximately 6% of the initial MOT atoms are loaded into the dipole trap (as opposed to a previously reported value of 43% for this experiment[107] which didn't take into account background MOT atoms). This value generally varied between 5 and 10% depending on factors like alignment of the trap and size of the MOT cloud. The width of the dipole trap was also determined to be 109±2 μm, which is consistent with the knife-edge measurement at the focus of the beam presented in figure 4.2.

Another method in which we managed to separate the atoms trapped in the dipole trap, and those that were not was to apply a "rolling ball" algorithm to the images. This technique is ideal for subtracting out relatively large and spatially varying backgrounds (which the expanding MOT cloud can be considered to be). Crudely stated, this algorithm

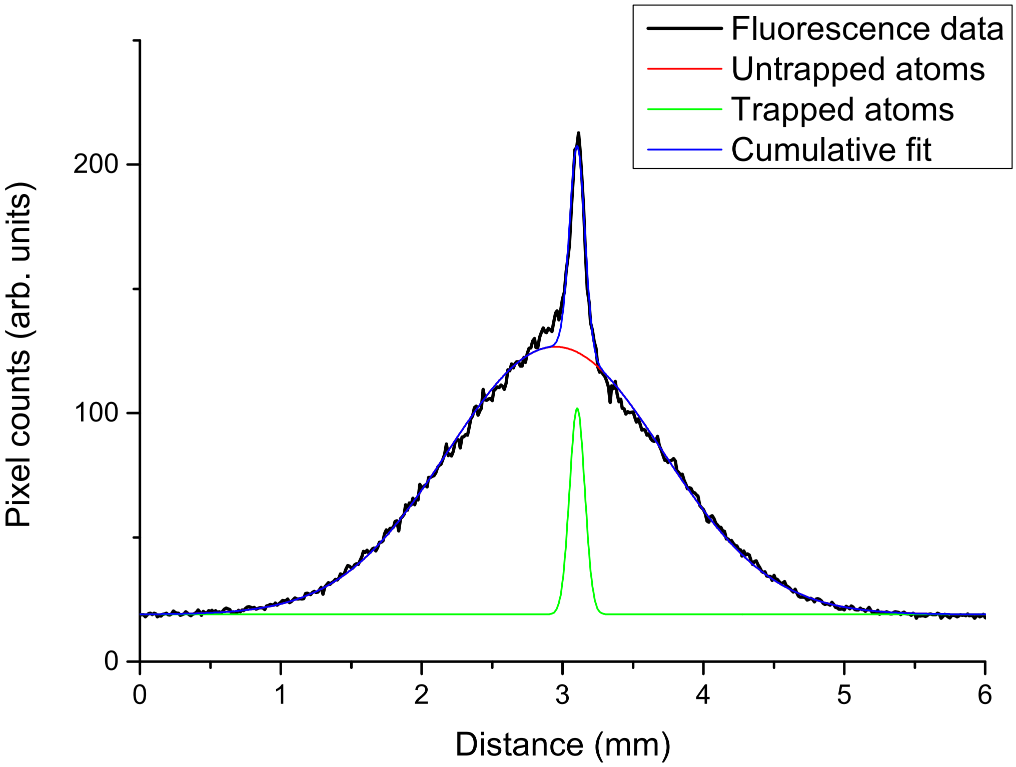

Figure 4.4: Cross-section of the dipole trap and the expanding untrapped MOT atoms. A multi-peak fit was applied to the data, and allowed us to ascertain that 6% of the MOT cloud was loaded into the trap.

works by "rolling a ball" around the image and simply subtracting anything away that the ball can fit/fall into. As such, details with smaller structure (like our dipole trap) are left intact while the larger background is subtracted.

To do this, we used a variant of the image processing software Image J called Fiji. This software comes pre-installed with the relevant plug-in to implement the "rolling ball" algorithm. Some care had to be taken over choosing the size of the "ball" to use. Too small and some of the information in the tails of the Gaussian distribution of the dipole trap might be lost. Too large and some background may remain. We settled on a "rolling ball" size of approximately 300 μm. The results of this are shown in figure 4.5. As can be seen, the application of this algorithm is very effective in reducing the background of untrapped atoms.

The next stage in characterisation of the trap was to take a simple lifetime curve. To do this, the trapping time was varied and at the end of each trapping period a fluorescence image was taken and the amount of trapped atoms counted. For each trapping time, 30 images with an exposure time of 2 ms each were accumulated and averaged to reduce any variation between the images. This was repeated 5 more times to verify reproducibility of

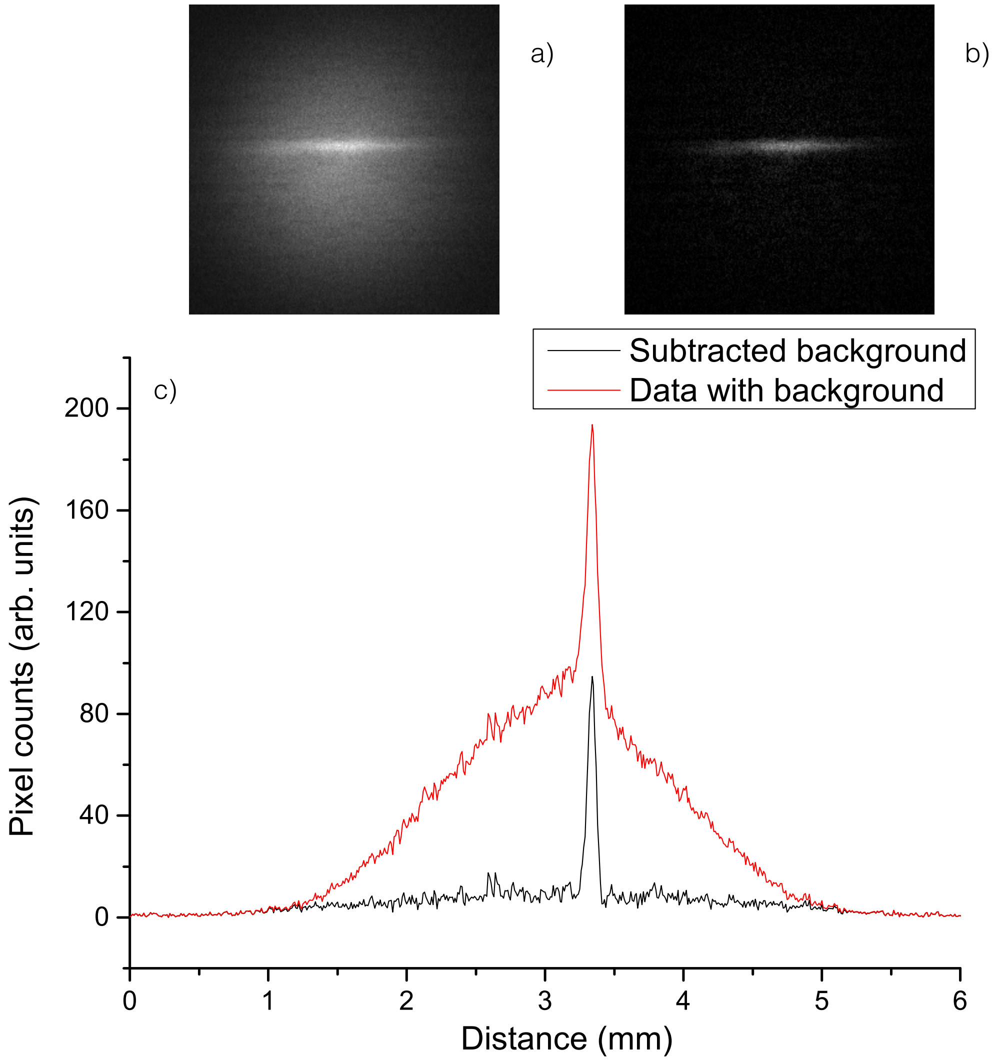

Figure 4.5: a) shows an example image of the trap before any compensation for the expanding MOT cloud was performed. b) shows the same image after a "rolling ball" algorithm was applied. The radius of the "ball" used was 300 μm. c) shows the transverse cross-section of each image.

results. The resultant lifetime curve is shown in figure 4.6.

As can be seen, the lifetime is surprisingly short and is equal to 16.3±0.2 ms. Initially, this short lifetime was thought to be due to Penning ionisation of the trapped atoms. However, upon comparison with the MOT lifetime (as shown in figure 3.10) this did not make much sense. This is particularly strange as although the density of the dipole trap starts off at a similar value to the MOT, the density soon reduces significantly as the trapped atoms spread out over the axial direction (as the Rayleigh range is large compared to the size of the trapped atom cloud). This spreading out of the atoms can be seen in figure 4.7.

Because of this, one would expect the lifetime to be substantially longer than that of

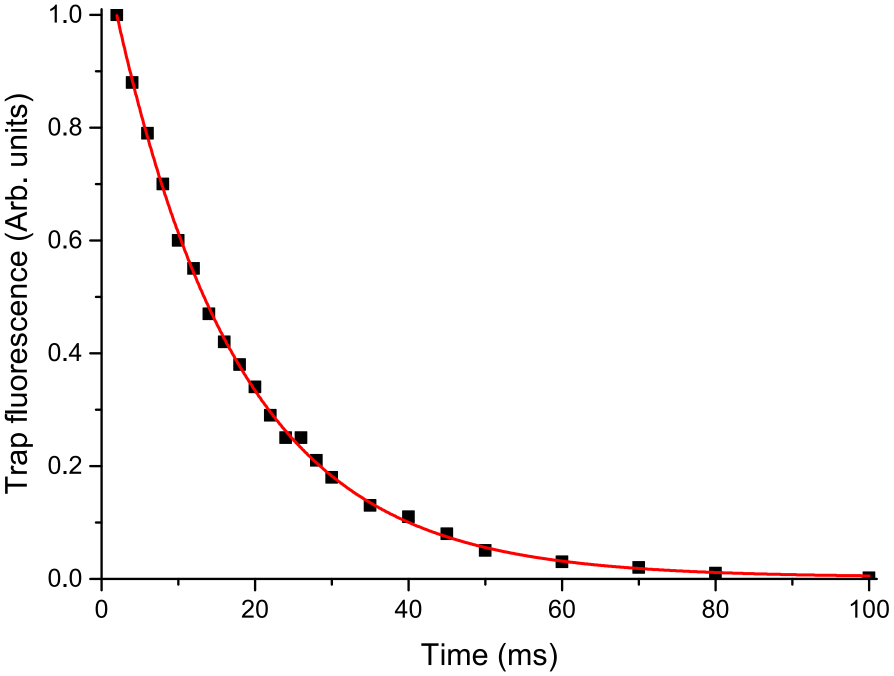

Figure 4.6: Lifetime curve of the CO_2 dipole trap, giving a lifetime of 16.3±0.2 ms. Error bars are smaller than the data points themselves.

the MOT. If equation (3.17) was fitted to this decay curve as it was for the MOT, the two body loss coefficient was several orders of magnitude larger than it should be. In this way, and as the background pressure is the same, neither background or intra-trap collisions can be responsible for the shortened lifetime.

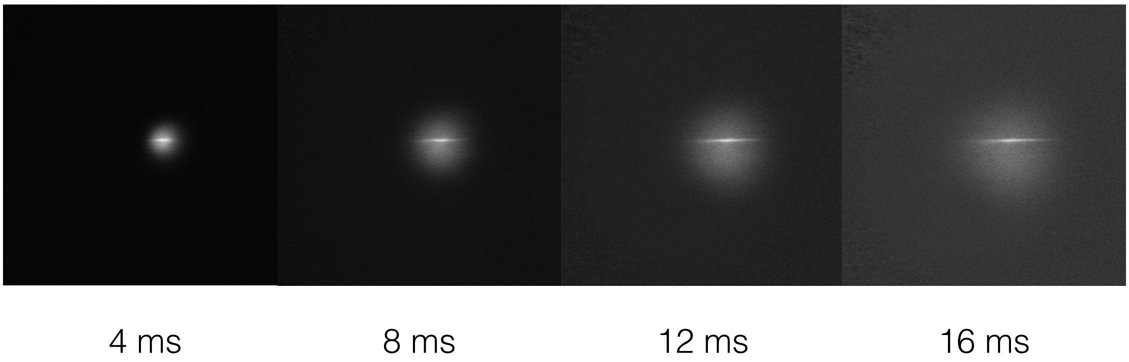

Figure 4.7: Graphic displaying the spreading out of the trapped atoms in the axial direction.

After further analysis, it became clear that some kind of artificial heating was responsible for this shortened lifetime. This was most likely to be of the form of parametric heating[116,117,121,122] caused by vibrations from turbo-molecular pumps. To confirm this we took a fast Fourier transform (FFT) of the MOT master laser beam frequency, which is shown in figure 4.8. As can be seen, there are two main resonances-at 1.4 and 2.2 kHz.

These are due to vibrations caused by the turbo-molecular vacuum pumps. Presumably there are two peaks as the different types and brands of pumps that are used in the experiment spin at different frequencies.

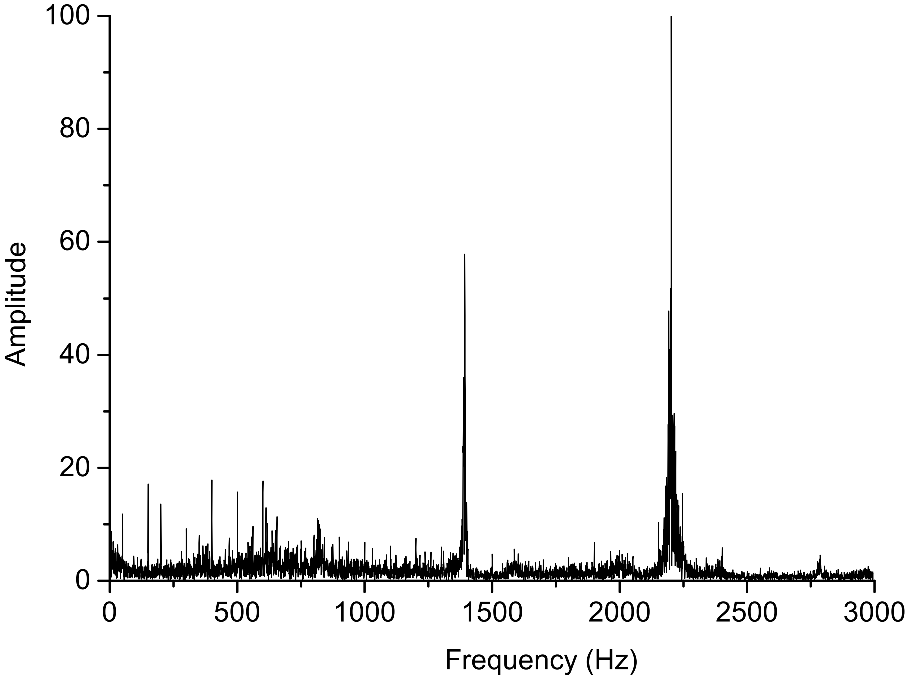

Figure 4.8: Fast Fourier transform of the MOT master laser beam intensity. The two main frequencies shown are due to vibrations to the optical table caused by the turbo-molecular pumps.

To take this data, the laser was scanned slowly (30 Hz) across resonance and the intensity monitored as the beam was passed through the RF discharge. In this way, faster fluctuations can be monitored. The sampling time of the FFT data was 0.1 ms, and over 10 s worth of data was analysed.

While these fluctuations were no longer a problem for the MOT beams, as a lock with a higher bandwidth than the vibrations was implemented (as described in section 3.2.1), they could well vibrate the internals of the CO_2 laser or indeed any of the trapping optics before the dipole trap itself. As such, while it is perhaps unlikely that the frequency itself of the CO_2 laser would be affected, the position of beam focus could fluctuate at these frequencies and end up exponentially heating atoms out of the trap.

To verify that these frequencies could cause such parametric heating, we can theoretically estimate the trap frequencies of the dipole trap. To do this we note that a cylindrically symmetrical harmonic oscillator has a potential of the form

$$U(r,z) \approx -U_0 \left(1 - 2\frac{r^2}{w_0^2} - \frac{z^2}{z_R^2}\right) \tag{4.4}$$

where we have assumed that the temperature of the trapped atoms is much less than the well depth created by the trap ($T << U_0/k_B$). The axial and radial trap frequencies can also be written as

$$\omega_{\text{axial}} = \sqrt{\frac{2U_0}{mz_R^2}} \tag{4.5}$$

and

$$\omega_{\text{radial}} = \sqrt{\frac{4U_0}{mw_0^2}}. \tag{4.6}$$

Given that focus of the trapping beam was measured to be 112 μm and that the power of the trapping beam was measured to be 62.5 W on exit from the science chamber (as measured by a water-cooled power meter from Coherent, part no. 0217-722-00) we can obtain an estimate for both trap frequencies. Putting these numbers into equations (4.5) and (4.6) we calculate the trap frequencies to be $\omega_{\text{axial}} = 2\pi \times 13.5$ Hz and $\omega_{\text{radial}} = 2\pi \times 635$ Hz.

With these calculations, we can see that the 1.4 kHz peak in figure 4.8 is very close to twice the radial trap frequency (at 1.27 kHz). This is significant as parametric excitation is enhanced at twice a trap frequency and so, even if the modulation is slight, the trap lifetime would be significantly limited by this. Moreover, as the power of the trapping beam was measured after the exit window of the science chamber we could expect the trap frequency to be slightly higher than estimated. The window used on the beam exit was previously used in Rb trapping experiments[118,119] and still contained Rb deposits, which would attenuate the beam and bring the trap frequency even closer to the 1.4 kHz noise from the vacuum pumps.

These trap frequencies could have been measured experimentally, but the atoms did not remain trapped for long enough to measure the frequency axially and technical limitations did not allow us to measure them radially. To do this axially, the trap simply needs to be loaded slightly away from the focus of the trap and oscillations of the trapped atoms will be excited in that direction. Radial oscillations can be excited by turning the trap off for a short period and then re-capturing the atoms. Unfortunately, for the set-up of this experiment we had no way of rapidly switching the trap on and off and so could not perform this measurement.

A couple of techniques were attempted in order to try and reduce the effect of this heating out of the trap. Firstly, all mirrors and lenses were mounted on thick posts in vibrationally insensitive mounts. Secondly, the turbo-molecular pumps were mounted onto vibration isolating dampers (Turbo-V vibration dampers-Agilent Technologies) to attempt to reduce the amount of vibrations that were coupled to the optical table.

Unfortunately, despite these attempts, vibrations were still being coupled onto the optical table and onto the optics throughout the CO_2 laser beam path. The lifetime measured increased to around 20 ms, but could not be extended further.

4.7 Conclusions

During this chapter, we have discussed the creation and loading of a dipole trap formed within the focus of a high-power CO_2 laser beam. The focus was successfully overlapped with the MOT cloud and up to 10% of the atoms were loaded into the trap. The trap lifetime was artificially limited to times of less than 20 ms due to parametric excitation out of the trap. This was due to vibrations being coupled to the optical table from the turbo-molecular pumps.

To overcome the influence of vibrations, some kind of position-detecting photodiode would have been required and a feedback loop set-up with a piezo-controlled mirror to compensate for movement of the beam. Moreover, the photodiode would have to be sensitive to the far-infrared (e.g. a mercury cadmium telluride photodiode). Because of the technical (and the cost of implementing such a scheme) difficulties of something like this a decision was made to now trap using the original plan of using an optical build-up cavity at 1064 nm. Such a cavity would have the ability to achieve much deeper well depths (necessary for the trapping of ground state whose polarisability is much less than metastable argon). The construction and set-up of such a cavity is described in chapter 5.

Chapter 5

Far-off resonance build-up cavity: theory

Optical dipole traps which utilise the Stark effect to spatially confine atomic and molecular species are an important tool in cold atomic physics[13,18,123]. However, as the Stark effect is a weak interaction, light of high intensity is often required to trap atoms or molecules for long periods. This thesis outlines two separate ways of achieving the required intensity. The first involves a single beam dipole trap (as already described in chapter 4), created from the output of a high power laser. The second uses an optical cavity to amplify input intensities to the level required for trapping. This chapter outlines the theory behind the latter option.

5.1 Fabry-Perot resonators

Simply stated, an optical cavity consists of two (or more) highly reflective mirrors between which correctly aligned light can reflect back and forth multiple times. These reflections create standing wave patterns (modes) for various resonant frequencies. As little light leaks out of the cavity, it can store and accumulate photons over time and therefore lead to a build up in intensity of the light.

The most simple case of an optical cavity is that of the Fabry-Perot resonator. In this, there are two plane parallel mirrors, a distance L apart, with reflection coefficients r_1 and r_2 and transmission coefficients t_1 and t_2 respectively. We can assume an electromagnetic wave of electric field E_{in}, frequency ω and wave-vector $k = w/c$ enters the cavity. Multiplying E_{in} by the reflection coefficient of the first mirror gives the electric field reflected from it ($E_{in}r_1$). Similarly, to determine the field transmitted by the second mirror we multiply E_{in} by the transmission coefficients for each of the two mirrors: $E_{in}t_1t_2$. The same can be done to calculate the field after many round-trips of the resonator, as shown in figure 5.1.

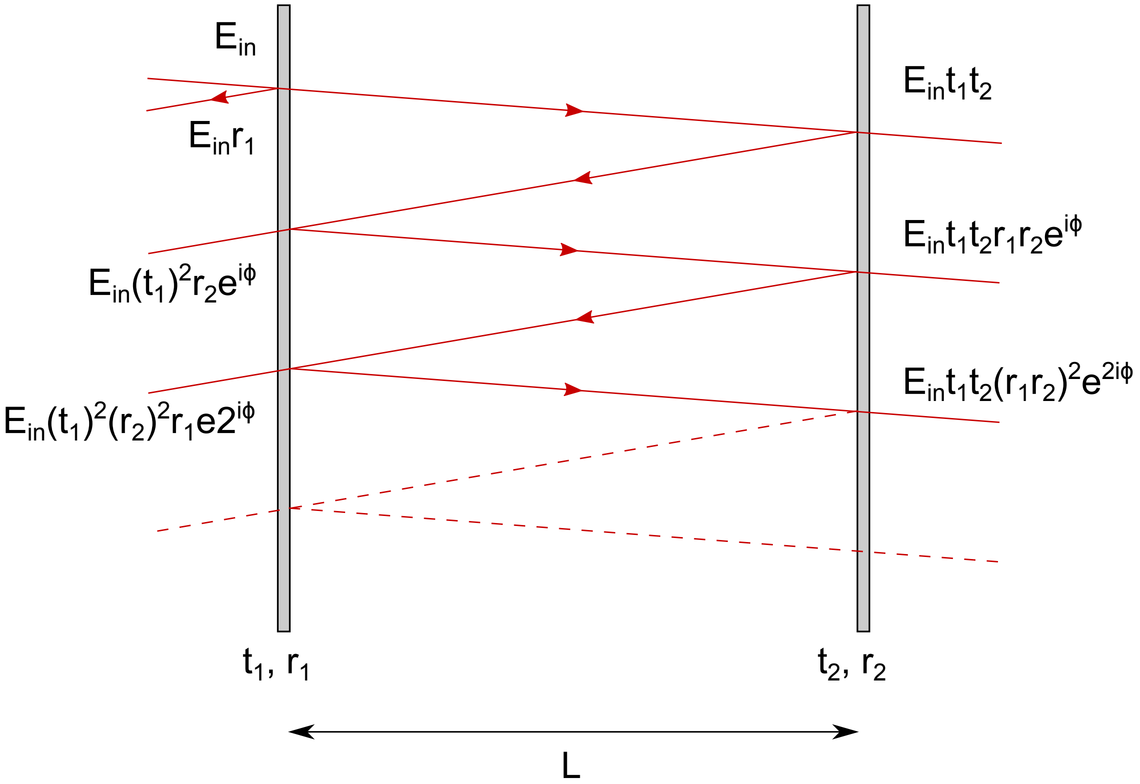

Figure 5.1: Misaligned light entering a Fabry-Perot resonator, with amplitude reflectivities r_1 and r_2 and amplitude transmittivities t_1 and t_2.

The transmitted field, E_t, is simply the sum of all individual components emerging from the second mirror:

$$E_t = E_{in}t_1t_2(1+r_1r_2e^{i\phi}+(r_1r_2)^2e^{2i\phi}+...) = E_{in}t_1t_2\sum_{n=0}^{\infty}(r_1r_2e^{i\phi})^n = E_{in}\frac{t_1t_2}{1-r_1r_2e^{i\phi}} \quad (5.1)$$

where ϕ is the phase difference picked up by the beam on each round-trip of the cavity. The reflected field, E_r, can be similarly determined:

$$E_r = E_{in}\left(r_1 + t_1^2r_2e^{i\phi}\sum_{n=0}^{\infty}(r_1r_2e^{i\phi})^n\right) = E_{in}\left(r_1 + t_1^2\frac{r_2e^{i\phi}}{1-r_1r_2e^{i\phi}}\right) \quad (5.2)$$

To calculate the transmitted intensity, I_t, the square of the magnitude of the electric field is taken:

$$I_t = |E_t|^2 = E_{in}^2 \left| \frac{t_1 t_2}{1 - r_1 r_2 e^{i\phi}} \right|^2 = I_{in} \frac{(t_1 t_2)^2}{(1 - r_1 r_2)^2} \frac{1}{1 + \frac{4 r_1 r_2}{(1 - r_1 r_2)^2} \sin^2\left(\frac{\phi}{2}\right)} \tag{5.3}$$

where $I_{in} = E_{in}^2$. At this point we can simplify the expression by introducing a term called the finesse coefficient, F:

$$F = \frac{4 r_1 r_2}{(1 - r_1 r_2)^2} \tag{5.4}$$

which leads to an expression called the 'Airy function', and is plotted in figure 5.2:

$$I_t = I_{in} \frac{(t_1 t_2)^2}{(1 - r_1 r_2)^2} \frac{1}{1 + F \sin^2\left(\frac{\phi}{2}\right)} \tag{5.5}$$

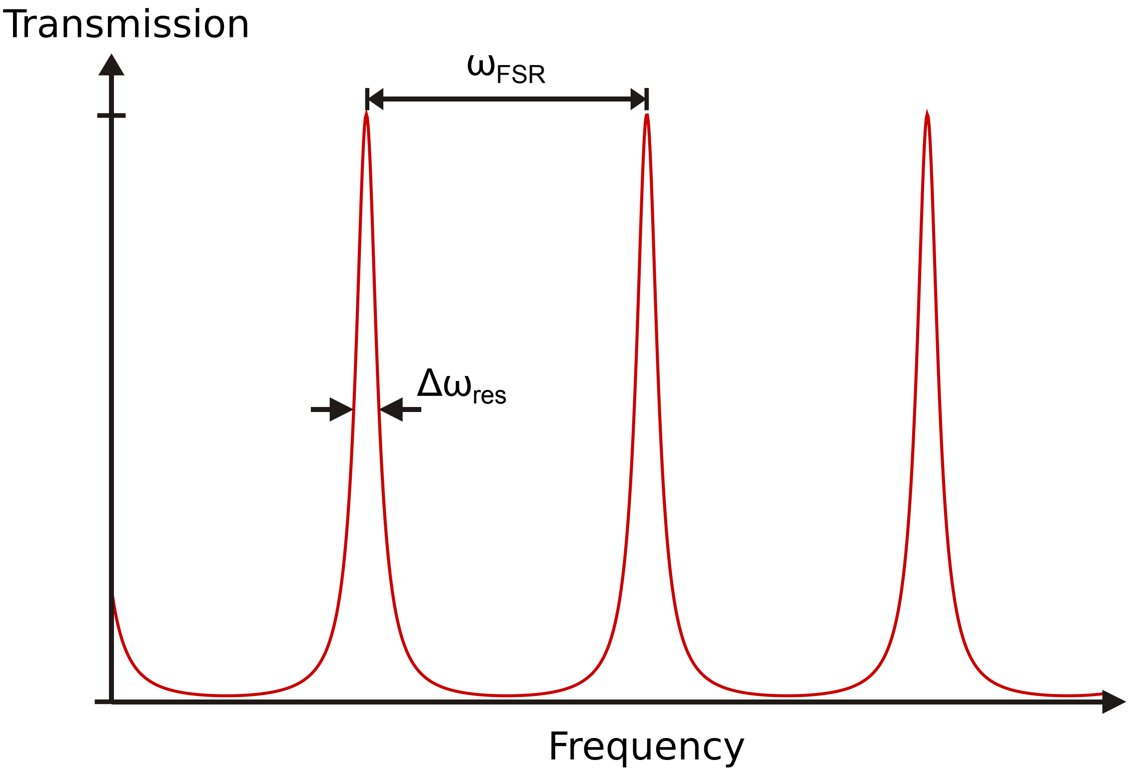

Figure 5.2: The Airy function. Here we can see the periodic resonances as we scan the Fabry-Perot resonator in frequency.

For an optical resonator $\sin^2(\phi/2)$ is zero (as at resonance ϕ=0). This leads to maximum transmission occurring when $\frac{2L}{c}\omega = 2\pi q$, where q is any integer. Therefore the resonant frequencies occur when

$$\omega_{\text{res}} = 2\pi \frac{c}{2L} q = 2\pi \omega_{FSR} q, \tag{5.6}$$

where $\omega_{FSR} = \frac{c}{2L}$ is known as the free spectral range, and is the frequency spacing between successive maxima. The linewidth of the resonances can also be determined as

$$\omega_{\text{res}} = \frac{\omega_{FSR}}{F} \tag{5.7}$$

In practice, losses occur over each round-trip of the cavity. To take this into account we must use the generalised finesse coefficient instead of the coefficient F given by equation (5.4). Note that for the next set of derivations I will switch to using the amplitude reflectivity and transmissivity, R and T, instead of the reflection and transmission coefficients, r and t. They are related by $r = \sqrt{R}$ and $t = \sqrt{T}$. This is just for ease of derivation. The generalised finesse coefficient can therefore be written as

$$F_A = \frac{4\sqrt{R_1 R_2 (1-(l_1+l_2))}}{\left[1-\sqrt{R_1 R_2 (1-(l_1+l_2))}\right]^2} \tag{5.8}$$

where l is the loss per mirror (including both absorption, A, and scatter, S), so that $l = A + S$. We can again calculate the transmitted intensity:

$$I_t = I_{in} \frac{T_1 T_2 (1-(l_1+l_2))}{(T_1+T_2+l_1+l_2)} \frac{1}{1+F_A \sin^2\left(\frac{\phi}{2}\right)} \tag{5.9}$$

As we have already discussed, in the case of a resonator the phase difference ϕ is zero and so we obtain:

$$\frac{I_t}{I_{in}} = \frac{4T_1 T_2 (1-(l_1+l_2))}{(T_1+T_2+l_1+l_2)^2} \tag{5.10}$$

A mode-matching factor ϵ should be included in this equation, as there are more losses during the mode-matching process. Moreover, the expression can be simplified by using a quantity called the finesse[124] (to be distinguished from the finesse coefficient):

$$f = \frac{2\pi}{L} = \frac{2\pi}{T_1+T_2+l_1+l_2} \tag{5.11}$$

where L denotes the total losses on each round trip of the cavity. We therefore get the following expression:

$$\frac{I_t}{\epsilon I_{in}} = 4T_1 T_2 (1-(l_1+l_2)) \left(\frac{f}{2\pi}\right)^2 \tag{5.12}$$

To obtain the intensity circulating inside the resonator, we can use the simple equation $I_{res} = I_t/T_2$. The build-up factor G inside the cavity, is given by:

$$G = \frac{I_{res}}{I_i} = 4T_1\epsilon(1-(l_1+l_2))\left(\frac{f}{2\pi}\right)^2 = \frac{4T_1\epsilon(1-l_1-l_2)}{(T_1+T_2+l_1+l_2)^2} \tag{5.13}$$

It is this factor that makes optical cavities attractive to use as dipole traps. The intra-cavity power can be orders of magnitude higher than the input into the cavity.

5.2 Cavity locking with the Pound-Drever-Hall method

Unfortunately, keeping an optical cavity on resonance with respect to an input laser beam is not a simple matter. Thermal fluctuations, air currents and vibrations, amongst other factors, cause an optical cavity to vary in length and therefore alter the resonance frequency. Since the free-spectral range (the spacing of the resonator modes) is very small, it only takes tiny fluctuations in this cavity length (only tens of picometres for a high finesse cavity) to knock the cavity off resonance and therefore ruin the intra-cavity power.

It is therefore often necessary to employ an electronic feedback method to lock the cavity onto resonance. This can compensate for any length change of the cavity, or any frequency variation in the input laser. There are two main methods by which this can be achieved: the Hänsch-Couillard method[125] and the Pound-Drever-Hall method[126,127]. The former requires an intra-cavity polariser to give reflected light a frequency-dependent elliptical polarisation, while the latter involves frequency-modulating the in-coupled light and monitoring the reflected cavity light with a phase-sensitive detector. The cavity locking in this thesis utilises the latter option: the Pound-Drever-Hall (PDH) method.

The first requirement for the PDH method is to impose sidebands (usually at a separation of some tens of MHz) on the incident beam. There are two main methods for achieving this: by using an Electro-Optic modulator (EOM) to modulate the phase (and therefore the frequency) of the laser beam, or by modulating the current to that of a laser diode (which has the effect of modulating both the frequency and amplitude of the laser). Firstly (as the derivation is simpler), we shall consider the method using an EOM.

As shown in figure 5.3, a laser beam is emitted and passes through an EOM that modulates the phase of the beam. This EOM consists of a crystal whose refractive index changes when an electric field is applied across it (created by putting a parallel plate capacitor across it). When the crystal is exposed to an electric field, the optical path length through it will increase and light will take longer to pass through it. This, in turn, alters the phase of the emergent laser beam.

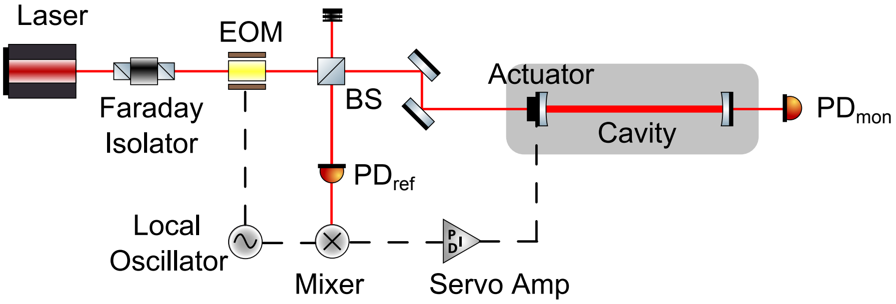

Figure 5.3: Basic layout of a Pound-Drever-Hall locked cavity.

An alternating electric field, whose frequency is set by a local oscillator, is applied to an EOM crystal. If the phase of a laser beam is modulated with a frequency that is larger than the cavity linewidth, then two sidebands are formed around the laser carrier frequency. These sidebands are used to produce the error signal which is eventually used to stabilise the cavity.

When the beam emerges from the EOM it passes into the optical cavity itself, whereupon a portion will travel back and forth many times. The light which is reflected straight from the cavity beats with light emerging from the cavity, and this signal is detected on a high-bandwidth photodiode. The mixer then multiplies this beat pattern together with the reference signal coming from the local oscillator to form an error signal. After the mixer, the signal is filtered such that only the portion that is at the modulation frequency remains. The resultant error signal is shown in figure 5.4.

Once this signal is created, it can be amplified or have its sign changed by the servo amp. It is then sent to the actuator, which is a piezo-electric crystal whose size varies according to what voltage is passed through it. In this way, there is a complete feedback loop which should keep the cavity locked onto the TEM$_{00}$ mode (the lowest order transverse mode that can circulate inside a resonator).

If, for whatever reason, the mode tries to drift up in frequency then there is a phase shift and, in turn, the error signal will send a lower voltage to the actuator. This reduces its size and drags the mode back onto resonance, and works vice versa in the opposite direction. It should be noted that this feedback stabilisation works only in the linear portion of the error signal. Moreover, the two other linear portions on each side of the

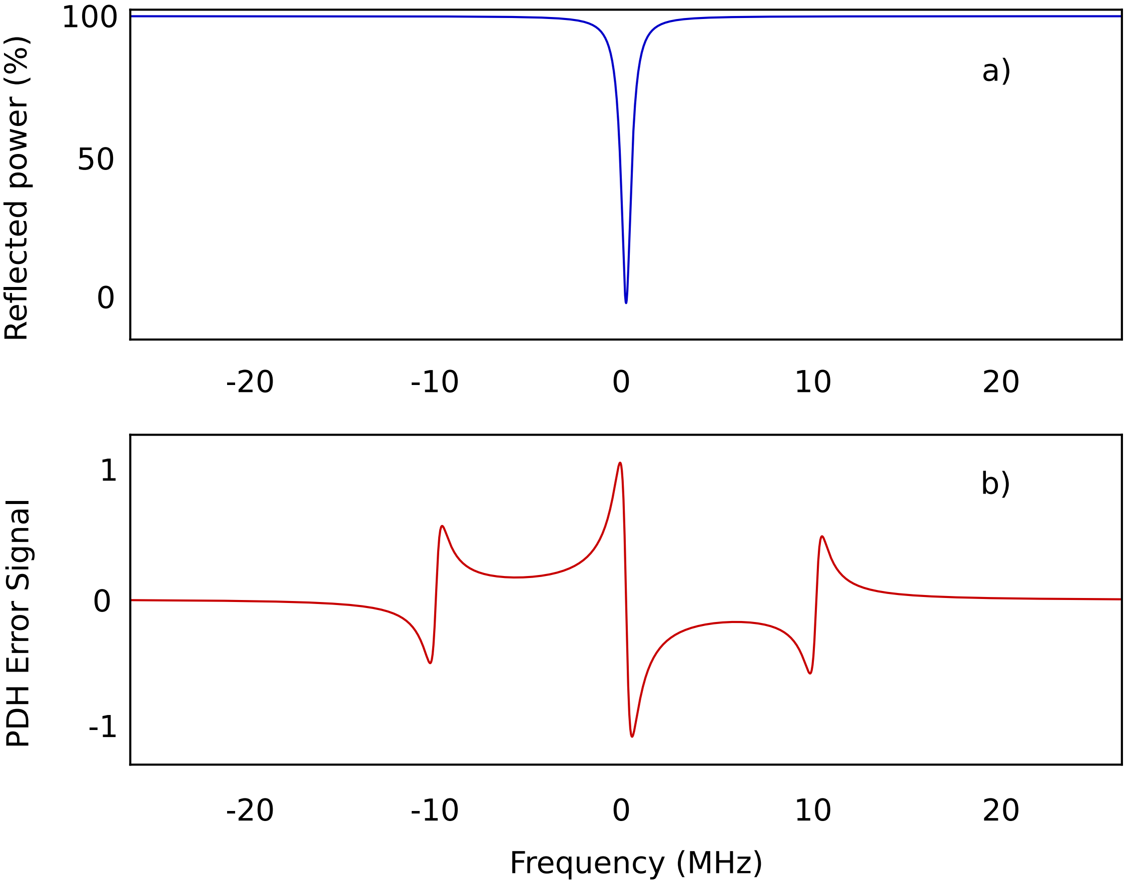

Figure 5.4: Graph a) shows a theoretical mode in reflection, while b) shows the corresponding error signal. The modulation frequency was simulated to be 10 MHz.

carrier are error signals for the two sidebands, so that it is possible to lock to these as well (if desired).

To derive the equation for the error signal, we start with a laser beam propagating in free space with an electric field of the form $E_0e^{i\omega t}$. After the beam passes through a phase modulator being driven at a modulation frequency Ω, the electric field can now be written as:

$$E_{inc} = E_0e^{i(\omega t+\beta\sin\Omega t)} \tag{5.14}$$

where β is the modulation depth. This can be rewritten in terms of Bessel functions [128–130]. The Bessel function, J_n, is a regular solution of the differential equation:

$$x^2\ddot{J}_n + x\dot{J}_n + \left(x^2 - n^2\right) J_n = 0 \tag{5.15}$$

and it satisfies the so-called generating formula

$$e^{i\beta\sin\Omega t} = \sum_{-\infty}^{\infty} e^{ni\Omega t} J_n(\beta) \tag{5.16}$$

For small values of β, the right-hand side of equation (5.14) may be approximated by simply using the terms with $n = -1, 0, 1$ in the generating formula, giving:

$$E_{inc} \approx E_0 \left[J_0(\beta) + 2iJ_1(\beta)\sin\Omega t\right] e^{i\omega t} = E_0 \left[J_0(\beta)e^{i\omega t} + J_1(\beta)e^{i(\omega+\Omega)t} - J_1(\beta)e^{i(\omega-\Omega)t}\right] \tag{5.17}$$

where equation (5.17) has been formed by taking complex exponentials. Writing the electric field in this way, one can see that there are three beams each with different frequencies: the carrier, at angular frequency ω, and two sidebands with frequencies $\omega \pm \Omega$. If each term in equation (5.17) is multiplied by the reflection coefficient, $F = \frac{\sqrt{R}(e^{i\phi}-1)}{1-Re^{i\phi}}$, at the corresponding frequency, then an equation for the reflected beam is obtained:

$$E_{ref} = E_0 \left[F(\omega)J_0(\beta)e^{i\omega t} + F(\omega+\Omega)J_1(\beta)e^{i(\omega+\Omega)t} - F(\omega-\Omega)J_1(\beta)e^{i(\omega-\Omega)t}\right] \tag{5.18}$$

To obtain an expression for the power, $P_{ref} = |E_{ref}|^2$ is used. After some algebraic manipulation, and using the fact that (for small β) $J_0(\beta) \sim 1$ and $J_1(\beta) \sim \frac{1}{2}\beta$ the following is obtained:

$$\begin{aligned} P_{ref} &= P_c\,|F(\omega)|^2 + P_s\left\{|F(\omega+\Omega)|^2 + |F(\omega-\Omega)|^2\right\} \\ &+ 2\sqrt{P_cP_s}\left\{\mathrm{Re}\left[F(\omega)F^*(\omega+\Omega) - F^*(\omega)F(\omega-\Omega)\right]\cos\Omega t\right\} \\ &+ 2\sqrt{P_cP_s}\left\{\mathrm{Im}\left[F(\omega)F^*(\omega+\Omega) - F^*(\omega)F(\omega-\Omega)\right]\sin\Omega t\right\} \\ &+ (2\Omega\ \text{terms}) \end{aligned} \tag{5.19}$$

where P_c is the power in the carrier and P_s is the power in each sideband. The mixer takes out the term that is proportional to $\sin\Omega t$ (because we want the term that oscillates at the modulation frequency Ω as this contains information about the phase, and the $\cos\Omega t$ term eventually cancels out). We end up with the following term as the error signal, which has already been plotted in figure 5.4b:

$$\epsilon = 2\sqrt{P_cP_s}\,\mathrm{Im}\left[F(\omega)F^*(\omega+\Omega) - F^*(\omega)F(\omega-\Omega)\right] \tag{5.20}$$

It should also be noted that, from equation (5.17), the power in the carrier, P_c, is:

$$P_c = J_0^2(\beta)P_0 \tag{5.21}$$

and the power P_s in each sideband is:

$$P_s = J_1^2(\beta)P_0 \tag{5.22}$$

Equation (5.22) is particularly useful as it allows us to calculate the theoretical height of the sidebands for a certain modulation depth.

An alternative to using an EOM to modulate the phase of the laser beam, is simply to modulate the current output from a diode laser. For this case, the derivation is subtly different as it is not only the frequency of the laser that is being modulated but also the intensity. In this way, equation (5.14) needs to be altered slightly as the amplitude of the electric field is no longer constant with time. Instead it varies as $1 + \alpha\cos(\Omega t)$ where Ω is the modulation frequency of the current being driven to the laser diode, and α is the effective amplitude modulation (AM) depth. We can therefore re-write this electric field emitted by the laser diode as

$$E_{inc} = E_0 \left\{1 + \alpha\cos(\Omega t)\right\} e^{i(\omega t + \beta\sin\Omega t)} \tag{5.23}$$

where β is the frequency modulation (FM) depth. Once again, re-writing this in terms of the Bessel functions we obtain a slightly more complicated expression than before:

$$E_{inc} = E_0(1 + \alpha\cos(\Omega t))\left[J_0(\beta) + 2iJ_1(\beta)\sin(\Omega t)\right] e^{i\omega t} \tag{5.24}$$

We can then express the cos and sine terms in exponentials, leaving us with:

$$E_{inc} = E_0 \left\{1 + \frac{\alpha}{2}\left(e^{i\Omega t} + e^{-i\Omega t}\right)\right\}\left[J_0(\beta) + J_1(\beta)\left(e^{i\Omega t} - e^{-i\Omega t}\right)\right] e^{i\omega t} \tag{5.25}$$

Finally, we can rearrange this into a more useful form:

$$\begin{aligned}\frac{E_{inc}}{E_0} &= J_0(\beta)e^{i\omega t} + \left\{J_1(\beta) + \frac{\alpha}{2}J_0(\beta)\right\}e^{i(\omega+\Omega)t} \\ &+ \left\{-J_1(\beta) + \frac{\alpha}{2}J_0(\beta)\right\}e^{i(\omega-\Omega)t} + \frac{\alpha}{2}J_1(\beta)\left\{e^{i(\omega+2\Omega)t} - e^{i(\omega-2\Omega)t}\right\}\end{aligned} \tag{5.26}$$

If we once again ignore the 2Ω terms we see, in a similar way to before, that we have three beams with separate frequencies: the carrier with frequency ω, and two sidebands with frequencies $\omega \pm \Omega$ (we also have further sidebands with frequencies $\omega \pm 2\Omega$ but these are usually neglected). It should also be noted that the sidebands, generally, no longer have equal amplitudes. Instead the powers in each of the sidebands are $\frac{1}{4}(\alpha+\beta)^2 P_0$ and $\frac{1}{4}(\alpha-\beta)^2 P_0$. Here, we have again used the approximation that, for small β, $J_0(\beta) \sim 1$ and $J_1(\beta) \sim \frac{1}{2}\beta$.

5.3 Optical cavity design

Designing an optical cavity, especially one that is to be used as a dipole trap, is not a trivial task. There are various factors to consider, some of which appear to clash with others. Therefore compromises usually have to be made. The main considerations to consider are listed in this section.

5.3.1 Cavity stability

The case discussed in section 3.1 is an over-simplified view of a cavity as it consists of a cavity with flat mirrors. Experimentally this is impractical to implement for stability reasons. Curved mirrors are therefore usually used. To calculate the stability criteria, we can use ABCD matrices[131,132].

The case of an optical cavity can be considered to be two mirrors, each of radius of curvature R and focal length $R/2$ which are a distance d apart. The path of a laser beam over one trip of the cavity, and reflection from a single mirror can be described as[131] (where the initial beam height and angle are r_1 and θ_1 respectively):

$$\begin{aligned}\begin{pmatrix} r_2 \\ \theta_2 \end{pmatrix} &= \begin{pmatrix} 1 & 0 \\ -\frac{1}{f} & 1 \end{pmatrix} \begin{pmatrix} 1 & d \\ 0 & 1 \end{pmatrix} \begin{pmatrix} r_1 \\ \theta_1 \end{pmatrix} \\ &= \begin{pmatrix} 1 & d \\ -\frac{1}{f} & 1 - \frac{d}{f} \end{pmatrix} \begin{pmatrix} r_1 \\ \theta_1 \end{pmatrix}\end{aligned} \tag{5.27}$$

Here, $\left(\begin{smallmatrix} 1 & 0 \\ -\frac{1}{f} & 1 \end{smallmatrix}\right)$ is the ABCD matrix[132] for a lens of focal length f (or a reflection from a cavity mirror). The matrix $\left(\begin{smallmatrix} 1 & d \\ 0 & 1 \end{smallmatrix}\right)$ displays propagation in free space over a distance d.

For cavity stability, we require r_2 to be less than r_1 and similarly θ_1 to be less than θ_2. If these conditions do not hold, then the circulating beam will progressively diverge and eventually lead to instability (and therefore mean that light leaks out of the cavity as shown later on in figure 5.5).

This can be simplified into an eigenvalue equation of the form:

$$\begin{pmatrix} r_2 \\ \theta_2 \end{pmatrix} = \lambda \begin{pmatrix} r_1 \\ \theta_1 \end{pmatrix} \tag{5.28}$$

Here, stability of the cavity is maintained when $\lambda < 1$. To solve this problem for an ABCD matrix, we have:

$$\begin{pmatrix} r_2 \\ \theta_2 \end{pmatrix} = \begin{pmatrix} A & B \\ C & D \end{pmatrix} \begin{pmatrix} r_1 \\ \theta_1 \end{pmatrix} = \lambda \begin{pmatrix} r_1 \\ \theta_1 \end{pmatrix} \tag{5.29}$$

and therefore also:

$$\begin{pmatrix} A - \lambda & B \\ C & D - \lambda \end{pmatrix} \begin{pmatrix} r_1 \\ \theta_1 \end{pmatrix} = 0 \tag{5.30}$$

This equation will only be satisfied, in a non-trivial way, for the case where the determinant is zero:

$$\det \begin{pmatrix} A - \lambda & B \\ C & D - \lambda \end{pmatrix} = 0 \tag{5.31}$$

For our individual case, we end up with the following:

$$\det \begin{pmatrix} 1-\lambda & d \\ -\frac{1}{f} & 1-\frac{d}{f}-\lambda \end{pmatrix} = \lambda^2 - 2\lambda\left(1-\frac{d}{2f}\right)+1=0 \tag{5.32}$$

For simplicity, we can re-write this equation as:

$$\lambda^2 - 2\alpha\lambda + 1 = 0 \tag{5.33}$$

where $\alpha = 1 - \frac{d}{2f}$. Re-writing equation (5.32) in this way allows us to see more simply that the two solutions are either both real or both imaginary, depending on the size of α. If $|\alpha| > 1$, then both solutions are real and can be written as:

$$\lambda = \alpha \pm \sqrt{\alpha^2 - 1} = e^{\pm\phi}, |\alpha| > 1 \tag{5.34}$$

Imaginary solutions are obtained for the case when $|\alpha| < 1$:

$$\lambda = \alpha \pm i\sqrt{1-\alpha^2} = e^{\pm i\phi}, |\alpha| < 1 \tag{5.35}$$

To ascertain whether or not the cavity is stable, we need to examine what happens when the laser beam undergoes N reflections between the cavity mirrors. This can be achieved by looking at the following simple equation:

$$\begin{pmatrix} r_N \\ \theta_N \end{pmatrix} = \lambda^N \begin{pmatrix} r_1 \\ \theta_1 \end{pmatrix} \tag{5.36}$$

For the case of real solutions, where $|\alpha| > 1$, we obtain:

$$\begin{pmatrix} r_N \\ \theta_N \end{pmatrix} = e^{\pm N\phi} \begin{pmatrix} r_1 \\ \theta_1 \end{pmatrix} \tag{5.37}$$

We can see that, for large N, this solution must diverge. In practice, what this means is that for $|1 - \frac{d}{2f}| > 1$, the cavity is unstable. Conversely, for the case where $|\alpha| < 1$ we have:

$$\begin{pmatrix} r_N \\ \theta_N \end{pmatrix} = e^{\pm iN\phi} \begin{pmatrix} r_1 \\ \theta_1 \end{pmatrix} \tag{5.38}$$

which no longer diverges as $|e^{iN\phi}| = 1$. We can therefore see that when $|1 - \frac{d}{2f}| < 1$, the cavity can be considered stable. Re-writing equation (5.35) in terms of the cavity length, d, and the focal lengths of the cavity mirrors, f, we get the following:

$$\lambda = \left(1 - \frac{d}{2f}\right) \pm i\sqrt{1 - \left(1 - \frac{d}{2f}\right)^2} \tag{5.39}$$

The value of λ must remain imaginary for cavity stability and so, for mirrors of equal curvature, we end up with the stability condition:

$$1 > \frac{d}{4f} \text{ or } 0 < d < 4f \tag{5.40}$$

which, once we substitute in $f = \frac{R}{2}$, is equivalent to:

$$0 < d < 2R \tag{5.41}$$

The case for a cavity with mirrors of unequal curvature is more complex as we now have to consider the case where the laser beam undergoes a full round-trip of the cavity:

$$\begin{aligned} \begin{pmatrix} A & B \\ C & D \end{pmatrix} &= \begin{pmatrix} 1 & 0 \\ -\frac{1}{f2} & 1 \end{pmatrix} \begin{pmatrix} 1 & d \\ 0 & 1 \end{pmatrix} \begin{pmatrix} 1 & 0 \\ -\frac{1}{f_1} & 1 \end{pmatrix} \begin{pmatrix} 1 & d \\ 0 & 1 \end{pmatrix} \\ &= \begin{pmatrix} 1 & d \\ -\frac{1}{f2} & 1 - \frac{d}{f2} \end{pmatrix} \begin{pmatrix} 1 & d \\ -\frac{1}{f_1} & 1 - \frac{d}{f1} \end{pmatrix} \end{aligned} \tag{5.42}$$

To find the stability criteria for this case, we need to use Sylvester's theorem[133]. This theorem is used for when a beam undergoes a periodic sequence through identical optics, and this is essentially what a optical cavity does. Light bounces back and forth in a repetitive manner. The theorem asserts that:

$$\begin{pmatrix} A & B \\ C & D \end{pmatrix}^n = \frac{1}{\sin\Theta} \begin{pmatrix} A\sin n\Theta - \sin(n-1)\Theta & B\sin n\Theta \\ C\sin n\Theta & D\sin n\Theta - \sin(n-1)\Theta \end{pmatrix} \tag{5.43}$$

where[134];

$$\cos\Theta = \frac{1}{2}(A + D) = 2\left(1 - \frac{d}{2f_1}\right)\left(1 - \frac{d}{2f_2}\right) - 1 \tag{5.44}$$

Periodic sequences are stable when the trace of the matrix $\left(\begin{smallmatrix} A & B \\ C & D \end{smallmatrix}\right)$ in equation (5.43) obeys the inequality:

$$-1 \leq \frac{1}{2}(A+D) \leq 1 \tag{5.45}$$

After some algebraic manipulation, we therefore end up with:

$$0 \leq \left(1 - \frac{d}{2f_1}\right)\left(1 - \frac{d}{2f_2}\right) \leq 1 \tag{5.46}$$

Going back to the case of an optical cavity (instead of that of two lens), we simply replace the focal lengths by the radii $R_1/2$ and $R_2/2$. This leads to:

$$0 \leq \left(1 - \frac{d}{R_1}\right)\left(1 - \frac{d}{R_2}\right) \leq 1 \tag{5.47}$$

where d is the spacing between cavity mirrors. To display the stability of a cavity pictorially, we introduce parameters g_1 and g_2. These are equal to $1 - \frac{d}{R_1}$ and $1 - \frac{d}{R_2}$ respectively. The stability diagram for optical cavities is given in figure 5.5 below:

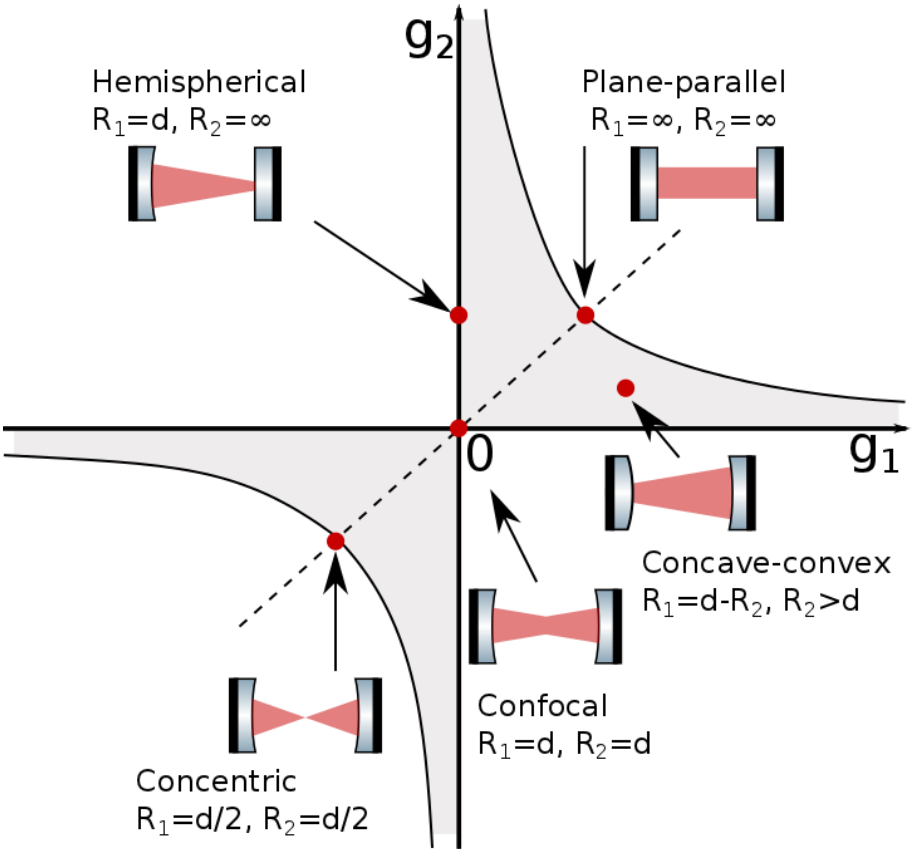

Figure 5.5: Stability diagram for an optical cavity. The shaded area represents the area in which a cavity is stable. Different types of stable cavities are displayed on the figure.

Particular different types of cavity are shown in figure 5.5. These include hemispherical, concentric, confocal, concave-convex and plane-parallel cavities. For the purposes of atomic trapping usually a cavity somewhere between a concentric and confocal one would be used. This creates a focus at the centre of the cavity-therefore creating higher intensities and thus well depths at the centre. Moreover, intensities on the mirrors will be lower which will lesson any mirror heating effects (which we will discuss later in this chapter).

While designing a cavity, verifying the stability is a crucial first step. In practice, if the stability criterion is not obeyed then light will leak out of the cavity on each round trip and therefore any possible build-up inside the cavity will be ruined.

5.3.2 Waist size

Deciding on a suitable waist size circulating within the cavity can often be a bit of a trade-off with regards to trapping atoms. On one hand, the waist should ideally be as large as the initial MOT to trap the largest possible amount of atoms within the cooled cloud. On the other hand, higher intensities are also desirable so that the potential well depths are deep enough for trapping. Thus, the parameters of the cavity depend on the experimental needs.

To calculate a formula for the waist inside an optical cavity, we first have to understand a little more about the properties of the laser beams that circulate inside them. The fundamental mode that circulates inside a cavity (the TEM$_{00}$ mode) has a Gaussian profile. Gaussian beams have intensity distributions of the form:

$$I = I_0 e^{-2r^2/w^2} \tag{5.48}$$

where I_0 is the maximum intensity and r is the distance away from the central axis of propagation. At $r = w$, the beam's intensity falls to I_0/e^2. Here, we can introduce another two beam parameters: the radius of curvature of the beam $R(z)$, and a quantity called the complex beam parameter $q(z)$. These are related to each other by:

$$\frac{1}{q} = \frac{1}{R} - i\frac{\lambda}{\pi w^2} \tag{5.49}$$

At the minimum beam waist, the beam-front is plane and so the radius of curvature $R(z)$ is equal to zero. We can therefore re-write equation (5.49) as:

$$q_0 = i\frac{\pi w_0^2}{\lambda} \tag{5.50}$$

and at a distance, z, away from the waist the complex beam parameter can be written as:

$$q = q_0 + z = i\frac{\pi w_0^2}{\lambda} + z \tag{5.51}$$

We can now combine equations (5.49) and (5.51), and after equating the real and imaginary parts of these equations we end up with:

$$w(z) = w_0\sqrt{1 + \left(\frac{\lambda z}{\pi w_0^2}\right)^2} \tag{5.52}$$

and

$$R(z) = z\left[1 + \left(\frac{\pi w_0^2}{\lambda z}\right)^2\right] \tag{5.53}$$

We can now state the condition on each cavity mirror as:

$$R_i(z) = z_i\left[1 + \left(\frac{\pi w_0^2}{\lambda z_i}\right)^2\right] = z_i + \frac{(z_R)^2}{z_i} \tag{5.54}$$

where $z_R = \frac{\pi w_0^2}{\lambda}$ is known as the Rayleigh range, which is the distance over which the mode waist increases by a factor of $\sqrt{2}$ from the minimum waist, w_0. Using equation (5.54) with the fact that $z_2 - z_1 = d$, we end up with (after some algebraic manipulation and taking the case of a symmetric cavity with $R_1 = R_2$) the following:

$$w_0^2 = \frac{\lambda}{2\pi}\sqrt{d(2R - d)} \tag{5.55}$$

We can also, therefore, obtain the Rayleigh range to be

$$z_R = \frac{1}{2}\sqrt{d(2R - d)} \tag{5.56}$$

In this way, equation (5.55) allows us to design a cavity with a suitable waist for particular experiments.

Another point to consider is how to mode-match into the cavity. The idea of mode-matching (as shown in figure 5.6) is to maximise coupling between a beam propagating in free space to a mode inside an optical cavity. This is generally achieved by using a lens pair to match the shape of the beam that circulates stably within the cavity. As can be seen in the figure, two lenses are used to identically match beam sizes w_0 and w_m at the focus of the cavity and on the mirrors respectively.

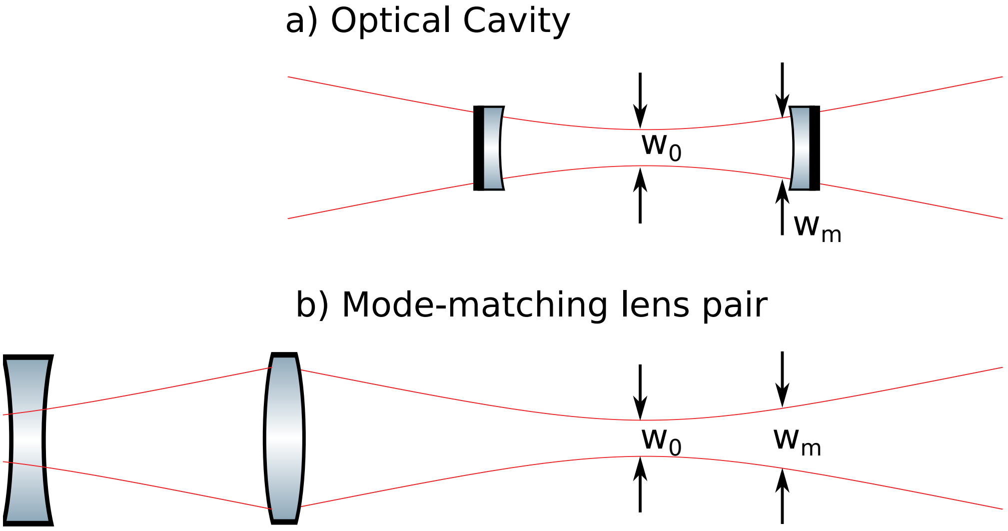

Figure 5.6: Diagram displaying mode-matching. Here, two lenses are used to identically match the shape of a stable beam circulating within the cavity.

In order to select a suitable lens pair for mode-matching, the following formulae can be used to predict the size and position of the waist of the beam[132]:

$$d_1 = f \pm \frac{w_1}{w_2}\sqrt{f^2 - \left(\frac{\pi w_1 w_2}{\lambda}\right)^2} \tag{5.57}$$

$$d_2 = f \pm \frac{w_2}{w_1}\sqrt{f^2 - \left(\frac{\pi w_1 w_2}{\lambda}\right)^2} \tag{5.58}$$

Here (as depicted in figure 5.7), the waist w_1 is formed by the first lens at a distance d_1 away from the second lens. This lens then, in turn, forms a waist w_2 a distance d_2 away from it. The focal length of the second lens is labelled f.

Of course, if the radius of curvature of the cavity mirrors is small then it can have a substantial effect on the position of the focus of the beam. Setting up mode-matching in practice can simply consist of setting up a camera to monitor the size of the focus at the centre of the cavity as a lens position is adjusted.

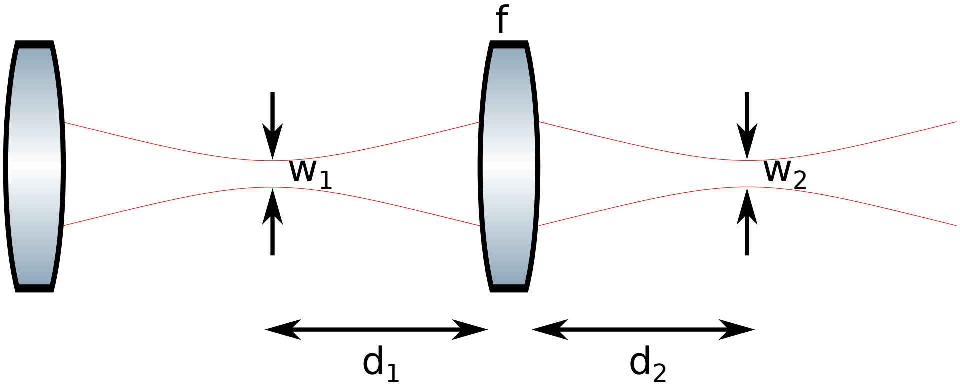

Figure 5.7: Graphic displaying notation for mode-matching equations 5.57 and 5.58.

5.3.3 Choosing mirror properties

Selection of the reflectivity and transmission properties of an optical cavity is not entirely straightforward. There are several concerns to be met including what you would like the finesse and linewidth to be and getting good impedance matching into the cavity.

As we have already seen in equation (5.7), the finesse is simply equal to the free-spectral range divided by the linewidth. As such, for a specified cavity length, the linewidth is inversely proportional to the finesse. The linewidth may not seem like an important factor to consider but the smaller it becomes, the more challenging is the implementation of a Pound-Drever-Hall lock. Indeed, for the purposes of achieving a high build-up intensity, there is little point in having a cavity of lower linewidth than the input laser as only the parts of the input beam resonant with the cavity will be coupled into the cavity.

While choosing what mirror reflectivities to use, the key consideration is what amplification of power is required from the cavity. To do this we can look back to equation (5.13) where we derived the expression from the build-up factor, G, inside a cavity. Here we can see that the build-up is strongly related to the cavity finesse. This makes sense as when the amount of light leaking out of the cavity on each round-trip decreases, the circulating intensity inside the cavity must increase.

There is another factor to bear in mind, however, as selecting two identical mirrors in a cavity will not lead to the maximum possible build-up. We have to consider impedance-matching into the cavity. We can see the effect of this by differentiating equation (5.13) with respect to T_1 to obtain:

$$G' = \frac{4\epsilon(1-l_1-l_2)(l_1+l_2-T_1+T_2)}{(l_1+l_2+T_1+T_2)^3} \tag{5.59}$$

This shows that a maximum is obtained by setting $T_1 = T_2 + l_1 + l_2$, which is verified by a negative second derivative. This relationship is known as the 'impedance-matching condition'. This condition only needs to be met when the losses per mirror l are significant when compared to the transmissions, T. If $T >> l$, then two identical mirrors are fine for an optical cavity as the impedance matching condition will be satisfied.

Another important factor to consider (especially if there is a very high circulating intensity inside the cavity) is that of mirror heating. High circulating intensities can lead to strong perturbations to the cavity. This occurs because even small absorption in the mirror coatings can lead to significant heating for high intra-cavity intensities. Previous work[135,136] has characterised the change in mirror radius of curvature as the intensity on the cavity mirrors increases. In Ref.[135] a radius of curvature change of 105 μm/(MW/cm^2) was measured for a 6,300 finesse cavity in air, while Ref.[136] measured between 47 and 60 μm/(MW/cm^2) for a 78,100 finesse cavity at a pressure of 1.3×10^{-5} mbar. LIGO experiments have also put great effort into minimising thermal instability caused by cavity mirror heating[137].

As will be discussed in much greater detail later on, in Chapter 6, the work in this thesis presents results that show much higher mirror flexing than previously measured. This is partially due to the fact that the pressure under which our experiment is performed is lower than in Refs.[135,136], but also because our cavity is of a lower finesse and therefore has mirrors that absorb/scatter more light. We measure[98] a value of 116±10 mm/(MW/cm^2), and observe unlocking of the cavity under long periods of high circulating intensity.

Chapter 6

Far-off resonance build-up cavity: metastable argon trapping

An alternative to simply focussing a high power laser to create high trapping intensities is to utilise the power enhancement properties of an optical cavity[138–140]. Here, the intra-cavity power can be orders of magnitude higher than that input into the cavity. While very high intensities can be achieved in a build-up cavity, such a trap is more complicated because the cavity must be actively controlled so that it is always in resonance with the laser. This requires a stable laser and cavity, and a feedback scheme to maintain high intra-cavity intensity with low noise characteristics. For a fixed input intensity, a higher finesse cavity which has a narrower linewidth can be used to produce a higher intra-cavity intensity, and therefore a deeper trap. However, the narrower linewidth can be more difficult to lock stably in a noisy environment. In addition, switching and modulating a cavity trap is difficult since a constant optical intensity is required to keep the cavity locked on resonance. Higher finesse cavities also have a longer decay time for the circulating light. This therefore limits how quickly the intra-cavity intensity can be modulated.

In this chapter we describe a deep optical trap using the high circulating intensity in a Fabry-Perot build up cavity. To minimise intensity noise we use a medium finesse cavity (∼2000) and a high input power to realise circulating power of up to 1 kW, with trap depths up to 11 mK for metastable argon atoms. Additionally, we use a weak beam to lock the cavity and a strong beam, that can be varied independently, to produce the high circulating intensity for the trap. This enables us to rapidly modulate the trap depth up to a bandwidth of 5 MHz.

6.1 Construction of a test cavity

6.1.1 Cavity spacer and mirrors

Before a final design of the cavity that would be used for trapping was settled upon, it was decided to first construct a test cavity. In this way, complexities of constructing and locking of a high finesse cavity could be determined. The cavity spacer was made out of Invar (a metal with very low thermal expansion) consisting of four rods (of 1/2 inch diameter) bolted to two 5×5 cm square plates with holes drilled for light to enter and exit the cavity. The cavity length itself is 8.2 cm and designed to allow optical access for all MOT beams.

Highly reflective off-the-shelf mirrors were ordered from Layertec (part no. 109556) and were quoted as having reflectivity >99.992% and transmission ∼0.001% at 1064 nm, with radius of curvature 20 cm. While these numbers were vague, the mirrors made an ideal candidate for the construction of a high finesse cavity. Moreover, these mirrors were cost-effective as they were off-the-shelf and so an expensive custom mirror coating run was not required.

6.1.2 Construction of a grating-stabilised diode laser

A custom grating-stabilised diode laser was initially built for use with the optical cavity. Diode lasers are often invaluable in optical experiments as they can be made relatively cheaply and produce light of narrow bandwidth and variable wavelengths. Building such a laser has also become increasingly straightforward in recent years.

The design that was followed is a now well-established one[141]. As light emitted from a laser diode is strongly divergent, a lens is placed close after the diode (in our case a 1064 nm Thor Labs diode-product no. M9-A64-0200) for collimation purposes. More importantly, a standalone laser diode has a large linewidth (>50 MHz) and to reduce this the light is directed onto a diffraction grating. The first diffraction order is reflected back into the laser diode itself and serves to frequency stabilise the laser and reduces the linewidth to <1 MHz[141–143]. In this way, the grating forms an external resonator with the diode's rear facet. By varying the length of this external cavity (by using a piezo-electric spacer) the emissions frequency can be varied up to a maximum of half the free spectral range of the external cavity.

To prevent thermal fluctuations changing the length of the cavity, the base-plate is mounted on a Peltier element. Inside the base-plate is an "AD590" whose output is fed into a temperature controller. In this way, fluctuations in room temperature can be accounted for by heating or cooling from the Peltier. Moreover, in this way the laser diode can be temperature tuned (i.e. varying the temperature to alter the wavelength outputted). The usual amount by which the wavelength is varied is 0.3 nm/K, and can occur over tens of nanometres.

6.1.3 Pound-Drever-Hall box

To produce an error signal a custom-made Pound-Drever-Hall (PDH) box was designed (by Dr. Peter Douglas), and constructed by the department's electronics technician Rafid Jawad: the electronic circuit is described in Appendix B. Such a circuit had to fulfil several requirements to successfully produce an error signal. Firstly, it had to produce a sinusoidal signal at a frequency of tens of MHz (in order to separate it from the main mode). This was necessary to produce sidebands on either side of the cavity resonance. Secondly, it had to contain a phase sensitive detector which would be used to demodulate the reflected cavity signal at the modulation frequency and obtain an error signal from it (as described in section 5.2).

In practice, varying lengths of cable between the reflected beam photodiode and input to the PDH box had to be used (as a phase shifter) in order to make sure that the modulation frequency and reflected mode had the correct phase relationship. Improper phase shifts lead to some peculiar looking error signals, and to unstable locking.

6.1.4 Alignment, results and characterisation of test cavity

The first challenge in setting up the cavity was to attach the mirrors to the cavity spacer and to align the mirrors correctly. Firstly, one of the cavity mirrors was glued (using Torr seal, which is a vacuum-compatible epoxy) to a piezo-electric transducer which, in turn, was glued to the cavity mount. The other cavity mirror was attached to an x-y-z translation stage and its position and angle systematically changed until coupling into the TEM_{00} mode was optimised. Throughout this process the cavity was scanned in frequency and the modes emergent from the cavity were split and placed on both a CCD camera and a photodiode. In this way, alignment into the cavity could be easily optimised until the vast majority of the light was coupled into the TEM_{00} as shown in figure 6.1. Once the cavity was aligned correctly, the remaining cavity mirror was glued onto the mount. While the glue was setting the alignment was monitored and adjusted slightly to compensate for slight movement of the cavity mirror.

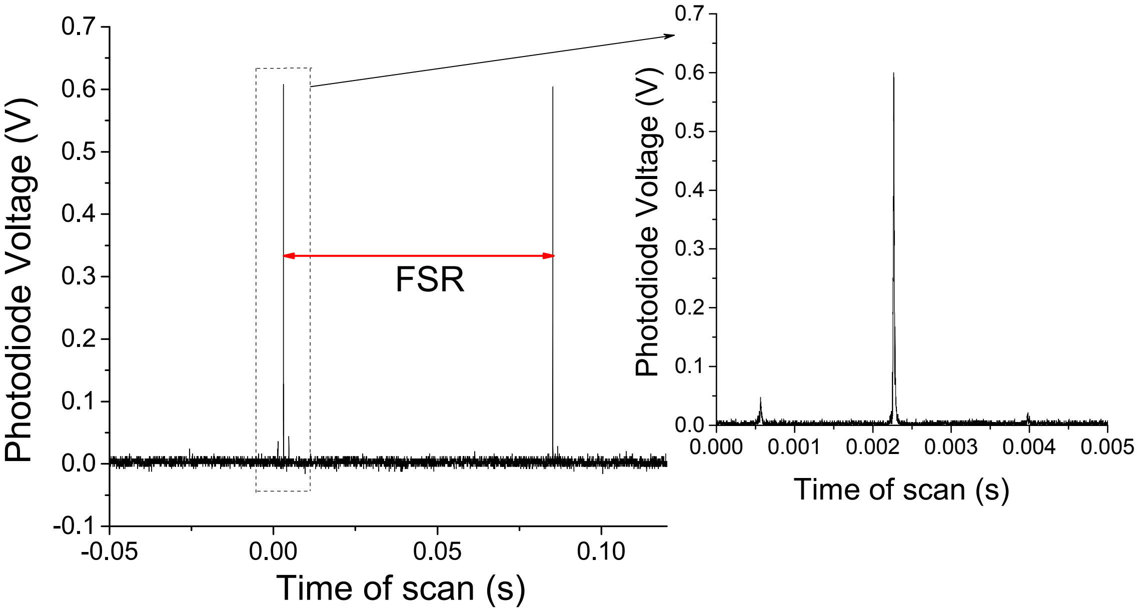

Figure 6.1: Figures showing the cavity being scanned in frequency. a) shows the free spectral range of the cavity, while b) shows a zoomed-in scan of the mode and two sidebands.

After the cavity was successfully aligned, it was necessary to modulate the input beam's frequency so that we could impose sidebands on a resonant mode as described in section 5.2. To do this, we simply installed a "bias t" (from Thor labs) inside the diode laser so that we could directly modulate the current that the diode is being driven by. In this way the frequency could be directly modulated, the result of which is shown in figure 6.1 b). Here, one can see the sidebands superimposed on either side of the TEM_{00} mode. This is necessary to generate an error signal for locking of the cavity.

The next step was the characterise the cavity, and to try and perform PDH locking on it (described more fully in section 5.2). The sidebands shown in figure 6.1 b) were used to calibrate the piezo voltage to frequency and allowed us to calculate a value of the free-spectral range (FSR) as 1.7±0.2 GHz. This was slightly lower than the expected value of 1.83 GHz (calculated from the equation FSR=c/2L) and the difference attributed to the piezo displaying hysteresis effects and not scanning linearly.

This effect was investigated, with the cavity purposely misaligned (to induce higher order modes) and the different transmission modes recorded. As the modes are equidistant from each other, they can be used as a frequency reference and so be used to show piezo

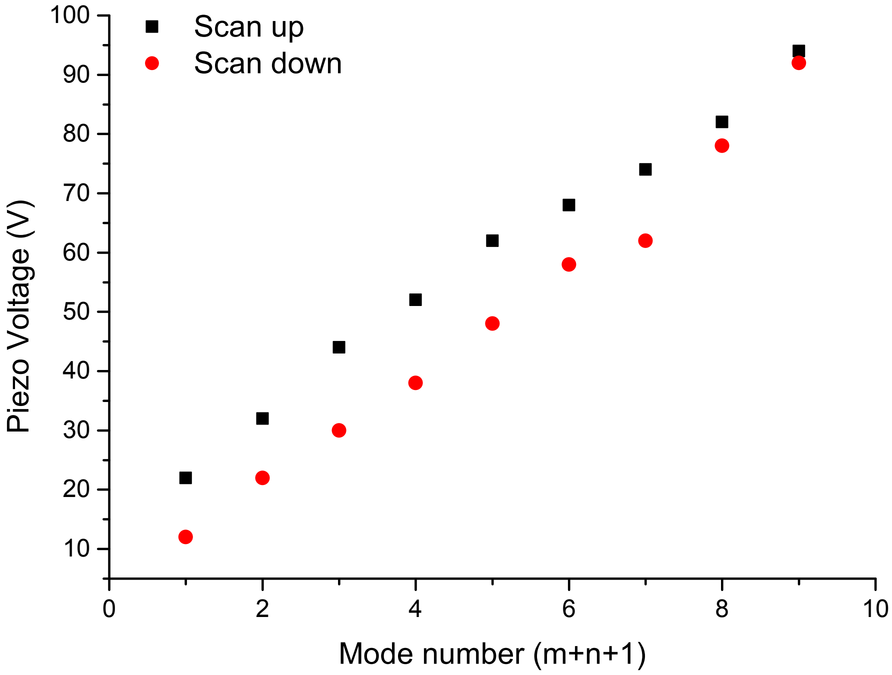

Figure 6.2: Graph showing the effect of piezo hysteresis. The cavity was purposely misaligned to display a variety of modes and then scanned up in frequency. While the cavity was scanned down in frequency the same modes are shown at slightly different piezo voltages to before.

hysteresis. The frequency of the modes is given by[144]

$$\nu_{qmn} = q\Delta_{\mathrm{FSR}} + (m+n+1)\Delta_{\mathrm{Gouy}} \tag{6.1}$$

where Δ_{FSR} is the free spectral range, Δ_{Gouy} is the Guoy phase change (i.e. distance between consecutive TEM modes), ν is the frequency of the modes, m and n are the labels of the TEM$_{mn}$ modes. The result of this measurement is displayed in figure 6.2, where hysteresis effects are clearly shown. This, however, is a fairly common effect for piezo electric transducers[145] and can be overcome by scanning the laser frequency instead of the cavity's (we did not scan our laser's frequency in order to prevent the diode from mode-jumping over a comparatively large scan). By using the data presented in figure 6.2 we can compensate for the hysteresis effects and obtain a value of the free-spectral range to be 1.8±0.1 GHz, consistent with the expected value.

Calculating the finesse of the cavity was more complicated than originally thought. The most commonly used way of calculating finesse would be to simply take a measurement of the linewidth of the cavity resonance. This would then be used to calculate the finesse as the free-spectral range divided by the linewidth. This measurement was attempted, however, in a noisy environment (again due to vibrations from vacuum pumps) and any slow scans (tens of Hz) across a mode led to a very noisy resonance peak so that it was impossible to directly calculate the linewidth of the TEM_{00} mode. Conversely, any fast scans (>100 Hz) led to the mode being broadened due to light taking time to leak out of the cavity.

However, this slow decay of light could actually be used to directly calculate the finesse by the following formula[146,147]:

$$\tau = \frac{Fl}{\pi c} \tag{6.2}$$

where τ is the cavity decay time, F is the finesse and l is the cavity length. Figure 6.3 shows an example of such a ring-down measurement. Here the cavity piezo is scanned quickly (at 300 Hz) and the light that enters the cavity can be seen to decay slowly out. From this, we calculate the decay time to be 13.7±0.5 μs, which gives a finesse of 157,000±6,000. The time taken for the piezo to scan over the mode completely is less than 100 ns, and so does not affect this measurement. The ring-down time was also verified by using an AOM to rapidly switch off the beam that is coupled into the cavity. From the free spectral range of 1.83 GHz, this measurement also leads to the value of the cavity linewidth being only 11.7±0.4 kHz.

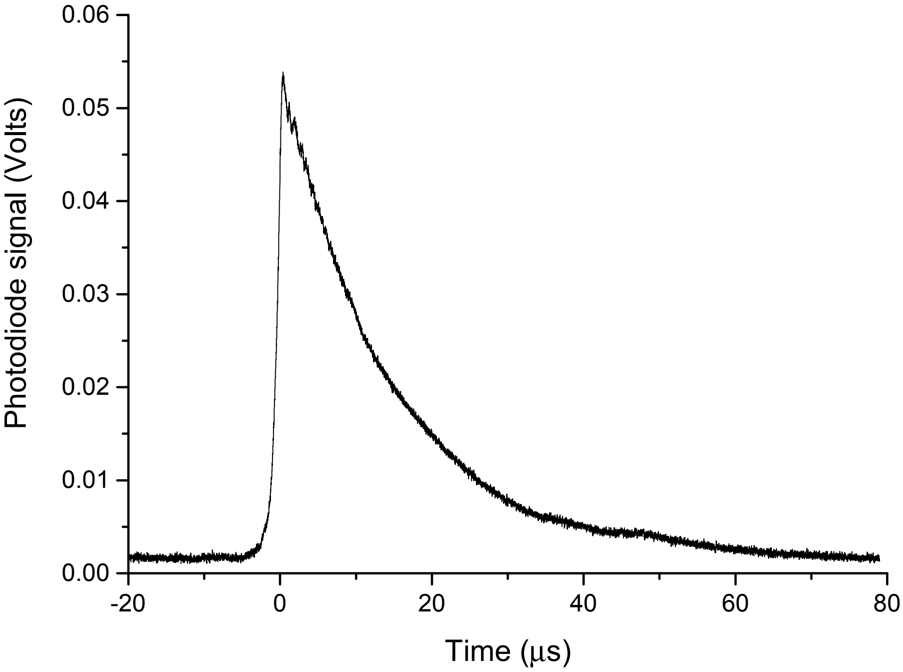

Figure 6.3: Mode of the cavity resonance, which display slow ring-down effects. The cavity decay time was determined to be 13.7±0.5 μs, leading to a finesse of 157,000±6,000.

As can be seen in figure 6.3, there are some ringing effects on the cavity mode. These ringing effects are caused by beating between the laser frequency and cavity mode frequency when either is swept in time. This phenomenon has been observed and studied by various groups[148–152], and by Poirson et al. in their 1997 paper[146]. Here, they modelled the process and used the results to accurately calculate the finesse of the cavity from the following formula:

$$\frac{\pi c}{l}\Delta t = \frac{F}{2}\left(\frac{I_1}{I_2} + 2 - e\right) \tag{6.3}$$

where I_1 and I_2 are the intensities of the first two maxima and Δt is the time difference between them. For the cavity shown in figure 6.3, these ringing effects can be more easily seen with a slower scan (as shown in figure 6.4 where the cavity is scanned at 30 Hz). As can be seen, the lifetime of the light circulating within the cavity is the same as before but the modulations on the cavity mode are more pronounced. While equation 6.3 could have been used to calculate the cavity finesse, in practice this slower scan meant that vibrations affected the cavity mode more and it was therefore difficult to get an accurate value for the finesse. Due to this, only the ring-down time was used.

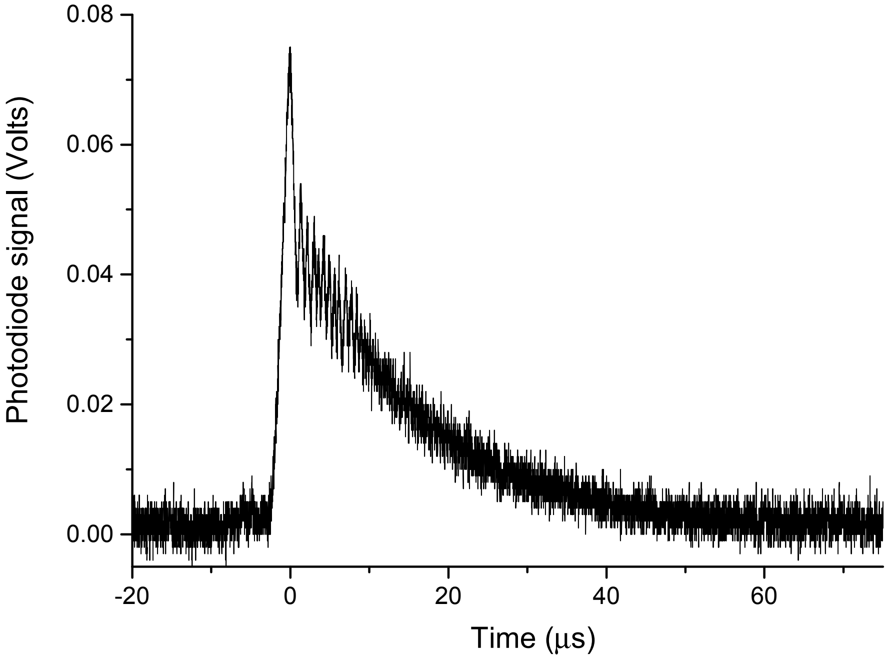

Figure 6.4: Cavity mode displaying ringing effects caused by beating between the laser frequency and the cavity mode frequency.

The calculated value of the finesse of 157,000±6,000 (from the ring-down time) was much larger than expected and the resultant narrow linewidth made the cavity difficult to lock. The narrow linewidth meant that only small vibrational disturbances led to the cavity becoming unlocked. The home-made diode laser's frequency was also influenced adversely by vibrations. Moreover, only 5% of the laser light was able to be coupled into the cavity due to poor impedance matching. Impedance matching into the cavity is optimised when $T_1 = T_2 + l_1 + l_2$ (as derived in section 5.3.3), meaning that the poor coupling into the cavity is presumably due to the transmittitivies of the mirrors being comparable in magnitude to the losses.

The combination of these factors meant that it was not possible to stably lock the cavity for more than a couple of seconds. These findings allowed us make some important modifications to the final design of the trapping cavity.

6.2 Construction and characterisation of the trapping cavity

6.2.1 Design of cavity

Due to the difficulties in locking the test cavity, it was decided to construct a cavity with a much lower finesse. A custom mirror coating was performed by Layertec, and a mirror reflectivity of 99.979% at 1064 nm was requested (which would lead to a finesse of ∼15,000). Moreover the transmittivites were requested to be close to ∼200 ppm, and losses of the order of 10 ppm. In this way, the impedance matching into the cavity should be efficient while only one mirror coating run is required and therefore the cost is kept down.

The desired waist at the centre of the cavity was $\sim 100\ \mu$m, as this would allow the majority of the MOT cloud to be trapped while still being small enough to allow for deep well depths. In this way, a mirror radius of curvature of 5 cm was settled on which leads to a waist of $\sim 80\ \mu$m at the focus. The length of the cavity spacer is again 8.2 cm (for optical access of all MOT beams), but this time the spacer was made out of a single piece of fused silica manufactured by Starna Scientific (shown in figure 6.5). Fused silica was used for its low coefficient of thermal expansion and the design again consisted of two 5x5 cm plates attached by four rods of diameter 1 cm. Such an open design allows for extensive optical access for all MOT cooling beams, and other beams as required. The mirrors themselves had a diameter of 12.7 mm and thickness of 3.0 mm.

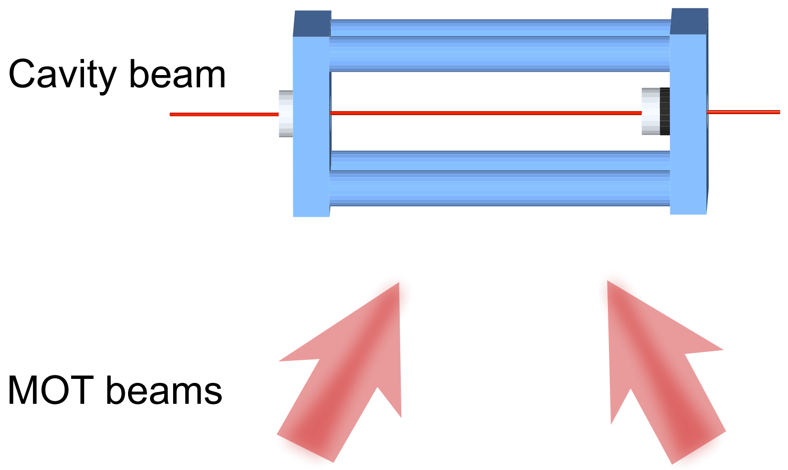

Figure 6.5: Graphic depicting the design of the fused silica cavity spacer. Particular attention was paid to allowing a design that was both stable and allowed plenty of optical access for the various MOT cooling beams.

To increase the stability of the beam coupled into the cavity, a diode-pumped solid state laser was purchased from Elforlight (product no. I4-700). Although this laser sacrificed the ability to modulate and tune the frequency, its output was extremely stable and has output powers up to 700 mW. While (with the build-up of the cavity which will be characterised in section 6.5.5) this power would be sufficient to trap metastable argon atoms, it would not be enough to trap argon in its ground state. Because of this, a fibre amplifier was purchased from Nufern (product no. 30W-SUB-1174-29) that amplified an input of between 50-200 mW up to powers of 30 W (in practice we measured up to 40 W).

The fibres within this amplifier were doped with Ytterbium ions which are excited by a pump laser (the DPSS laser in our case) and these then decay by stimulated emission. In this way, amplification of the pump beam can be achieved and high powers produced.

6.2.2 Characterisation of cavity

Characterisation of a cavity of lower finesse than that of the test cavity proved to be far simpler. Light took far less time to leak out of the cavity and because of this it was easier to obtain a good profile of the TEM_{00} resonance with a fast scan (so that vibrations do not affect the mode). The cavity mode, along with the associated error signal (produced by the PDH method) and reflected mode are all shown in figure 6.6.

The data in this figure was taken by scanning the cavity piezo at 100 Hz and noting the error signal produced by the PDH box, as well as the photodiode signals of both the transmitted and reflected cavity modes (where the sidebands can be seen). As the frequency separation of the sidebands from cavity resonance is set by the PDH box (in our case at 33 MHz), the sidebands can be used as a frequency reference and therefore allow us to calculate both the cavity linewidth and finesse.

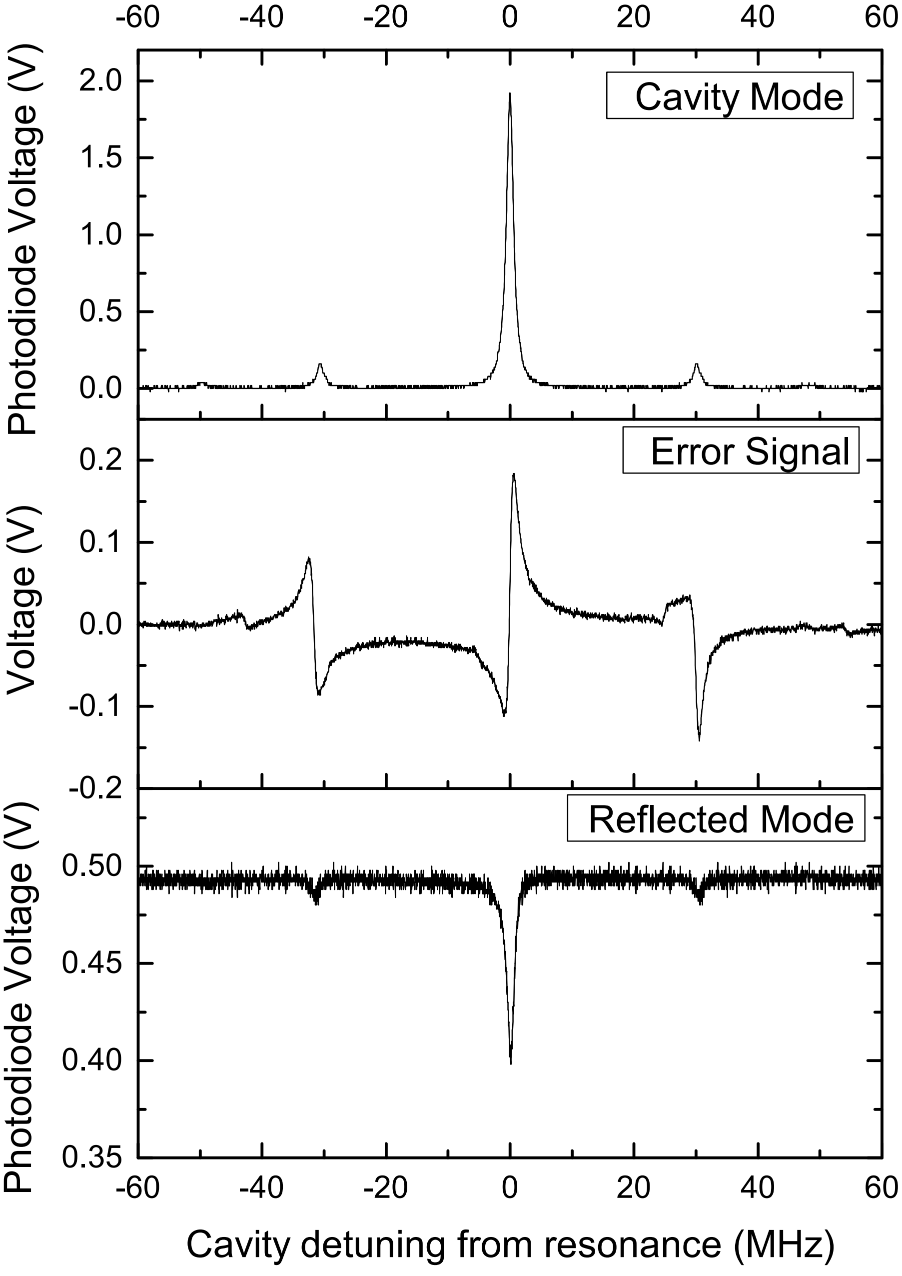

Figure 6.6: Here, the cavity was scanned in frequency at 100 Hz. The cavity mode itself is shown along with the error signal produced by the PDH box and the reflected mode. The sidebands of the TEM_{00} mode can also be seen, and are at approximately 33 MHz away from the main mode. These are used as a frequency calibration to determine the cavity's linewidth.

In doing this we note a cavity linewidth of 910±50 kHz, and a finesse of 2050±100. From the equation $F = \frac{\pi\sqrt{R}}{1-R}$, we obtain a value of the mirror reflectivity, R, to be $\sim$0.9985 (or 99.85%). This value is far less than we initially specified, and would lead to a lower cavity build-up and trap depths. Layertec themselves stated that they expected the mirrors to have a reflectivity of 99.94% which would lead to a finesse of ∼5000, but we still measured considerably less than this.

Despite this, we still expected the cavity to have sufficiently deep well depths for trapping of both metastable as well as ground state argon. For molecules, that would be comparatively "hot", the well depths would probably be too shallow. In the future, for example for sympathetic cooling experiments, a higher finesse cavity would be required to produce a deeper trap.

6.3 Experimental layout for trapping metastable argon

6.3.1 Cavity mount

One of the first challenges was to design a stable mount for the cavity to either rest on, or be attached to. Such a mount would ideally be able to have its position readily adjusted so as to perfect the overlap of the centre of the cavity with the MOT cloud position. An octagonal structure (shown in figure 6.7 with an outer radius of 9 cm was designed to fit within the inner lip (diameter ∼10 cm) of a DN100CF sized window at the bottom of the science chamber. M6 screw holes were positioned such that the mount could be raised from the window itself and held horizontally in place against the lip of the window. The screw positions could be varied continuously to allow, as a first approximation, the centre of the cavity to be placed roughly where the MOT cloud would be.

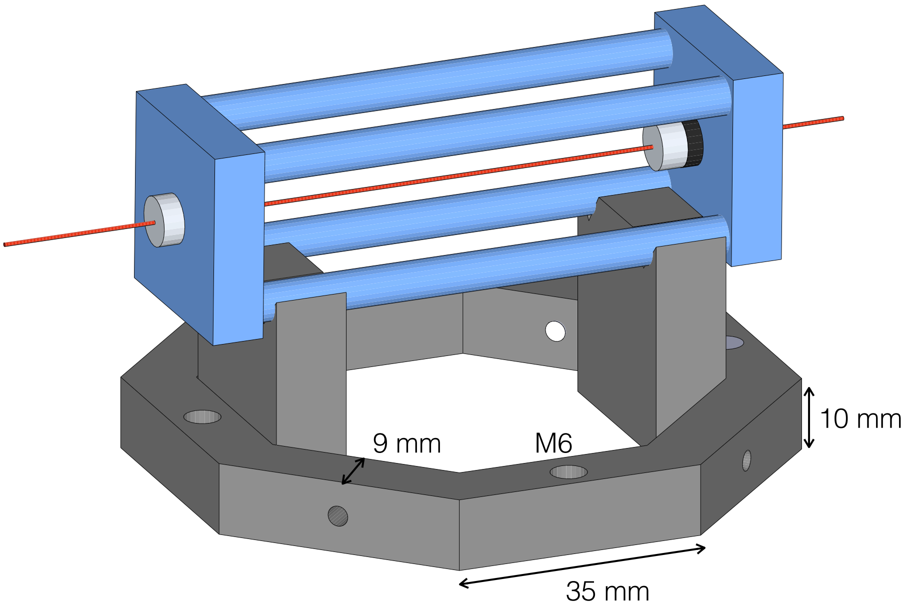

Figure 6.7: 3D model of the cavity mount placed inside the science chamber.

A “V mount” was bolted (using M6 bolts) on top of the octagonal structure, and was used to rest the cavity on top of it. It was not required to epoxy the cavity to the “V mount”, but care had to be taken when either pumping down or venting the vacuum system. If done too quickly then gas flows would subtly alter the position of the cavity and ruin the alignment. A photo of the cavity mounted within the science chamber is placed in Appendix A.

6.3.2 Optical layout

The light for the cavity trap is provided by a diode-pumped solid state (DPSS) laser (Elforlight I4-700) operating at a wavelength of 1064 nm. This produces two beams: a weak beam (100mW) that is used to lock the cavity and a stronger beam (created by a fibre amplifier-producing powers up to 30W) which creates the intra-cavity trap. The Pound-Drever-Hall (PDH) feedback method[126,127] was used to keep the cavity locked to the TEM_{00} mode. To do this, the weak beam passes through an EOM to provide the sidebands for PDH locking. The modulation frequency used was 30 MHz. The weak beam then passes through a high extinction ratio (100,000:1) polarising beam splitter (PBS) so it is orthogonally polarised to the strong beam. It is then mode-matched into the cavity using a single focusing lens.

The remainder of the DPSS beam is used to produce the strong beam, which creates the trap. To modulate the intensity of this beam, it is passed through two acousto-optic modulators (AOMs). The first AOM deflects the beam and shifts the frequency down by 80 MHz before it is coupled into a fibre amplifier (Nufern Nu-Amp) producing an output up to 30 W. The amplified beam is then shifted back up in frequency by 80 MHz before it passes through a half-wave plate and PBS. It is then mode-matched by a single lens into the cavity. This beam is orthogonally polarised to the weak locking beam. This is required so that no light from the strong beam leaks onto the phase-sensitive photo-detector which is used to produce the error signal for the PDH locking. The power build-up factor of the cavity is 33 (calculated from the measured intra-cavity intensity as described in section 6.5.5), which is less than expected for a finesse of $\sim$2000. Although our mode-matching is not perfect (between 30 and 50%, depending on alignment), this lower than expected value is attributed to the linewidth of the seed laser (not known) being much larger than the cavity (900 kHz). It should also be noted that the reflected mode in figure 6.6 is from that of the weak locking beam. Alignment of the weak beam was not critical as it was simply used for generating an error signal for locking. More effort was put into correct alignment of the strong trapping beam, with higher mode-matching efficiencies achieved (up to 50%).

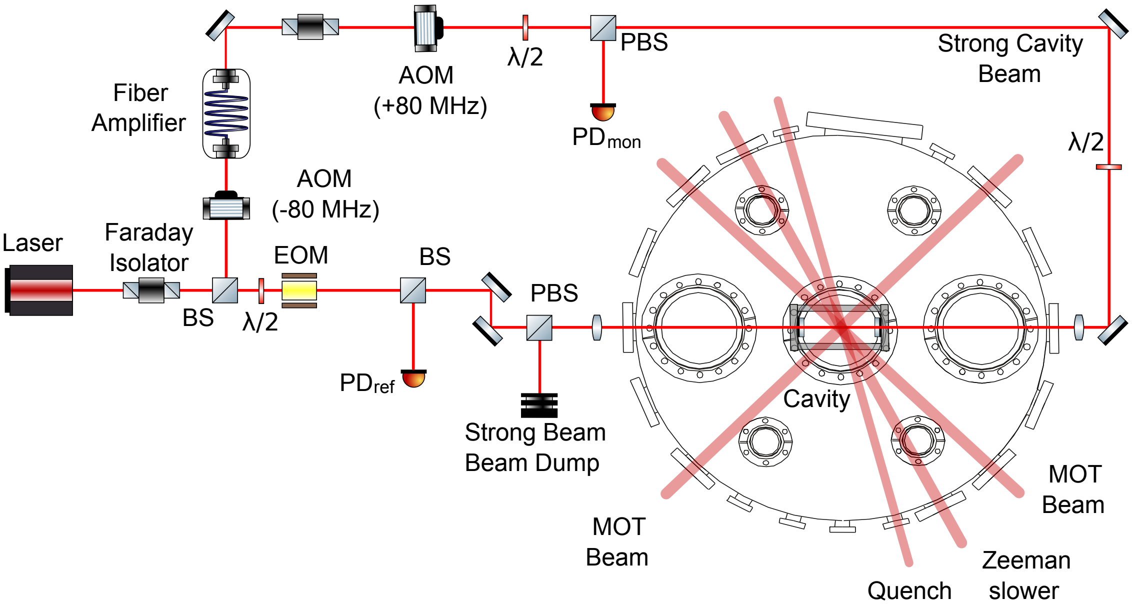

Figure 6.8: Optical layout for cavity trapping of metastable argon. Here the both the weak beam (used for cavity locking) and the strong trapping beam are displayed.

The quality and alignment of the polarisation optics is of utmost importance in the set-up. If any light from the strong beam leaks onto the locking photodiode (which monitors weak beam light reflected from the cavity), an undesirable beat pattern is formed between the strong and weak beams. This beat pattern leads to a modulation in the depth of the reflected mode and, in turn, this leads to a modulation of the amplitude of the locking error signal. This can result in noise in the circulating intensity inside the cavity or, in the worst case, to the cavity becoming unlocked. We found that a high quality polarising beam splitter with an extinction ratio of 100,000:1 was important as were zero-order wave plates, whose retardation is less temperature dependent.

By using an arbitrary waveform generator, the strong beam intensity can be rapidly changed by switching the AOM and controlling the diffracted intensity. The error signal produced by the weak beam is used to control a piezo-electric actuator glued behind one of the cavity mirrors. This provides a slow ($\leq$ 1kHz) locking signal to keep the cavity on resonance with the DPSS laser. The bandwidth of this lock is enough to account for noise present in most systems. A useful feature of having an AOM in the strong beam path is that we can effectively use it as a noise-eater[153] to remove any faster (up to 1 MHz) intensity fluctuations inside the cavity, by monitoring the transmitted intensity.

6.4 Trap alignment and loading

Metastable argon atoms are first prepared and cooled in the MOT[68,154]. While the cavity mount described in section 6.3.1 has the ability to finely adjust the cavity's position, it would be a slow and frustrating process to overlap the cavity focus with the MOT with this method only. If done this way, each time the cavity is moved it would have to be re-aligned and then checked to see if there is successful overlap with the MOT.

Because of this, the cavity was first placed manually (using the mount screws) as close as possible to the MOT position (this is very close to the centre of the chamber itself). The cavity was then aligned and the vacuum system was then pumped down to the pressures required to achieve a MOT. The cavity was locked and the intra-circulating power set to a fairly high level. The MOT cloud's position was then finely adjusted by carefully tweaking the currents in the compensation coils described in section 3.1.4.

In doing this we could move the position of the MOT by distances of up to 1 mm before the atomic cloud became destructively perturbed. The compensation coil currents were systematically varied to perfect the alignment. Overlap occurs when the Stark shift induced by the trapping beams reduces the fluorescence of trapped atoms in the MOT. Once the Stark shift was observed, loading of metastable argon could be attempted and when a trapping signal was detected, the MOT position was moved with respect to the center of the dipole trap to optimise trap loading. This was achieved by varying the MOT compensation coil currents until the maximum trapping signal was attained.

The experimental timing sequence (shown in table 6.1) consists of a 3 second MOT loading phase, followed by a ramping up of the intra-cavity intensity over a time between 20 ms and 500 ms (while the MOT beams and magnetic field are still on). By ramping the power up in this way up to 50% more atoms were loaded into the trap, compared to when the trap is switched on instantaneously. The variable time of the ramp depends on the power of the trapping beam. This is presumably because the Stark shift at maximal powers is large (of the order of 100 MHz) and so for higher intensities the ramp has to be longer in order to allow the MOT beams to more effectively dissipatively cool the atoms within the lattice sites themselves. Lower powers require only a fast ramp, and the ramp times were optimised regularly to obtain the maximal amount of trapped atoms.

	MOT loading (3 s)	Intensity ramp (20-500 ms)	Variable trapping time	Imaging (1-5 ms)
MOT beams	▨	▨		▨
MOT mag. field	▨	▨		
Zeeman slower	▨	▨		
Atomic beam	▨	▨		
Trapping beam		▨	▨	
Camera trigger				▨

Table 6.1: Experimental timing of loading metastable argon into the optical cavity trap. The shaded cells depict periods when a piece of apparatus is turned on.

Approximately 10^5 atoms can be loaded into the cavity trap, which is roughly half the number originally present in the MOT. After the cavity has reached the desired intensity, the MOT beams and magnetic field are switched off and a period of trapping in the cavity follows. The atoms are then released from the dipole trap and, with the MOT beams switched back on, can be imaged by fluorescence.

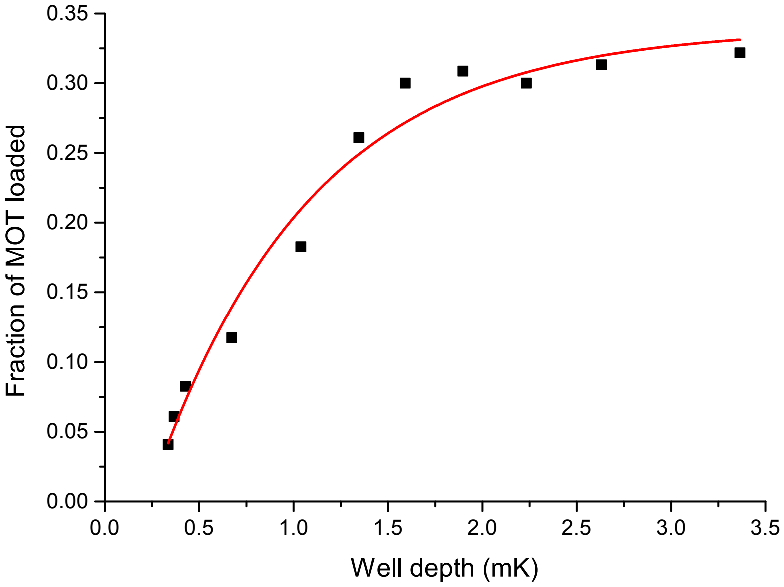

Figure 6.9: Graph showing how the loading efficiency depended on the trapping well depth.

Once atoms were successfully loaded into the trap, a study was performed to investigate how the efficiency of loading depended on well depths. The result of this is shown in figure 6.9. Here, the strong trapping beam power was varied and the amount of atoms initially trapped monitored by fluorescence imaging. The input power was converted to a well depth according to the technique described in section 6.5.5. As can be seen, loading is optimised at well depths of about 2-3 mK (the maximum possible well depth is 11 mK) where ~30% of the MOT is transferred to the cavity. Depending on alignment, this number can vary between 20 and 50%.

6.5 Results

6.5.1 Reduction of intensity noise

As with the CO_2 laser dipole trap described in chapter 4, vibrations from the turbo-molecular vacuum pumps led to a reduction in trap lifetime. The vibrations manifested themselves as intensity noise within the intra-cavity field and exponentially heated atoms out of the trap due to parametric heating. This was verified by taking a fast-Fourier transform (FFT) of the transmitted cavity light. For the cavity trap, the radial trap frequencies (which are measured in section 6.5.5) are in the kHz range and again similar to those produced by the turbo-molecular pumps.

However, there were no technical limitations with this trap that meant we could not compensate for the effect of these vibrations. Indeed the two-beam locking scheme displayed in figure 6.8 allows the use of the weak locking beam to generate an error signal and lock the cavity using the piezo (with a bandwidth of up to 3 kHz). The strong beam can then be independently modulated up to a bandwidth of 1 MHz, and this modulation can be used to provide compensation for intensity jitter within the optical cavity.

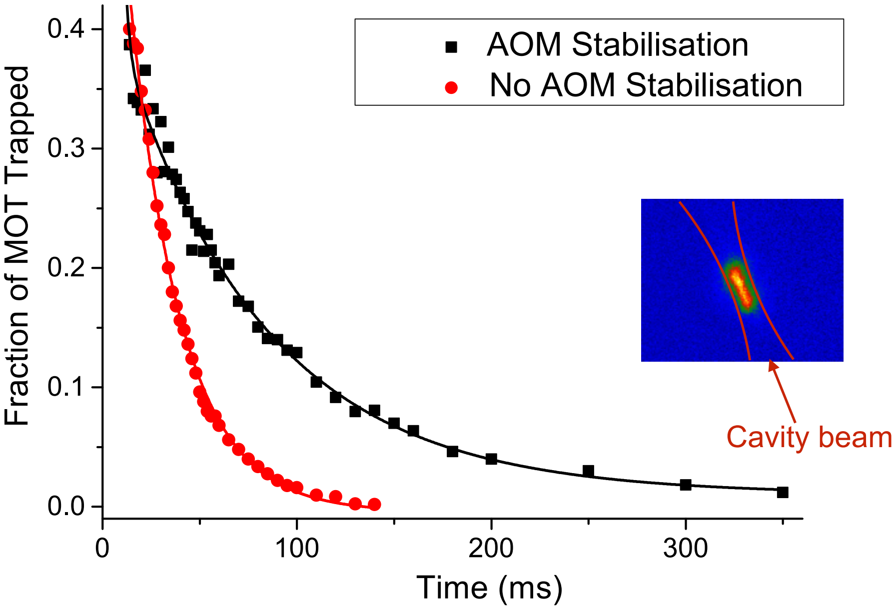

Figure 6.10: Lifetime curves of the optical cavity trap both with and without fast bandwidth stabilisation. The black squares and red circles depict the lifetime curve with and without fast-bandwidth stabilisation respectively. Inset in an example fluorescence image from the trap.

To do this, a photodiode is set up monitoring the portion of the strong trapping beam that is transmitted through the cavity. An electronic feedback loop is then created by using a servo controller (New Focus LB1005) and the strong-beam AOM can be used as a noise-eater.

When this faster bandwidth feedback was introduced, the noise at kHz frequencies was reduced by more than a factor of 100. Figure 6.10 shows measured trap lifetimes with and without the fast AOM intensity stabilisation. Without stabilisation the lifetime is shortened by parametric heating to 26±1 ms, but with feedback the lifetime is limited by Penning ionisation losses[79,80,82]. This lifetime varies between 70 and 300 ms, depending on the trapped atom density. Losses from the cavity trap will be characterised in much greater detail in the next chapter in section 7.4.1.

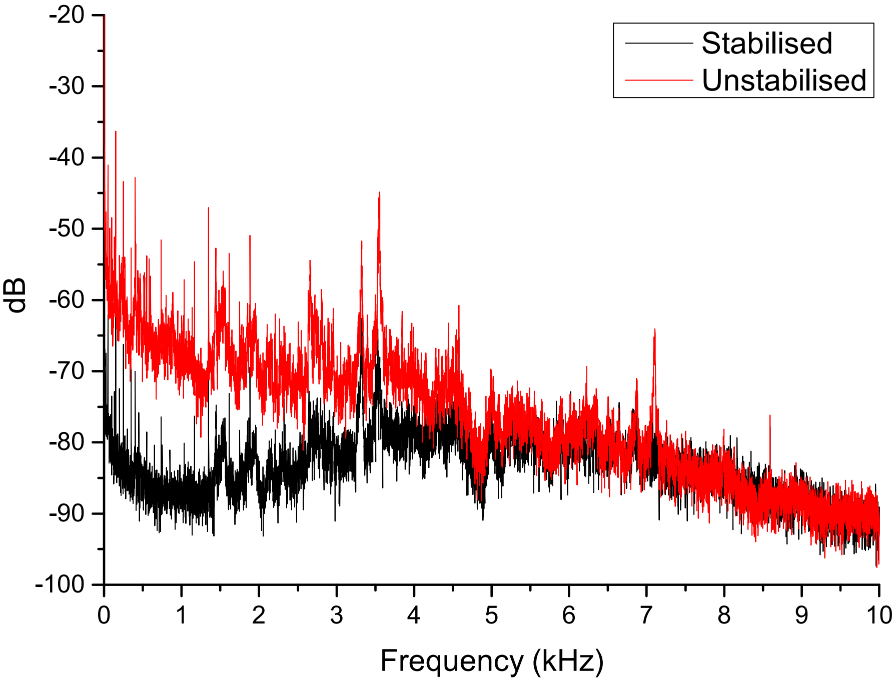

Figure 6.11: Fast-fourier transforms of the light transmitted from the cavity. When fast-bandwidth stabilisation was introduced, intensity noise was reduced by at least one order of magnitude.

To verify that the intensity noise on the intra-cavity beam was reduced, light transmitted from the cavity was monitored on a photodiode. A fast-Fourier transform was then taken of this signal (as shown in figure 6.11), and showed a reduction in intensity noise (at frequencies near the radial trap frequency) of at least one order of magnitude. As can be seen, for the case where there is no fast stabilisation, there are a large amount of peaks in the kHz range (relating to the frequency of vibrations created by the turbo-molecular pumps). Fast-bandwidth stabilisation reduced the amplitude of these peaks, to the extent where the trap lifetime is no longer effected by parametric heating (which was verified by artificially inducing small modulations at the trap frequencies and noting no lifetime shortening). There was little intensity noise beyond 10 kHz.

In general, intensity noise was the main contributing factor to the parametric heating out of the trap (over positional shaking). This is because only tiny positional movements manifest themselves as intensity noise within the cavity. The movement itself does not cause appreciable heating, but the intensity oscillations do. Therefore, by compensating for the intensity noise with a fast-bandwidth lock the trap lifetime is no longer limited by parametric heating.

6.5.2 Intra-cavity field switching and modulation

Once atoms are trapped, the amplified beam needs to be switched off quickly to release the atoms for time-of-flight temperature measurements and then turned on again at a later time when we want to re-trap. While turning the intra-cavity field off is not difficult, switching the field back on is more of a challenge because no error signal would be produced while the cavity beam is off. Here, the locking servo loop will have lost information about its previous locked state, making re-locking unreliable. Alternative methods to re-lock a cavity include the use of a flywheel circuit[155]. Here two servo locking loops are used; one loop corrects for slow frequency drift whose memory is stored while the cavity is unlocked. Another faster loop has its gain lowered during the unlocked period. This system works well for medium finesse cavities, but has only a limited capture range. Therefore if there is a large frequency drift during the time that the cavity is unlocked it may take a long time to re-lock, or even not lock at all. This re-locking scheme is less applicable to higher finesse cavities or in noisy systems, where frequency drifts may be significant compared to the linewidth.

The two beam locking scheme that we use enables the trapping beam to be independently varied without affecting the locking beam. The intra-cavity intensity can be switched off by simply blocking the strong beam, and we can ramp up the circulating power slowly, maintaining a lock at all times. Figure 6.12 contains graphs which show that the cavity stays locked with modulation of the strong beam intensity. Figure 6.12 a) is a plot of the voltage sent to control the diffracted light intensity from the AOM. This

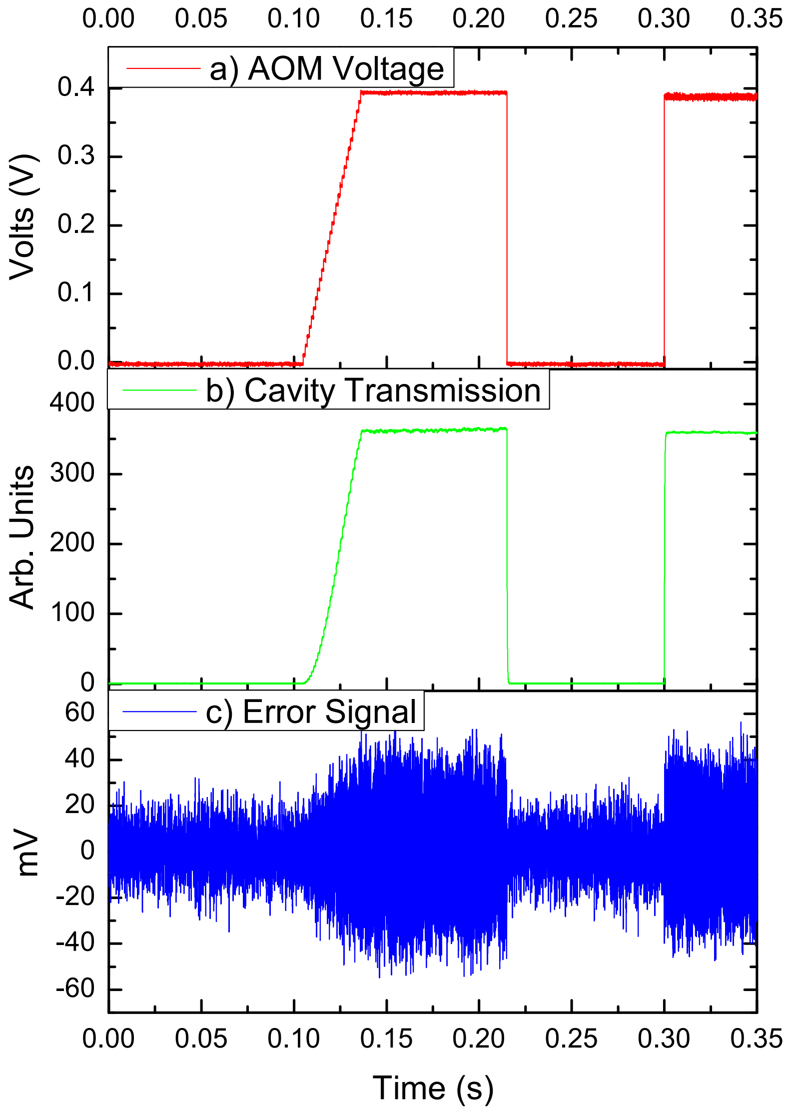

Figure 6.12: a) The control voltage signal sent to strong beam AOM to vary the input power into the cavity. b) The cavity transmission as a function of time while the input power is varied. c) The error signal created by locking beam as the input intensity is modulated.

light is then coupled into the cavity. Figure 6.12 b) is a corresponding measurement of the cavity transmission as a function of time. Note that high cavity transmission indicates high intra-cavity power. At full power (30 W) the intensity inside the cavity was $\sim 5 \times 10^{10}$ W/m^2. As can be seen the cavity transmission closely follows the voltage sent to the AOM, indicating that the cavity maintains lock for all times. Figure 6.12 c) shows the amplitude of the error signal measured during this time. The error signal increases for high circulating powers, compensating for the larger cavity perturbations at higher intensity.

By ramping the circulating power up slowly as shown in figure 6.12 b), 50% more atoms were loaded into the dipole trap compared to when the trap was immediately switched on. The ability to turn the trap off rapidly allows us to perform time-of-flight temperature measurements both with and without the ramp.

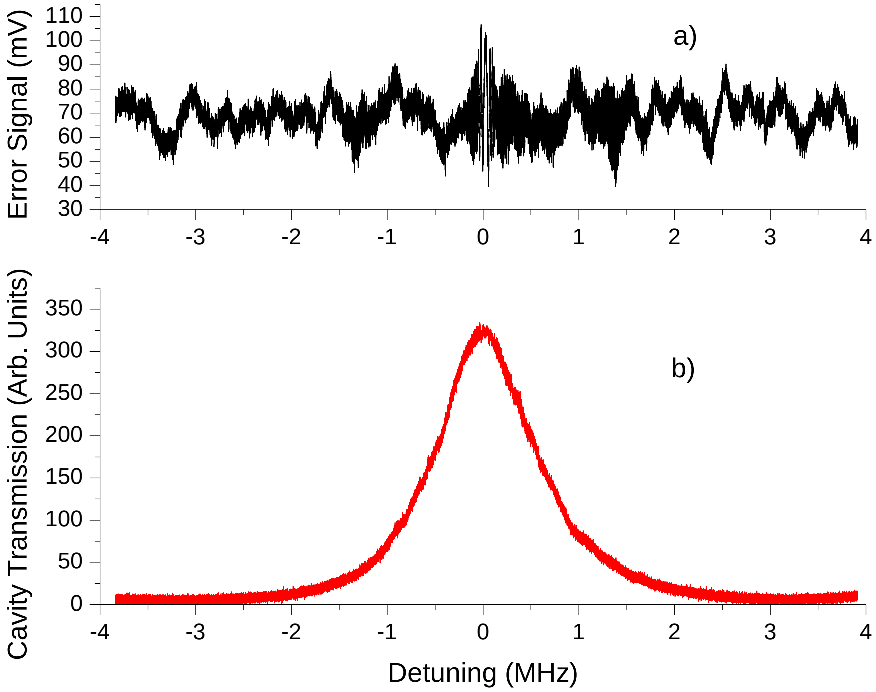

Figure 6.13: a) The PDH error signal produced while the strong beam is scanned in frequency. b) A graph of cavity transmission as a function of cavity detuning.

We also investigated the effect of frequency modulating the strong beam with respect to the locking beam frequency. This is of interest for cavity cooling of trapped particles[156,157]. Figure 6.13 shows the cavity transmission as the strong beam frequency is tuned over the cavity resonance. This is achieved by operating the first AOM at 80 MHz and scanning the second a few MHz around the original 80 MHz setting. While this causes a slight deflection of the strong beam the figure shows the cavity stays locked over the scan. At high intensities at zero detuning, the amplitude of the error signal significantly increases as can be seen in figure 6.12 c).

6.5.3 Temperature measurements

The ability to rapidly switch off the intra-circulating power within the optical cavity (as shown in figure 6.12) means that we can perform time-of-flight expansion temperature measurements. These are carried out in a similar way to that of calculating the MOT temperature as described in section 3.2.5. In doing this, we calculate a radial temperature of 190±20 μK and an axial temperature of 410±30 μK with the corresponding data shown figure 6.14.

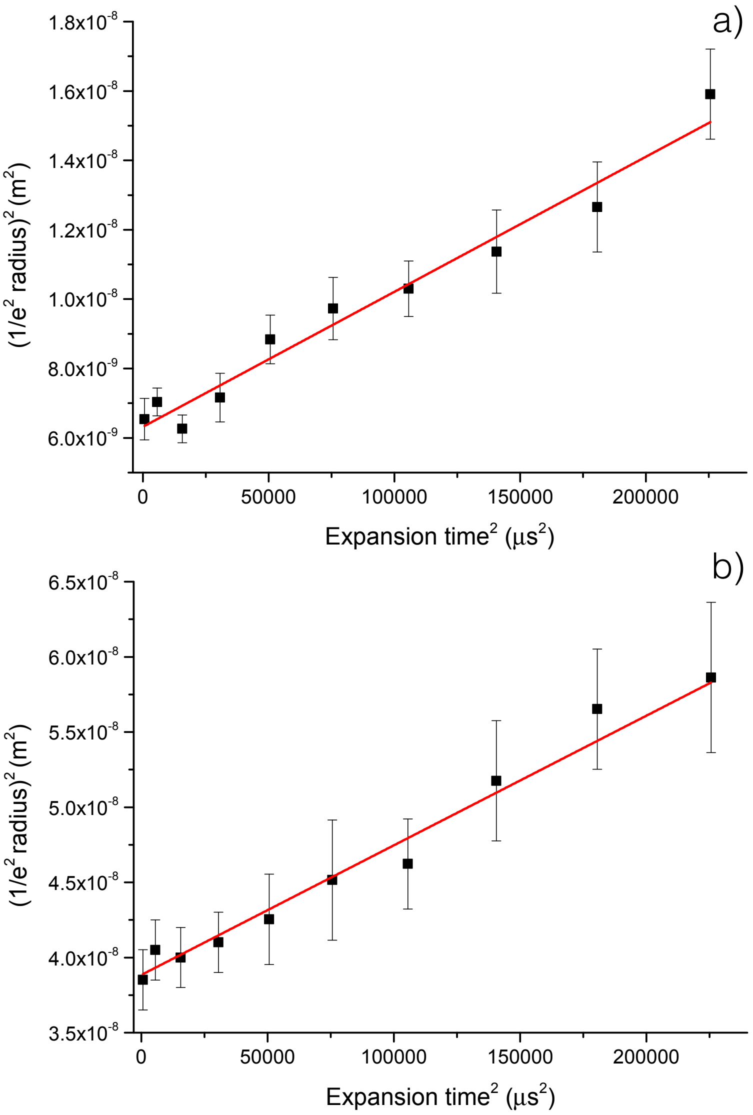

Figure 6.14: Time-of-flight expansion temperature measurements. The gradient of a) gives the value for $k_B T/m$ in the radial direction while b) is the same case for the axial direction.

To take this data, atoms were loaded into the trap and held for 20 ms. The cavity beam was then rapidly switched off and the trapped atoms allowed to freely expand for a variable period of time. After the expansion period, the MOT beams were turned back on and fluorescence images taken. From these images, the radial and axial widths of the cloud could be determined and used to calculate the temperatures. The difference in radial and axial temperatures is presumably due to the trapped cloud not thermalising fully within 20 ms of trapping (and atoms being more efficiently dissipatively cooled in the radial direction). It was not possible to attain accurate temperature measurements at much longer trapping periods due to there not being sufficient fluorescence signal.

To attain as estimate for the average cloud temperature we simply use the expression $T_{\mathrm{av}} = (2T_{\mathrm{rad}} + T_{\mathrm{ax}})/3$ to obtain an average temperature of $\sim$260 μK. The temperature of the cloud was also studied without ramping up the intra-cavity intensity slowly. Instead the trapping field was immediately turned on and an average temperature of 0.9±0.1 mK noted. In this way we can see that ramping the trapping field slowly not only increases the loading efficiency by 50% but also sucessfully increases the dissipative cooling inside the lattice while the cooling beams remain switched on.

6.5.4 Mirror heating

As shown in section 6.5.2, high circulating intensities can lead to strong perturbations to the cavity. This occurs because even small absorption in the mirror coatings can lead to significant heating for high intra-cavity intensities. Previous work[135,136] has characterised the change in mirror radius of curvature, but these are either measured in air or for much higher finesse cavities (with lower absorption coefficients than our cavity). In reference[135] a radius of curvature change of 105 μm/(MW/cm^2) was measured for a 6300 finesse cavity in air, while reference[136] measured between 47 and 60 μm/(MW/cm^2) for a 78,100 finesse cavity at a pressure of 1.3 $\times 10^{-5}$mbar. LIGO experiments have also put great effort into minimising thermal instability caused by cavity mirror heating[137].

We measured the radius of curvature change by noting the piezo voltage drift required to keep the cavity locked when the strong beam was switched on. Figure 6.15 a) shows this drift, while the cavity transmission is also measured. The cavity takes nearly 10 minutes to thermalise fully, and during this time the cavity transmission drops. This is because the radius of curvature is increasing to such an extent that the spatial profile of the cavity mode changes, and as a result the amount of in-coupled light decreases. When trapping cold atoms, the strong beam is on for no more than half a second out of a five second cycle so this heating is not a problem. The piezo voltage was calibrated to frequency by using the sidebands imposed on the weak beam. The equation for the cavity's resonant frequency is:

$$\nu = \left\{ q + (n + m + 1) \frac{1}{\pi} \cos^{-1}(1 - L/r) \right\} \frac{c}{2L} \tag{6.4}$$

and was used to convert a frequency change into a radius of curvature change[158]. In this equation q is the longitudinal mode number, n and m are the transverse mode numbers,

L is the length of the cavity and r is the radius of curvature of the cavity mirrors.

To verify that cavity length changes due to piezo movement do not significantly contribute to any frequency changes, we calculate the sensitivity with respect to small changes in both cavity length and radius. Assuming that L and r change from L_0, r_0 to $L_0 + \delta L_0, r_0 + \delta r_0$ the change in frequency is given approximately by:

$$\Delta\nu \approx \frac{\partial\nu\left(L_0, r_0\right)}{\partial L}\delta L_0 + \frac{\partial\nu\left(L_0, r_0\right)}{\partial r}\delta r_0. \tag{6.5}$$

We obtain $\frac{\partial\nu(L_0,r_0)}{\partial L}$ to be -9.30$\times10^8$ Hz/m and $\frac{\partial\nu(L_0,r_0)}{\partial r}$ to be -2.49$\times$ 10^{10} Hz/m. As the piezo can never move by more than a micron, this contribution to frequency is at most

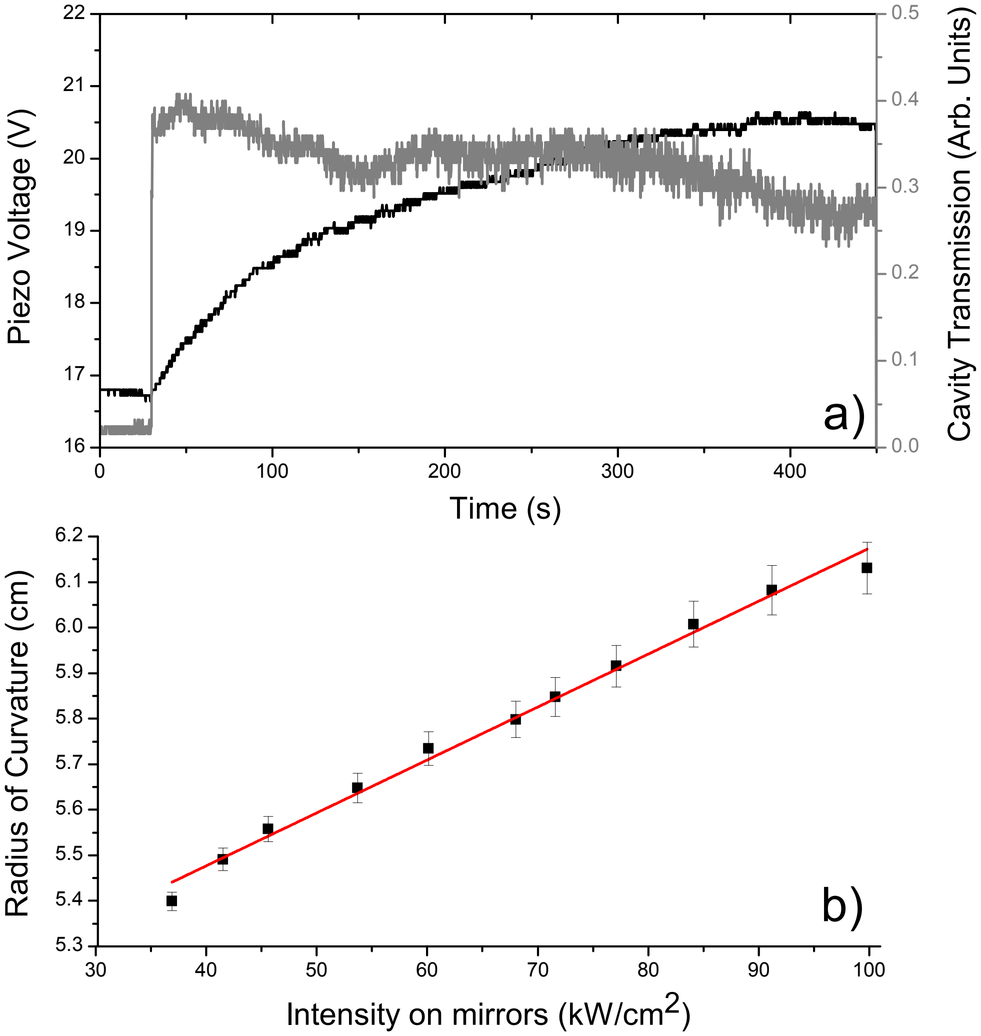

Figure 6.15: a) The black curve shows the drift in piezo voltage which is used to lock the circuit after the strong beam was turned on at t=30 s. The slow drift is due to mirror heating caused by the intra-cavity light. Also shown as the grey curve is the variation in cavity transmission over time. b) The calculated radius of curvature of cavity mirrors with the intensity on the cavity mirrors.

930 Hz. However as is shown in figure 6.15, the radius of curvature increases by slightly over 1 cm which equates to 249 MHz. Therefore the cavity length changes induced by heating are significantly less important than the changes in radius of curvature.

Figure 6.15 b) shows the calculated radius of curvature as a function of intensity on the mirrors. A linear fit for radius of curvature against mirror intensity gives 116±10 mm/(MW/cm^2). This is three orders of magnitude higher than previous work. This much larger change as compared to other works is due to the higher heating caused by larger absorption losses in our mirrors ($\sim$ 1000 ppm). In addition, the mirrors are not conductively cooled by surrounding air as they are placed in a high vacuum environment. For long periods ($\sim$ 8 minutes), input powers of much more than 2 W led to the cavity becoming unlocked before it thermalised fully. This is because the mode-matching efficiency decreases and the error signal amplitude is reduced. However, for our trapping applications, the strong beam is never on for more than half a second out of five and in this time the cavity maintains lock up to input powers limited by our amplifier (30 W).

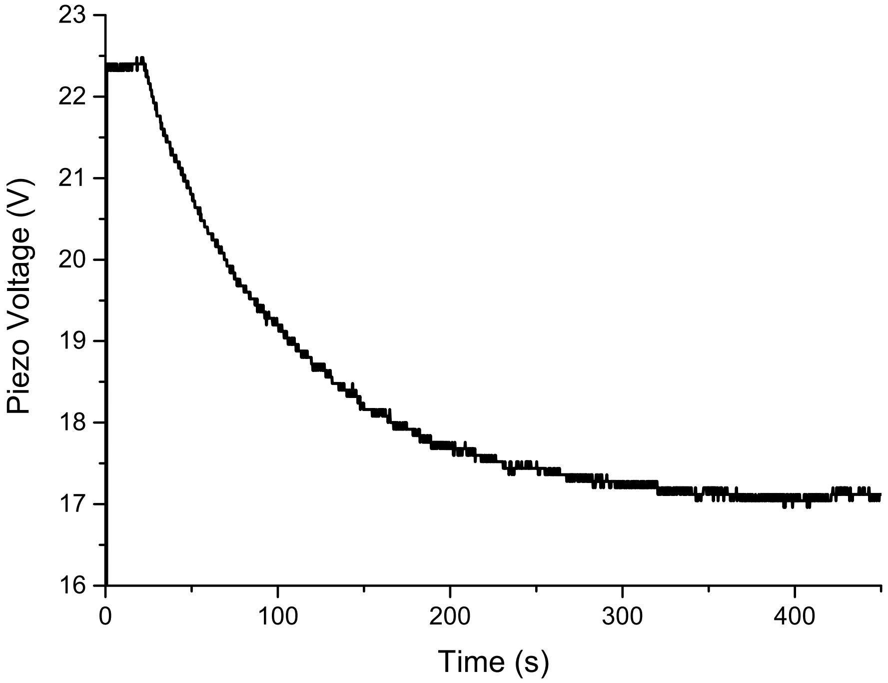

Figure 6.16: Example graph showing the cooling of the cavity over time (intra-cavity power is turned off at t$\sim$20 s). Here, the piezo voltage required to keep the cavity on resonance was monitored.

Once the cavity mirrors had been heated, it took a similar amount of time for them to cool down again (once the intra-cavity beam had be switched off). This cooling is shown in figure 6.16. Here, the piezo voltage required to keep the cavity on resonance was noted while the cavity was re-thermalising to its original temperature. The mirrors did not display any adverse effects from the heating.

6.5.5 Trap frequency and intensity measurements

Characterising the intensity circulating within an optical cavity and therefore the trapping well depths is not always a straightforward task. While this could be achieved by characterising the cavity mirrors reflectivity, absorption and transmittivity fully this would be a difficult measurement to perform and likely contain a large error. However, as our two-beam locking scheme allows us to rapidly modulate the trapping intensity, this can be used to parametrically heat atoms out of the trap. This would be resonantly enhanced when the modulation is at or near the trap frequencies. Therefore the measured trap frequencies of the atoms stored in the cavity can be used to determine the circulating intensity and cavity build-up.

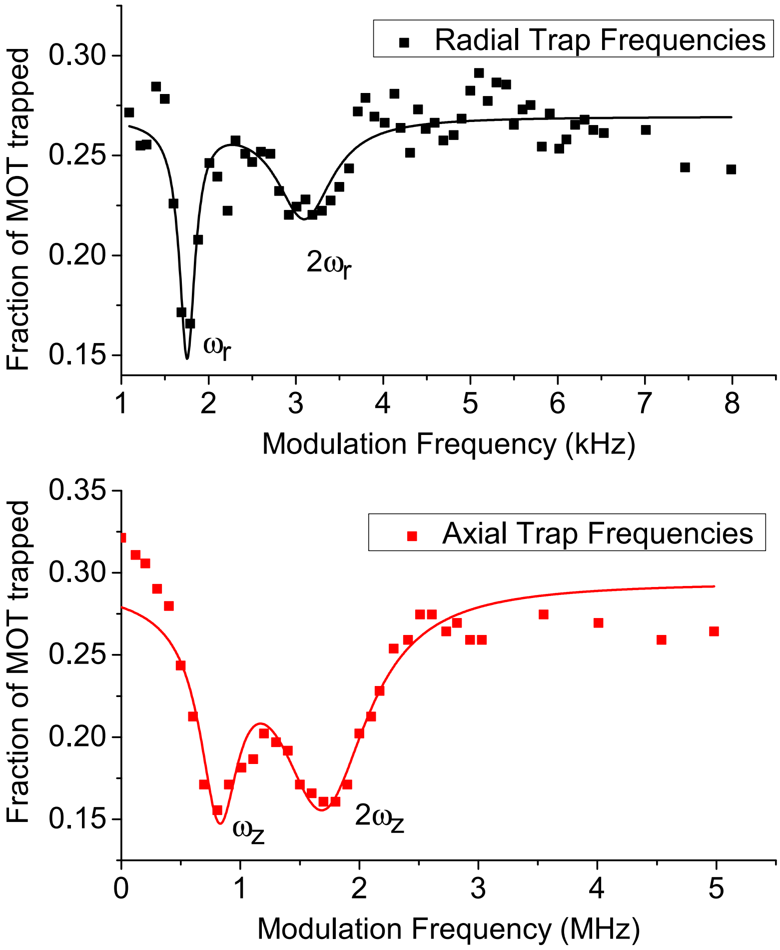

Figure 6.17: Graphs of the fraction of trapped atoms as a function of trap modulation frequency. The reduction in atom number indicates the location of the radial and axial trap frequencies. Significant loss also occurs at twice the trap frequencies.

Trap frequencies were determined by modulating the intensity of the strong beam using the AOM after the fibre amplifier. When the modulation was equal to or twice the trap frequency, strong parametric heating of the cold atoms occurs and they are lost from the trap[116]. Figure 6.17 shows the fraction of atoms remaining after a 10% intensity modulation for 20 ms. The strong loss in the kHz range give the radial trap frequency, and at MHz frequencies the axial frequency.

We measure a radial trap frequency ω_r of approximately 1.7 kHz, and a axial trap frequency, ω_z, of ~0.8 MHz, for an input power of 5 W. Assuming the harmonic approximation, the trap frequency is given by $\omega_z = 2\pi f_z = \sqrt{2\frac{U_0 k^2}{m}}$ and $\omega_r = 2\pi f_r = \sqrt{4\frac{U_0}{mw^2}}$ (where m is the mass of the trapped particle, U_0 is the well depth, $k = 2\pi/\lambda$ and w is the waist of the trap). These equations give a well depth of $\sim$ 1.8 mK at a 5 W input. In turn, by using the equation $U_0 = \frac{2\alpha}{\epsilon_o c} I_c$, where I_c is the one-way circulating peak intensity and α is the ground state polarisability of the trapped particle, we obtain a circulating intensity of 6.45×10^9 W/m^2. At the full power available (30 W) a trap depth of $\sim$ 10.8 mK is attained, using the polarisability of 47.9×10^{-40} Cm^{2}V^{-1} for metastable argon[159].

6.6 Conclusions

In this chapter I have demonstrated the creation of a deep optical trap for metastable argon by using a high power laser coupled to a medium finesse cavity. A novel two-beam locking scheme was used to provide rapid switching and modulation of the trapping beam. A weak beam was used to lock the cavity piezo (at a bandwidth of several kHz) by the PDH method. A strong beam of orthogonal polarisation was used for trapping and could be rapidly switched and modulated in both frequency and intensity as required for measuring the properties of trapped atoms.

The cavity was characterised to have a finesse of 2050±100 and a linewidth of 910±50 kHz and produced well depths of up to 11 mK for metastable argon. The ability to rapidly modulate the trap allowed us to both reduce intensity noise within the trap and allowed us to perform time-of-flight temperature measurements and to measure the trap frequencies by artificially inducing parametric heating out of the trap. The average temperature was measured to be ~260 μK and the trap frequencies were noted to be 1.7 kHz in the radial direction and 0.8 MHz in the axial direction. Although we measured changes to the cavity induced by heating of the mirrors by the intra-cavity field, this did not limit the trap depths attainable. The two-beam locking scheme also allowed us to slowly ramp up the intra-cavity intensity which improved both the loading into the trap and dissipative cooling within the lattice.

Due to the deep well depths this cavity could also provide high enough trapping intensities to trap ground-state argon, the procedure of which is detailed in the next chapter.

Chapter 7

Far-off resonance build-up cavity: ground state argon trapping

7.1 Introduction and motivation

The development of methods to create, control and manipulate the motion of cold complex molecules has, over the last ten years, allowed the study of atomic and molecular interactions with unprecedented precision. Cold molecules offer a new testbed for precision measurement[160] and the exploration of cold collisions and chemistry[161]. Cold polar molecules are seen as promising candidates for studying condensed matter physics[162] and even quantum information science[163]. Of central importance to these applications has been the development of techniques to create translationally cold molecules that are either in their absolute internal ground state or a well defined internal ro-vibrational state. However, while many slow complex species can now be produced by methods such as Stark and Zeeman deceleration[46,57,61], these non-dissipative methods are realistically limited to temperatures in the mK range since the high energy particles must be discarded to reduce the translational energy spread. Truly dissipative methods are therefore required to further cool molecules into the sub-mK regime where quantum effects will become dominant[34].

Sympathetic cooling is a promising general method for dissipative cooling, but typical laser cooled species are generally reactive and cannot generally be utilised[73]. Trapped noble gas atoms in their ground state appear to be an ideal candidate for the sympathetic cooling of molecules[75,164,165] as they are chemically inert and can be laser-cooled to μK temperatures in an excited metastable state. Cold helium gas has already been used extensively to buffer gas cool many species but temperatures are limited to the 100 mK range[69]. In addition, as these atoms are in their absolute ground state, inelastic state changing collisions which can prevent efficient collisional cooling can be reduced or avoided. All of the noble gas atoms have been laser cooled in a metastable state[76–83] and all but helium can be quenched to its non-reactive ground state by dipole-allowed transitions. However, once in their ground state they have no magnetic moment and cannot be trapped in a magnetic trap. Finally, ground state noble gases are difficult to detect using CW laser spectroscopic methods because the first dipole allowed transitions are in the vacuum ultraviolet where no available CW laser sources exist.

Ground state noble gas atoms can be trapped in an optical dipole trap, despite their ground state static polarisabilities being at least an order of magnitude smaller than typical laser cooled species, since large optical fields detuned far from resonance can be used to trap them. Such large CW fields can be produced in optical buildup cavities, which have previously been used to create deep traps for a range of atomic species[138–140,166]. Additionally, species that cannot be directly observed can be detected when simultaneously trapped with another species that can be probed spectroscopically. This can be accomplished because the interactions between the two species in a trap perturb the motion of the observable species via intra-trap collisions. Examples include atomic ions that are sympathetically cooled by other trapped ions or ions produced by chemical reactions with others in the trap[167]. Detection is accomplished by modulating the trap potential to parametrically heat the species that cannot be directly observed. This frequency is usually unique to each trapped species because of their differences in mass. The modulation heats the species which can be observed and is detected as a change in the fluorescence monitored from the trap. By recording the trap fluorescence as a function of modulation frequency a type of species-specific mass spectrometry has been achieved in ion traps. In neutral atom traps parametric heating is a well established way of characterising the trap. For example, the loss induced by parametric heating is commonly used to identify trap frequency and therefore trap depth for a particular species[168]. In addition, by tuning slightly away from the parametric resonance, selective removal of hot atoms in the trap has been demonstrated[169].

In this chapter we describe dipole trapping of cold ground state argon atoms suitable for the sympathetic cooling of molecules. We also demonstrate the detection of the ground state by using a type of parametric loss spectroscopy based on co-trapping a small fraction of metastable argon atoms. This allows us to simultaneously measure the presence of ground state argon atoms as well as the polarisability of the metastable state at the trapping wavelength of 1064 nm. Finally, we measure (the first time that this has been done), Penning and associative losses of trapped metastable atoms in the absence of resonant laser light and determine the loss rate for metastable atoms by collisions with the co-trapped ground state atoms.

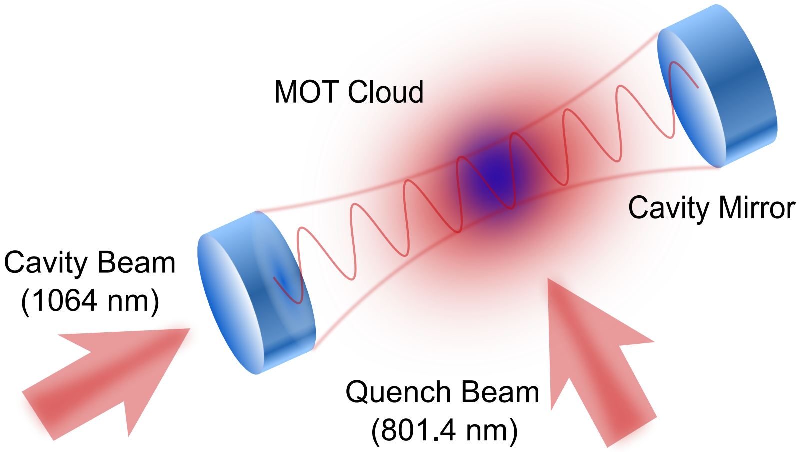

Figure 7.1: Schematic of the optical cavity. Metastable argon is first cooled in a MOT, and then quenched down to the ground state. Both species can be trapped in the lattice formed within the optical build-up cavity.

7.2 Quenching down to the ground state

As has already been described, due to the ground-state cooling transitions for the noble gases being in the deep ultra-violet, atoms first have to be excited and cooled in a metastable state. For sympathetic cooling purposes these atoms must then be transferred back down to the ground state by an optical quenching process. Table 7.1 shows the quenching wavelengths and associated recoil temperatures for the noble atoms. Quenching wavelengths are included for all atoms apart from Helium which cannot be optically quenched but can be transferred to the ground state by Stark induced transitions[170].

As can be seen, the recoil temperature depends on the mass of the quenched atom and so Helium is unsuitable for sympathetic cooling of molecules below the mK range. Argon was originally selected due to its combination of favourable elastic cross-section with molecular hydrogen[84] and benzene[85]. Moreover, the recoil temperature is suitable for sympathetic cooling down to ultracold temperatures.

To quench metastable argon down to the ground state requires a laser operating at

	^{4}He*	^{20}Ne*	^{40}Ar*	^{84}Kr*	^{132}Xe*
λ_{cool} (nm)	1080.3	640.2	811.5	811.3	881.9
T_{Doppler} (μK)	39	203	141	133	116
$\lambda_{\mathrm{quench}}$ (nm)	-	633.4	801.4	810.4	979.9
T_{recoil} (μK)	1216	261	66	25	11

Table 7.1: Here we show the cooling wavelengths and doppler temperatures for cooling of the metastable rare gas atoms (wavelengths taken from NIST atomic spectra database) along with the quenching wavelengths and relevant recoil temperatures from the quenching process.

801.4 nm. The effect of this is to first excite atoms from the 4s$[3/2]_2$ metastable state to the 4p$[5/2]_2$ state, from which they decay to the ground state via either the 4s$[3/2]_1$ or 4s$[1/2]_1$ states (as displayed in figure 7.2). The maximum photon recoil temperature from this process is 68 μK, which places a limit on the lowest temperature of the trapped ground state.

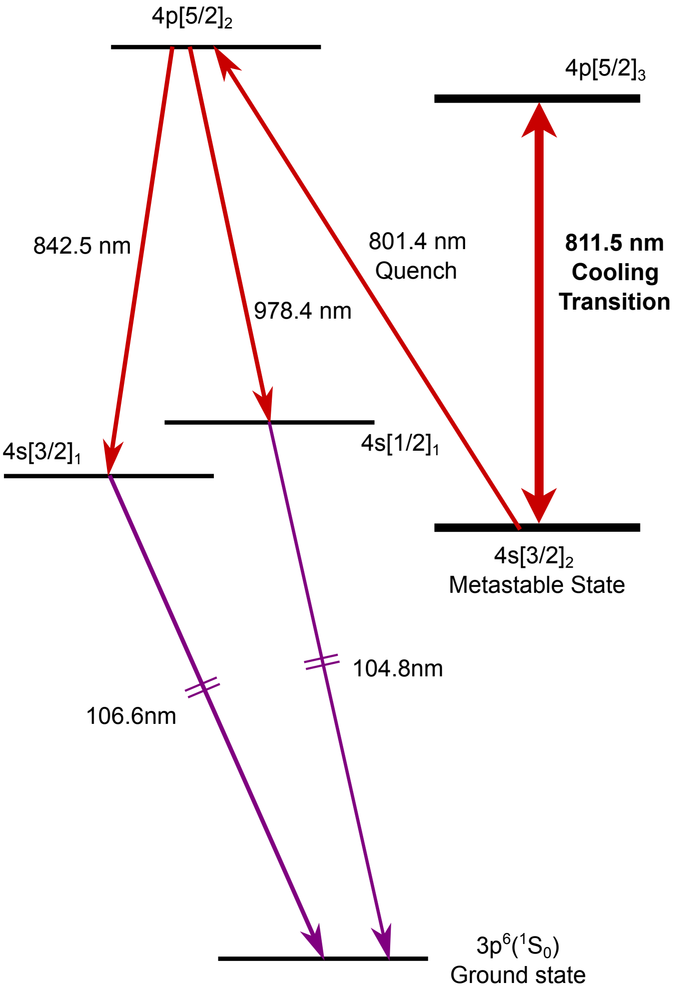

Figure 7.2: Energy level diagram of the relevant transitions in argon. Here, both the closed-cycle cooling transition and the optical quenching process is shown.

The laser itself simply consists of a free-running laser diode (Thor labs product no.

LD808-SA100) mounted in a commercial diode mounted with integrated TEC (Thor labs TCLDM9). As 801.4 nm is a somewhat awkward wavelength for a diode (most are at 808 nm and would have to be considerably temperature tuned downwards) a diode was requested with the centre wavelength as close to the quenching wavelength as possible. The diode we received was designed to have a centre wavelength of 808 nm (at room temperature) but reached 801.4 nm at 31.5 °C.

To correctly set the wavelength of the quenching diode, a wavelength-meter was first used to get an approximate value for the temperature of the diode. The beam was then set to a high power (∼100 mW), collimated and enlarged to give a beam diameter of roughly 1 cm. It was then aligned through the centre of the science chamber and due to the quench beam being large we could be sure that it was overlapped with the MOT cloud. The temperature of the quench laser was then slowly varied until a dip in MOT fluorescence was noted. This corresponded to quenching of the metastable atoms in the MOT cloud down to the ground state, where they no longer fluoresced under the presence of the cooling beams.

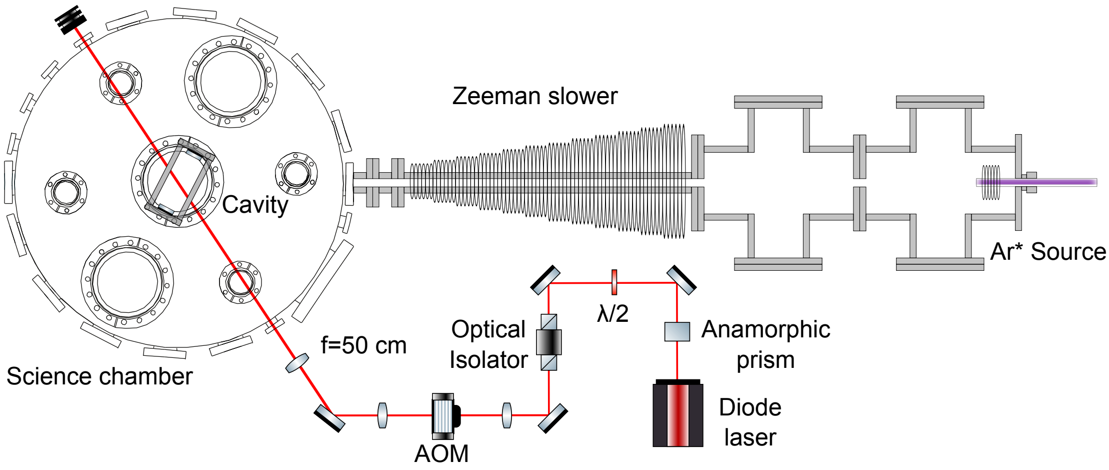

Figure 7.3: Schematic showing the path of the quench laser beam.

When the quench beam had such a large diameter, the laser tended to drift off the quenching transition within a few minutes (presumably due to slight thermal fluctuations). To counter this, and to avoid implementing a lock on the laser, the beam was tightly focussed such that power-broadening effects meant the laser quenched effectively for long periods. By doing this, the laser stayed on the quenching transition for several days at a time without the temperature or current needing adjustment.

The path of the quench beam is shown in figure 7.3. Here, the beam is aligned through an anamorphic prism and isolator before being passed through an AOM so that the beam can be rapidly switched on and off. The beam is then focussed through the MOT cloud using a lens of 50 cm focal length with the fluorescence of the MOT monitored and minimised so that successful overlap with the atomic cloud can be verified.

7.3 Loading of ground state argon

The experimental timing procedure for loading ground state atoms into the trap is displayed in table 8.1. It firstly consists of loading the cavity with metastable atoms in the same way as described in section 6.4. Once metastable atoms have been successfully loaded, the quench beam is switched on for a period between 100 μs and 2 ms. This variable period of time allows us to select how many metastable atoms are quenched to the ground state.

	MOT loading (3 s)	Intensity ramp (20-500 ms)	Quenching period (0.1-2 ms)	Variable trapping time	Imaging (1-5 ms)
MOT beams	▨	▨	▨		▨
MOT mag. field	▨	▨	▨		
Zeeman slower	▨	▨	▨		
Atomic beam	▨	▨	▨		
Trapping beam		▨	▨	▨	
Quench beam			▨		
Camera trigger					▨

Table 7.2: Experimental timing of loading of both metastable and ground state argon atoms. The variable quenching period allows us to select the proportion of metastable atoms that are quenched.

After atoms have been quenched they are held for a variable period and after this time the trap is re-illuminated by the MOT beams and the remaining metastable atoms detected by their fluorescence. As ground state atoms are “dark” (as least in regards to this experiment) they cannot be detected in the same way as the ground state atoms are. We monitor intra-trap collisions and use them to characterise an additional loss channel (for the detected metastable atoms) to detect the presence of ground state argon within the trap. This characterisation and detection is detailed in the next section.

7.4 Detection of ground state argon and results

Detecting trapped ground state atoms is a challenge due to the short wavelengths required to excite atoms from the ground state. Due to this, we cannot detect them in the same way as metastable atoms and have to use a different technique. One option would be to perform a 3 + 1 resonantly-enhanced multi-photon ionisation (REMPI) process at 261.27 nm[171]. This, however, would involve the use of a dye laser which was not available for the timespan required for the work presented in this thesis. In view of this, we decided to simply load co-trap ground state and metastable atoms together and monitor the additional loss channel from ground state and metastable atomic collisions.

We achieved this by using two separate methods. We firstly took lifetime curves in the cases where only metastable atoms were trapped and then when both ground state and metastable atoms are co-trapped. The decay of the metastable atoms was then monitored for both cases and curves fitted to them fully describing the loss. The second method involves parametrically heating the ground state atoms out of the trap. As ground state atoms have a polarisability of ~ 40 times less than metastable atoms, the two species have different trap frequencies. If the ground state atoms are heated out of the trap early on in the trapping process, then there are less intra-trap collisions between metastable and ground state atoms and any extra metastable loss induced by this process minimised.

7.4.1 Intra-trap collisions

The lifetime-limiting trap losses have already been touched upon for the both the case of the MOT in section 3.2.4, and also the metastable argon trap in section 6.5.1. As metastable argon atoms have intrinsically high internal energy, an intra-trap collision can lead to either a Penning ($Ar^* + Ar^* \rightarrow Ar + Ar^+ + e^-$) or associative ionisation process ($Ar^* + Ar^* \rightarrow Ar_2^+ + e^-$). Both are inelastic state-changing collisions in which both metastable atoms are lost. If the trapped atoms are not spin-polarised, then for most metastable atoms the loss rate is of the order of 10^{-10} cm^3/s and trap lifetimes are ultimately limited by these interactions[83].

For trapping of metastable atoms only, trap loss from the optical lattice in the build up cavity can be described by a differential equation:

$$\dot{\rho_e} = -\Gamma \rho_e(t) - \gamma_{ee} \rho_e(t)^2, \tag{7.1}$$

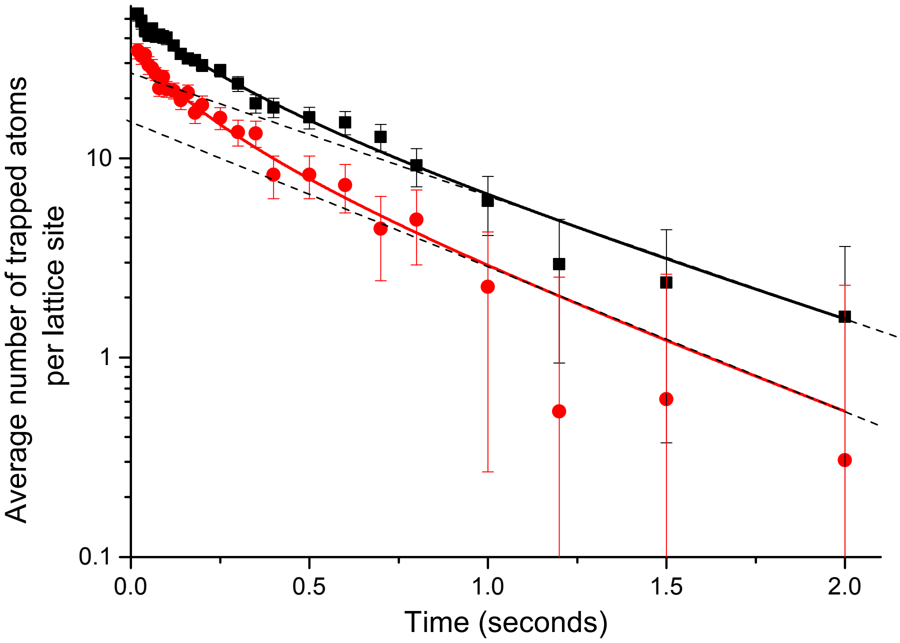

Figure 7.4: Lifetime curves which plot the average number of trapped metastable atoms in a the lattice trap as a function of time. The higher plot arises when only metastables are trapped (black squares). The lower curve (red circles) is recorded when both metastable and ground state atoms are co-trapped. The dashed lines show how the atoms would decay if only collisions with background gases caused trap loss. These lines highlight how the early behaviour is dominated by Penning and associative losses. The error bars originate from the standard error of 20 images averaged for each data point. The solid lines are fits from equation 7.2.

where ρ_e is the density of trapped metastable atoms, Γ is the one-body loss coefficient (i.e. mostly caused by collisions with background atoms) and γ_{ee} is the two-body loss coefficient (caused by metastable intra-trap collisions). If the effective trap volume is not time-dependent, the number of trapped atoms is given by

$$\rho_e(t) = \frac{\Gamma \rho_e(0) e^{-\Gamma t}}{\gamma_{ee}\rho_e(0)(1 - e^{-\Gamma t}) + \Gamma}, \tag{7.2}$$

where $\rho_e(0)$ is the initial density of metastable atoms.

Fig. 7.4 displays two lifetime curves; one loaded with only metastable atoms (black squares) and the other with both ground state and metastable atoms (red circles). Note that in each case the first few hundred milliseconds of the lifetime curve (when the density is highest) deviates from a single exponential decay. We attribute this loss to Penning and associative losses for the case when only metastable atoms are loaded into the trap. The remaining loss after this time is primarily due to background collisions. To see this, an additional line has been placed on the graph demonstrating what the lifetime curve would be if only background collisions with a single exponential decay contributed. When both species are loaded into the trap the number of metastable atoms is observed to decrease more quickly when compared to the case of metastables only. This is discussed in detail further below.

Equation (7.2) was first fitted to the decay curve corresponding to only metastable atoms loaded into the trap. The one-body loss coefficient, Γ, was determined from the fit to be 1.3 ± 0.1 s^{-1} and the two-body loss coefficient, γ_{ee}, is $(3.3\pm0.8)\times10^{-10}$ cm^{3}s^{-1}. Our two-body loss coefficient, γ_{ee}, is lower than a previously measured value[80] of $(5.8\pm1.7)\times10^{-10}$ cm^{3}s^{-1}. The previous value, however, was measured in a MOT without extrapolation to vanishing MOT light intensity. Light-assisted collisions artificially raise the measured value, which is in keeping with our lower value measured in the off-resonant lattice. The total cross section between background ground state and metastable atoms $\sigma_{ge} = \Gamma/\rho\bar{v}$ (where σ_{ge} can be determined from the loss coefficient, ρ is the background density of ground-state argon in the vacuum chamber and $\bar{v}$ is the mean relative velocity). Because the efficiency N_{ar}/N_{ar^*} of the RF discharge is $\sim10^5$, the background gas primarily consists of ground state argon atoms. Due to this, we can use the one-body loss coefficient to calculate the total elastic cross section between ground state and metastable atoms. In doing so, we obtain a value of $(1.7\pm0.8)\times10^{-13}$ cm^2 for room temperature collisions. While this number in practice comprises of both inelastic and elastic cross-sections, in practice inelastic processes are negligible to elastic ones. The error primarily results from uncertainty in background pressure of $\sim 8\times10^{-9}$ mbar. This total cross-section is a combination of elastic metastability exchange[172,173] and direct processes and corresponds well to a value of 5.6×10^{-14} cm^2 determined at higher energies and with theoretical values[174,175].

Modelling the case in figure 7.4 where we co-trap both ground state and metastable atoms together (red circles) is more complicated. Simply fitting equation (7.2) to this curve is not strictly correct as there are additional collisions between the ground-state and metastable atoms. If equation (7.2) was fitted to this curve then we would obtain a two-body loss coefficient, γ_{ee}, of $(7.4\pm2.4)\times10^{-10}$ cm^{3}s^{-1} and a one-body loss coefficient, Γ, of 1.5 ± 0.4 s^{-1}. While this is not a correct analysis of this data, it does display the surprisingly strong effect on the metastable atoms of the co-trapped ground state atoms.

Because of this substantial effect on the loss of metastable atoms, it was not initially clear whether elastic or inelastic collisions between the ground state and metastable atoms were causing this additional loss from the trap. Although elastic collisions are expected to

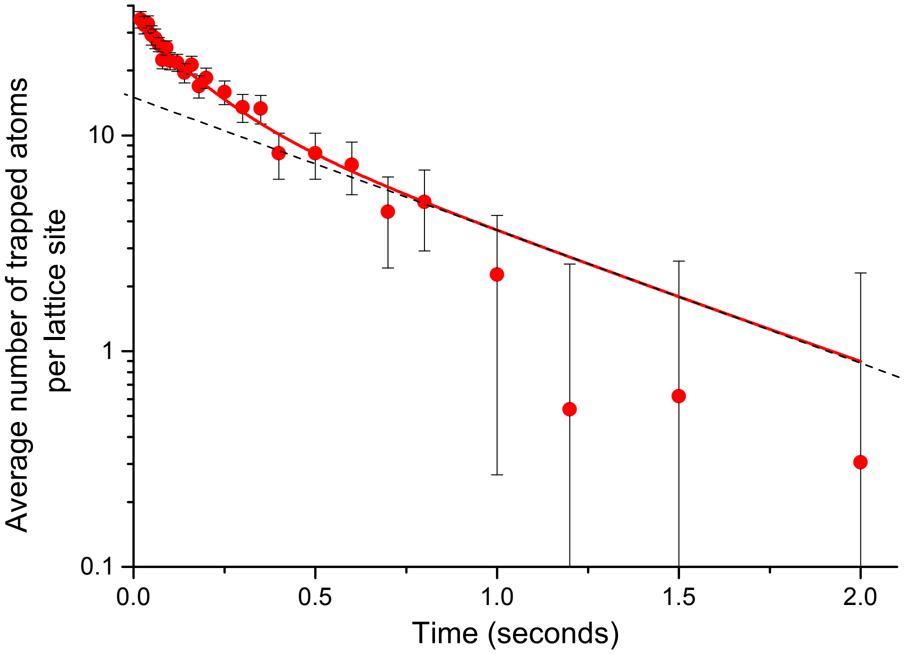

Figure 7.5: Here, both ground state and metastable atoms are loaded into the trap. The approximation to the coupled differential equations 7.3 and 7.4 is fitted to the lifetime curve.

dominate over inelastic collisions[175–178], they cannot directly lead to loss of the metastable atoms.

To establish what type of collisions were leading to the additional loss within our trap, it was decided to first model the collisions on the assumption that they were inelastic. In such a collision, both the ground state and metastable atom are expected to be ejected from the trap after a collision. To model this process we have two coupled differential equations, which describe the decay of both species:

$$\dot{\rho}_e = -\Gamma\rho_e - \gamma_{ge}\rho_g\rho_e - \gamma_{ee}\rho_e^2 \tag{7.3}$$

$$\dot{\rho}_g = -\Gamma\rho_g - \gamma_{ge}\rho_g\rho_e, \tag{7.4}$$

where ρ_g is the ground state density and γ_{ge} is the loss coefficient during a ground state-metastable collision. To obtain an approximation to these equations we use the the Picard-Lindelöf theorem[179,180], a description of which is given in appendix C.

This approximate solution (equation (C.7) in the appendix) is fitted to the lifetime curve when both metastable and ground state atoms are fitted, an example fit of which is shown in figure 7.5. To avoid over-parameterising the fitting routine, γ_{ee} and Γ were fixed at the already calculated values of $(3.3 \pm 0.8) \times 10^{-10}$ cm^{3}s^{-1} and 1.3±0.1 s^{-1} respectively (for the case when only metastable atoms were trapped). In doing so, we found the loss coefficient of a ground state and metastable collisions (presuming that the collisions are inelastic), γ_{ge}, to be $(9 \pm 6) \times 10^{-10}$ cm^{3}s^{-1}.

While the fit to the data was good, this is an extraordinarily large value and is many orders of magnitude larger than rate-coefficients in high pressure plasmas[178]. Therefore our resultant inelastic cross-sections would be substantially larger than those generally accepted[175–178], particularly at the cold temperatures in our trap.

Based on our calculated values and the fact that at our temperatures elastic collisions should dominate, we therefore conclude that the loss within our trap is not due to inelastic collisions, but elastic ones. While elastic collisions cannot lead to direct metastable loss, any collision with a ground state atom will, on average, lead to a cooling of the metastable atom. This is because the optical well depth for ground state atoms is approximately 40 times lower than for metastable atoms, and the trapped ground state atoms are therefore colder. This process leads to sympathetic cooling of the metastable atoms. We conclude that the increase in the metastable atom density by this cooling process (which results in compression within the trap) leads to greater loss by Penning and associative inelastic collisions when compared to the case of only metastable atoms loaded into the trap. This is what we observe in our experiments and is shown in figure 7.4. We model this loss process again using equation (3.16), but allow the trapped volume of the metastable atoms to decrease with time as expected with cooling. Values for γ_{ee} and Γ are set at the previously measured value. As we measure the metastable number as a function of time we recast equation (7.2) to obtain the effective volume change and therefore the temperature as a function of time:

$$V(t)(\propto T^{3/2}) = \frac{N(t)\left(\gamma_{ee}\frac{N_e(0)}{V(0)}(1 - e^{-\Gamma t}) + \Gamma\right)}{\Gamma\frac{N_e(0)}{V(0)}e^{-\Gamma t}} \tag{7.5}$$

The effective volume is then converted into a temperature (the result of which is shown in figure 7.6) by the following equation:

$$V_{\text{eff}}(t) = \left(\frac{4\pi k_B T(t)}{m}\right)^{3/2} \frac{1}{\bar{\omega}^3} \tag{7.6}$$

where $\bar{\omega}$ is the geometrically averaged trap frequency and is equal to $\bar{\omega} = \omega_{\text{rad}}^2 \omega_{\text{ax}}$.

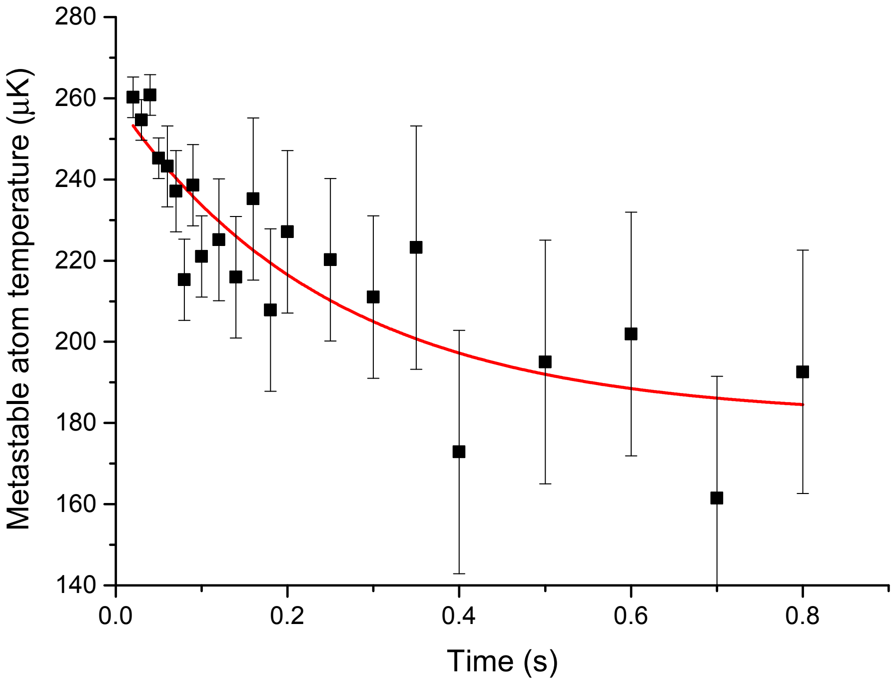

Figure 7.6: Graph showing the variation of metastable atom temperature over time. These temperatures are calculated by monitoring the volume change over time from equation 7.5 and converted to a temperature. The thermalisation time in this figure is 0.25 s, and can be used to calculate an approximate total elastic cross-section for ground state collisions with metastable atoms.

From figure 7.6, we can see that the initial temperature of trapped metastable atoms is 260 μK: these atoms are then cooled to temperatures of $\sim$200 μK within 0.5 s. This is a result of the intra-trap collisions between metastable atoms and the colder ground-state atoms. From the data in figure 7.6 we obtain an e^{-1} thermalisation time of 0.25 s. As this process is dependent on the collision rate with trapped ground state argon atoms, we can therefore use this thermalisation time to obtain a total collisional cross-section between metastable and ground state atoms. The following derivation is analogous to previous and similar experiments involving the sympathetic cooling of ^{7}Li atoms by using ^{133}Cs atoms[32,33]. Marcel Mudrich's thesis[181] in particular offers a very thorough overview of the derivation.

We can now consider the case where both metastable and ground state atoms are trapped together in a dipole trap. The static polarisabilities, α_e and α_g, are different and this leads to differing potential well depths in the ratio $U_e/U_g = \alpha_e/\alpha_e$ ($\sim$ 40 in our case). The collision rate describes the thermalisation process between the two species and is of the form:

$$\Gamma_{eg} = \langle \sigma(v_r) v_r \rangle_{r,v_r} \tag{7.7}$$

$$= \int d^3r \int \frac{d^3p_e}{(2\pi\hbar)^3} \int \frac{d^3p_g}{(2\pi\hbar)^3} f_e(\boldsymbol{r},\boldsymbol{p}_e) f_g(\boldsymbol{r},\boldsymbol{p}_g) \sigma\left(\left|\frac{\boldsymbol{p}_e}{m} - \frac{\boldsymbol{p}_g}{m}\right|\right)\left|\frac{\boldsymbol{p}_e}{m} - \frac{\boldsymbol{p}_g}{m}\right| \tag{7.8}$$

where r and v_r show spatial and momentum integration and σ is the scattering cross-section. Moreover, $f_{e,g}$ indicate the phase-space distributions of the particles and $\boldsymbol{r}$ and $\boldsymbol{p}_{e,g}$ indicate the position and momentum of the atoms. The mass of each atom is denoted m and is the same for both species.

To perform these momentum integrations, we need to transform into centre-of-mass coordinates. This simply involves introducing the centre-of-mass velocity $\boldsymbol{v}_0 = (m\boldsymbol{v}_e + m\boldsymbol{v}_g)/(2m)$, the total mass $M = 2m$, the relative velocity $\boldsymbol{v}_r = \boldsymbol{v}_e - \boldsymbol{v}_g$ and in the reduced mass μ (which in our case is equal to $m^2/2m = m/2$ as the mass of each species is identical).

Now suppose the atoms are trapped in a harmonic potential with cylindrical symmetry:

$$U_i(\mathbf{r}) = \frac{1}{2}\left(\omega_{rad,i}^2(x^2+y^2) + \omega_{ax,i}^2 z^2\right) \tag{7.9}$$

Each single component is assumed to be in thermal equilibrium. The phase-space distribution of each species is assumed to be given by

$$f_i(\mathbf{r},\mathbf{p})T = n_{0,i}\Lambda_i^3 \exp\left(\frac{-p_i^2}{2m_i k_B T_i}\right)\exp\left(\frac{-U_i(\mathbf{r})}{k_B T_i}\right), \tag{7.10}$$

where $\Lambda_i = \left(\frac{2\pi\hbar^2}{m_i k_B T_i}\right)$ and $n_{0,i} = \left(\frac{m_i}{2\pi k_B T_i}\right)^{3/2} \omega_{rad,i}^2 \omega_{ax,i}$ is the peak density: the local density is given by

$$n_i(\mathbf{r}) = \int d^3p \frac{f_i(\mathbf{r},\mathbf{p})}{(2\pi\hbar)^3}. \tag{7.11}$$

We can now integrate equation (7.8) to produce the total number of collisions per unit time:

$$\Gamma_{eg} = \sigma_{eg}\frac{N_e N_g}{V_e g}\sqrt{\frac{8k_B}{\pi}\left(\frac{T_e}{m} + \frac{T_g}{m}\right)} \tag{7.12}$$

This can be simplified further by noting that $\sqrt{\frac{8k_B}{\pi}\left(\frac{T_e}{m} + \frac{T_g}{m}\right)}$ is the mean thermal velocity,

$\bar{v}$, to give:

$$\Gamma_{eg} = \sigma_{eg}\frac{N_e N_g}{V_{eg}}\bar{v} \tag{7.13}$$

where V_{eg} is a measure of the spatial overlap of the two clouds,

$$\begin{aligned} V_{eg} &= N_e N_g \left(\int d^3 r n_e(\mathbf{r}) n_g(\mathbf{r}) \right)^{-1} & (7.14) \\ &= \left(\frac{2\pi k_B \left(T_e + \frac{\alpha_e T_g}{\alpha_g} \right)}{m_e} \right)^{3/2} \frac{1}{\omega_{rad,e}^2 \omega_{ax,e}}. & (7.15) \end{aligned}$$

This can be simplified further by noting that $\sqrt{\frac{8k_B}{\pi}\left(\frac{T_e}{m}+\frac{T_g}{m}\right)}$ is the mean thermal relative velocity $\bar{v}$: thus

$$\Gamma_{eg} = \sigma_{eg}\frac{N_e N_g}{V_{eg}}\bar{v}. \tag{7.16}$$

The thermalisation time is dictated by the temperature difference between the two species[32,33] ($\Delta T = T_e - T_g$):

$$\tau^{-1} = \frac{d(\Delta T)}{\Delta T dt} = \frac{\Gamma_{eg}\xi}{3}\frac{N_e + N_g}{N_e N_g} \tag{7.17}$$

where ξ is a reduction factor and is equal to $4m_e m_g/(m_e + m_g)^2$ (for our experiment $\xi = 1$ as the mass of the constituent particles is identical). An average of $3/\xi$ collisions per atom is needed for thermalisation, and therefore for equal mass atoms 3 collisions are required[182].

Equations (7.10) and (7.17) can now be combined to obtain an expression for the thermalisation time[181]:

$$\tau^{-1} = \sigma_{eg}\frac{N_e + N_g}{3V_{eg}}\sqrt{\frac{8k_B}{\pi}\left(\frac{T_e + T_g}{m}\right)} \tag{7.18}$$

where σ_{eg} is the total elastic cross-section, N_e and N_g are the number of trapped metastable and ground state atoms per lattice sites respectively, V_{eg} is the spatial overlap of the two atomic clouds, T_e and T_g are the metastable and ground state temperatures and m is the atomic mass.

The thermalisation time obtained from the data in figure 7.6 is put into equation along with the initial temperatures and atom numbers. In doing so an approximate total elastic cross-section of $(6 \pm 4) \times 10^{-11}$ cm^2 was calculated. This is larger than the total cross-section obtained from collisions between the metastable atoms and background argon gas collisions at room temperature and is roughly consistent with calculations of the elastic cross section of the nearby ($4s'[1/2]_0$) metastable state with ground state argon as function of collision energy[175].

7.4.2 Parametric loss spectroscopy

Introduction and theory

As we have already discussed in section 6.5.5, parametric resonances are a powerful tool in characterising the potential well depths of a trap. Indeed, in far-off resonance traps where the optical scattering rates are extremely low, parametric heating due to laser instabilities can be the prime reason for heating within the trap. Due to this, much theoretical and experimental work has been performed in modelling and understanding this phenomenon[116,117,183].

Simply stated, fluctuations in a trapping beam's intensity or central position can heat atoms trapped within it. This process is resonantly enhanced at frequencies near the trap frequency (i.e. an atom oscillating within the trap will gain an amount of energy on every oscillation). While this ordinarily leads to heating, previous work has exploited the anharmonicity of a trap (where higher energy atoms oscillate more slowly) to preferentially heat the more energetic atoms out of the trap and therefore cool the overall sample. This is known as selective parametric cooling[169].

For the work presented in this thesis, parametric heating resonances are used to identify the presence of a "dark" co-trapped species. By co-trapping metastable atoms and ground state atoms together, we have already seen in section 7.4.1 that intra-trap collisions between the colder ground-state atoms and metastable atoms lead to an additional loss channel for the metastable species. This is attributed to a sympathetic cooling of the metastable atoms which therefore compresses them and leads to an increase in Penning losses due to the higher metastable density. By parametrically heating the ground state atoms out of the trap soon after loading, the metastable lifetime should therefore be increased. In doing so, we should map out a parametric spectrum for not only metastable atoms, but also ground state ones. A peak (in metastable number) should be present when ground state atoms are ejected from the trap, and a conventional dip when metastable atoms are heated.

To model the parametric heating process, we first should note that an atom of mass M trapped in a red-detuned FORT (of constant trapping intensity) has a Hamiltonian of the form:

$$H = \frac{P^2}{2M} + V_{\text{eff}}\left(\vec{x}\right) \tag{7.19}$$

where $V_{\text{eff}}\left(\vec{x}\right)$ is the effective potential and is given by:

$$V_{\text{eff}}\left(\vec{x}\right) = -\frac{1}{4}\alpha|\mathcal{E}\left(\vec{x}\right)|^2 = \frac{1}{2}M\omega_x^2 x^2 \tag{7.20}$$

Here, α is the atomic polarisability, $\mathcal{E}\left(\vec{x}\right)$ is the trapping field amplitude and ω_x is the mean-square trap frequency in the x-direction. If the atom is moving in the axial direction in a sinusoidal 1D lattice, then the Hamiltonian can be taken to be:

$$\begin{aligned} H_{\text{ax}} &= \frac{P_z^2}{2M} + V_0\cos^2(kz) \\ &= \frac{P_z^2}{2M} + \frac{V_0}{2}[1 + \cos(2kz)] \end{aligned} \tag{7.21}$$

which give a stationary Schrödinger equation of:

$$-\frac{\hbar^2}{2M}\frac{d^2\Phi}{dz^2} + \frac{V_0}{2}(1 + \cos(2kz))\Phi = E\Phi \tag{7.22}$$

If, however, we now allow the trapping intensity to have small fluctuations we then have the following Hamiltonian:

$$H = \frac{P^2}{2M} + \frac{1}{2}M\omega_x^2[1 + \epsilon(t)]x^2 \tag{7.23}$$

where $\epsilon(t)$ is the fractional fluctuation of the trapping intensity:

$$\epsilon(t) = \frac{I(t) - I_0}{I_0} \tag{7.24}$$

Equation (7.22) has been used to classically study parametric resonances. For the case where $x(t) = x_0\cos\omega_x t$ and $\epsilon(t) = \epsilon_0\sin 2\omega_x t$ it has been proved that trapped atoms are exponentially heated with a rate constant equal to $\epsilon_0\omega_x$ (which is also equal to the width of the parametric resonance). To calculate transition rates between the trap's quantum states, we can use first-order time-dependent perturbation theory with a perturbation of the form:

$$H'(t) = \frac{1}{2}\epsilon(t)M\omega_x^2 x^2 \tag{7.25}$$

For an atom initially in state $|n\rangle$ at time $t = 0$, this additional modulation of the trapping light induces transitions to state $|m \neq\rangle n$ with an averaged rate over time interval T:

$$\begin{aligned} R_{m \leftarrow n} &= \frac{1}{T}\left|\frac{-i}{\hbar}\int_0^T dt' H'_{mn}(t')e^{i\omega_{mn}t'}\right| \\ &= \left(\frac{M\omega_x^2}{2\hbar}\right)^2 \int_{-\infty}^{\infty} d\tau e^{i\omega_{mn}\tau}\langle\epsilon(t)\epsilon(t+\tau)\rangle \left|\langle m\left|x^2\right|n\rangle\right|^2 \end{aligned} \tag{7.26}$$

Here, the correlation function for fractional fluctuations in the trapping intensity is defined to be:

$$\langle\epsilon(t)\epsilon(t+\tau)\rangle = \frac{1}{T}\int_0^T dt\epsilon(t)\epsilon(t+\tau) \tag{7.27}$$

If the trapping potential is approximately harmonic, then the transition rates are equal to:

$$R_{n\pm 2 \leftarrow n} = \frac{\pi\omega_x^2}{16}S_k(2\omega_x)(n+1\pm 1)(n\pm 1) \tag{7.28}$$

where $S_k(w)$ is the one-sided power spectrum of the trapping field fluctuation. This is defined as:

$$S_k(\omega) = \frac{2}{\pi}\int_0^{\infty} d\tau \cos\omega\tau\langle\epsilon(t)\epsilon(t+\tau)\rangle \tag{7.29}$$

and this is defined such that:

$$\int_0^{\infty} d\omega S_k(\omega) = \int_0^{\infty} df S_k(f) = \langle\epsilon^2(t)\rangle = \epsilon_0^2 \tag{7.30}$$

where ϵ_0 is the root-mean-square fractional modulation on the trapping intensity, and ω is simply equal to $2\pi f$ (where f is in Hz).

By giving the atoms a probability, $P(n,t)$, of being in state $|n\rangle$ at a time t, then the average heating rate is given by:

$$\begin{aligned}\langle \dot{E}(t) \rangle &= \sum_n P(n,t) 2\hbar\omega_x (R_{n+2\leftarrow n} - R_{n-2\leftarrow n}) \\ &= \frac{\pi}{2}\omega_x^2 S_k(2\omega_x)\langle E_x(t)\rangle\end{aligned} \tag{7.31}$$

where the average energy of an atom,$\langle E_x(t)\rangle$ is equal to $\sum_n P(n,t)(n+1/2)\hbar\omega_x$. The main result from equation (7.31) is that the average atomic energy increases exponentially, and is of the form:

$$\langle \dot{E}_x \rangle = \Gamma_x \langle E_x \rangle \tag{7.32}$$

Here, Γ_x is the rate constant (in units of sec^{-1}) of the atomic heating and is equal to:

$$\Gamma_x = \frac{1}{T_x}\pi^2 f_x^2 S_k(2f_x) \tag{7.33}$$

where f_x is the trap frequency (in Hz) in the x-direction and T_x is the time taken (in sec) to increase the average energy by a factor of e.

More generally, this process can be similarly derived both for fluctuations in the position of the trap centre[117] and for frequencies of the form $2\omega_0/n$[183] but a full explanation is beyond the scope of this thesis. As can be seen, the heating is dependent on the trapping intensity being driven at a frequency of $2\omega_0$ and this thus displays the parametric nature of the process.

Results

To verify that we have trapped ground state atoms we co-trap metastable and ground-state atoms and artificially modulate the trap intensity over the trap frequencies for both species. As the polarisability of metastable atoms is ~40 times larger than for ground-state atoms, each species has a different trap frequency. If the trap is modulated at the ground state trap frequency, then ground state atoms will be ejected from the trap and they therefore will not have a chance to collide with the metastable atoms. As was described in section 6.5.5, these collisions lead to a sympathetic cooling of the metastable atoms and therefore compress them within the trap. This compression leads to a higher density for the metastable atoms, and therefore leads to enhanced Penning losses. By parametrically heating ground state atoms out of the trap, the metastable trap lifetime should be lengthened.

In doing so, we can detect the "dark" trapped ground-state species that would otherwise require a REMPI process to be detected. By modulating the trap intensity over a range of frequencies, we should also be able to detect the ground-state trap frequencies and therefore use them to compare the polarisability of the ground state atoms with the metastable species.

For a harmonic trap, the frequency of modulation at which significant heating and trap loss occurs is equal to $2\omega/n$, where ω is the trap frequency and n is an integer. The axial trap frequency in a harmonic trap is given by

$$\omega_z = 2\pi f_z = \sqrt{2\frac{U_0 k^2}{m}}, \tag{7.34}$$

where m is the mass of the trapped particle, U_0 is the well depth and $k = 2\pi/\lambda$. U_0 is related to the polarisability by $U_0 = \frac{2\alpha}{\epsilon_0 c} I_c$, where I_c is the one-way circulating peak intensity. As the lattice wells are only harmonic for the lowest energy atoms the parametric heating spectrum is broadened. In addition, as we load both ground and excited state atoms into the trap we expect to observe trap frequencies for both states. However, since we only observe the metastable state, the loss for the ground state has a different signature from that of loss from the metastable state. This is because if ground state atoms are ejected from the trap the lifetime of the metastable atoms in the trap is increased since there are fewer collisions between the ground and metastable atoms. Instead of a decrease in observed fluorescence when modulated on a parametric heating resonance an increase is observed. When the trap frequency of the metastable atoms is reached, we observe the conventional parametric heating loss spectrum and a decrease in fluorescence.

The trap frequencies for the metastable atoms were determined by applying a sinusoidal intensity modulation to the light coupled into the build-up cavity using an acousto-optic modulator. The well depth was modulated by 10% for frequencies up to 4 MHz for 100 ms. The trap was then turned off and the remaining metastable atoms were imaged on an EMCCD camera following illumination by the MOT beams. This provided a parametric loss spectrum as shown in figure 7.7 a) and b).

Fig. 7.7 a) shows two troughs corresponding to modulation at approximately the radial trap frequency and at twice this value, 1.7 kHz and 3.0 kHz respectively. Fig. 7.7 b) show two higher frequency peaks corresponding to modulation at the axial trap

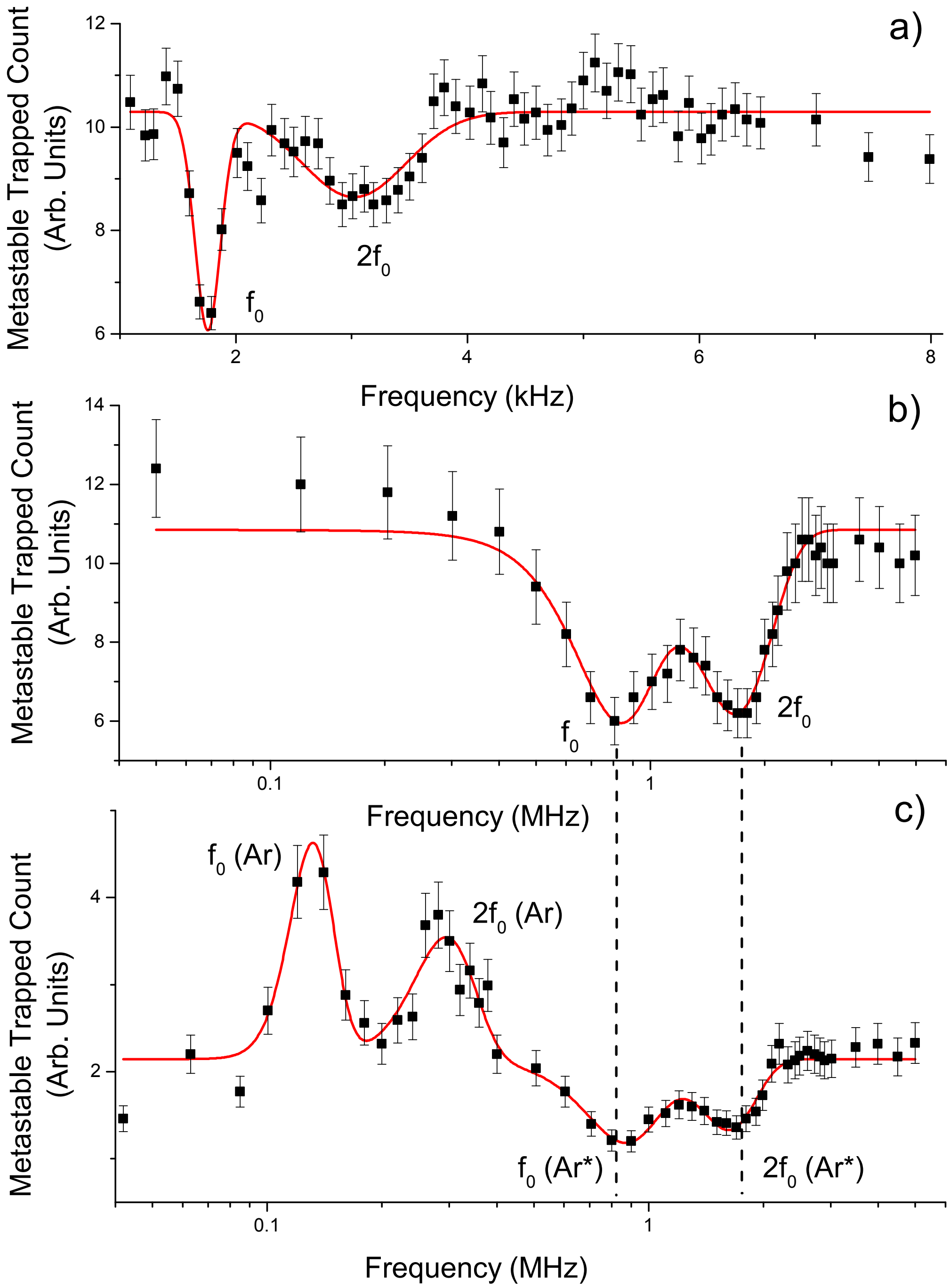

Figure 7.7: Graph displaying parametric resonances of Ar and Ar* atoms observed in the dipole trap. a) shows two troughs due to metastable atoms being parametrically heated out of the trap at the radial trap frequencies. b) shows the same, but for the axial trap frequencies. c) shows the axial trap frequencies when we co-trap ground state and metastable atoms together. Here, the dips corresponding to the losses are the same case as in b). The peaks are due to ground state atoms being ejected out of the trap which reduces the collisional loss with metastable atoms. The error bars again originate from fluctuations of 20 averaged fluorescence images.

frequency and approximately twice this value along the lattice at 820 kHz and 1.67 MHz respectively. These four frequencies correspond to a intra-cavity intensity of $\sim 7 \times 10^9$ W/m^2 using a polarisability of 5.51×10^{-39} Cm^2/V[184] in equation 7.34. To measure the ground state frequencies we quenched 80% of the metastables loaded into the trap. When the parametric loss measurements are repeated we observe four well-defined peaks as shown in figure c). Two of these peaks, at frequencies of 130 kHz (the axial trap frequency for ground state argon) and 300 kHz, correspond to the reduced loss of metastable atoms as ground state argon has been ejected from the trap. These frequencies correspond to the trap frequency and twice the trap frequency. The other two peaks at 890 kHz and 1.75 MHz show increased loss due to direct conventional parametric excitation of metastable argon out of the trap and are consistent with figure b).

We use these trap frequencies to determine the ratio of the polarisability of metastable to ground state argon, α_{ar*}/α_{ar}. Using both parametric resonances at f_z and $2f_z$ for both species, we calculate the α_{ar*}/α_{ar} ratio to be 40±6. As the trap light is far from any resonance the polarisability of the ground state should be well approximated by its static value given by 1.83×10^{-40} Cm^2/V[185]. However, the metastable state polarisability is likely to be larger because it will be enhanced by the trapping light at 1064 nm. We determine this polarisability by using the measured polarisability ratio and the assumption that the ground state value is well approximated by its static value. This gives a metastable polarisability of $(7.3\pm1.1)\times10^{-39}$ Cm^2/V, and as expected, this value is larger than the static polarisability given by 5.51×10^{-39} Cm^2/V.

Moreover, these trap frequencies can be used to accurately ascertain the well depths for both metastable and ground state atoms (by using equation (7.34)). In doing so we calculate a metastable well depth of 3 mK, and a ground state well depth of 80 μK.

7.5 Conclusions

We have trapped ground state argon atoms in an optical dipole trap and detected them using a parametric heating process. In contrast to typical parametric loss spectroscopy we detect the presence of ground state atoms in the trap by observing a reduced loss of co-trapped metastable argon. Using this method we have also measured the metastable to ground state polarisability ratio and from this the polarisability of the metastable state. By co-trapping both species we have also measured the one-body loss coefficient and the total elastic cross section of metastable argon by background ground state argon collisions. We have also determined the two body loss coefficient for the metastable state in the absence of light assisted collisions. Measurements of the increased loss of metastable atoms at both ultra-cold temperatures and with background room-temperature collisions were made.

Since our trap is designed for co-trapping molecules and atoms, the parametric heating method will allow us to detect trapped molecules which, like ground state argon, often have transitions in the UV and VUV where laser sources are not readily available. In addition, by tuning slightly away from a parametric resonance we can in principle perform forced evaporation by selectively removing any hot trapped atoms or molecules[169]. We note that although the metastable state density is always limited by Penning and associative losses the ground state is not. This may allow us in future to increase the density of ground state atoms well above 10^{10} cm^{-3}, which is important for sympathetic cooling using ground state argon or other laser cooled noble gas atoms.

Future work could include directly detecting ground state atoms by using a 3 + 1 resonantly-enhanced multi-photon ionisation (REMPI) process at 261.27 nm[171]. This would allow us to accurately ascertain the amount of trapped ground state atoms and monitor their lifetime when co-trapped with metastable atoms. We could therefore determine the total elastic cross-section of a ground-state collision with metastable atoms more accurately. Moreover, by using a REMPI process we would not have to simultaneously trap both metastable and ground state atoms to detect the ground state atoms. We could therefore develop methods to continuously load and accumulate ground state atoms into the trap and obtain far higher densities which would be applicable for sympathetic cooling.

7.5.1 Prospects for sympathetic cooling

The work presented in this chapter has displayed a method for the dipole trapping of ground-state argon. The ability to produce a trapped source of ultracold inert atoms has immediate implications for the sympathetic cooling of molecules (the original motivation for this work). If a molecular species is slowed (by Zeeman, Stark or optical Stark deceleration) then molecules can be feasibly loaded into the trap. By co-trapping molecules with ultracold inert atoms, thermalising collisions are predicted to cool decelerated molecules to ultracold temperatures within a timescale of several seconds.

While the attainable well depths of molecules may not be feasible for the current cavity (which could produce a well depth of the order of ~1 mK for Benzene and molecular Hydrogen), a higher finesse cavity could produce a larger power build-up and produce molecular well depths in the 10-100 mK range. This would be sufficient to trap a significant fraction of a slowed molecular beam.

Polarisabilities	**Cm^2V^{-1}**
Ground-state argon	1.826×10^{-40}
Metastable argon	47.9×10^{-40}
Benzene (C_6H_6)	11.6×10^{-40}
Molecular hydrogen (H_2)	5.19×10^{-40}

Table 7.3: Polarisabilities of both metastable and ground state argon along with benzene and molecular hydrogen.

Table 7.3 shows the polarisabilities of both argon species, benzene and molecular hydrogen. Simulations of Ar-H_2 and Ar-C_6H_6 interactions have previously been carried out[85] to assess the efficiency of a sympathetic cooling between the two species. During these simulations, typical initial atomic and molecular density and temperature conditions were considered and final temperatures of 330 ± 30 μK and 600 ± 100 μK were calculated for molecular hydrogen and benzene respectively.

These simulations, however, were considered for when the overall temperature of the ground state atoms was raised by the initially warmer molecular species (as they thermalise). However, the work presented in this chapter has raised the prospect of a sympathetic evaporation. In such a scheme, the potential well depths for ground state argon will be lower than those for the molecules (due to the polarisability differences). For example, the polarisability of Benzene is ~6 times higher than that of ground state argon. If a dipole trap produces a well depth of 6 mK for Benzene, then the well depth for ground state argon will be ~1 mK.

If an energetic Benzene molecule then collides with an argon atom, the argon atom will (more often than not) be ejected from the trap and carry away kinetic energy from the Benzene molecule. If ground state atom atoms could be continuously accumulated in the dipole trap then the lost ground state atoms could be replaced by others. This would quickly lead to a sympathetic cooling of the benzene molecules. As the temperature of the benzene molecules approaches 1 mK, however, evaporation of the ground state atoms reduces. At this point, the well depths (for both species) could be reduced thereby initiating more evaporation and a further cooling. In this way, molecules could be cooled to close to the initial temperature of the ground state argon atoms. This cooling is analogous to evaporative cooling, except without the loss of any of the molecular species.

A crucial part of this scheme would be to continuously accumulate ground state atoms within the trap to replace those that are being evaporated out. This could be feasibly done with a large magneto-optical trap, with the dipole trap beam through the centre of the trap. While the dipole trap beam will Stark shift the MOT beams out of resonance in the centre of the MOT, a MOT cloud will still be present around the trap and atoms will be dissipatively cooled within the trap. If a quench beam was also aligned through the centre of the atomic cloud, then the metastable atoms within the trap could be optically pumped to the ground state. As the Stark shift of the trap is large, this quench beam could be tailored such that only the coldest metastable atoms are quenched to the ground state. In this way, ground state atoms could be continuously loaded into the trap and used for sympathetic cooling (and evaporation) of molecules.

Chapter 8

Conclusions

8.1 Summary of experiments performed

8.1.1 Metastable argon magneto-optical trap

The early portion of this thesis was dedicated to the description and characterisation of a metastable argon magneto-optical trap. Cooling had to be performed in the 4s$[3/2]_2$ metastable state as the cooling transitions in the absolute ground state are at ultra-violet wavelengths, where laser sources are not readily available. An RF discharge was therefore used to excite a portion of ground-state argon atoms up to the metastable state, at an efficiency of $N_{ar}/N_{ar^*} = 10^5$. The metastable atoms were then slowed using a Zeeman slower and captured within a magneto-optical trap (MOT). Cooling was performed on the 4s$[3/2]_2$ to 4p$[5/2]_3$ transitions and MOT temperatures of 80 μK were achieved.

The cooling beams were locked onto frequency by using a technique that utilises magnetic dichroism within the RF discharge[111]. A "master" laser was locked (by creating a feedback loop with the laser current) onto the cooling frequency and used to injection lock[109,110] a "slave laser" to boost the overall power such that the amount is sufficient for all cooling beams.

The vacuum system consisted of four turbo-molecular pumps which were backed by scroll pumps. Pressures down to $\sim 3 \times 10^{-9}$ mbar were measured by using an ion gauge. Unfortunately the turbo-pumps created many undesirable vibrations which manifested themselves in fluctuations in laser frequencies. Ion pumps would have been preferable to use but are generally inefficient for noble gases.

Between 10^5 and 10^6 atoms were generally cooled in the MOT, and at densities of up to 10^{10} /cm^3. Both fluorescence and absorption imaging was performed to calculate these numbers. The lifetime of the MOT was generally of the order of 200 ms, and was primarily limited due to Penning ionisation. A two-body loss coefficient was calculated (albeit in the presence of near-resonant light) from this lifetime curve.

8.1.2 CO_2 laser dipole trap

The atomic cloud that was cooled in the MOT was then loaded into a dipole trap simply formed by the focussed beam of a CO_2 laser at a far-detuned wavelength of 10.6 μm. The trap was aligned was carefully characterising the position and width of the focus by using a knife-edge technique. A minimum waist of 110 μm was measured, which created an expected well depth of 240 μK. The loading procedure consisted firstly of loading the MOT and then a brief (5 ms) optical molasses phase. After this period all MOT cooling beams were switched off and the atoms were confined within the focus of the beam.

Unfortunately, the trap lifetimes were limited to only 20 ms and this was not due to Penning ionisation but instead attributed to parametric heating out of the trap. A fast Fourier transform of the MOT master laser beam frequency was taken, with large resonances at both 1.4 and 2.2 kHz. These frequencies are due to vibrations from the turbo-molecular pumps being coupled onto the optical table. The 1.4 kHz resonance in particular was extremely close to twice the radial trap frequency (at 1.27 kHz). Due to this, we expect atoms to be exponentially parametrically heated out of the trap and significantly limit the attainable lifetime.

Although experimental constraints meant that this lifetime limitation could not be resolved, the CO_2 laser trap provided a valuable test-bed for the dipole trapping of metastable argon atoms.

8.1.3 Optical cavity trap

An optical cavity was designed to create deep traps for not only metastable argon, but also ground state argon (whose polarisability is 40 times less than metastable argon) and for molecules in sympathetic cooling experiments. While the cavity finesse of 2,000 was less than originally designed it still proved sufficient to provide a well depths of up 11 mK for metastable argon.

A variant of the Pound-Drever-Hall technique[126,127] was used to lock the optical cavity on resonance. Here, two beams were used: a weak beam to lock the cavity by creating a feedback loop with the cavity piezo, and a strong beam of orthogonal polarisation which was used for trapping. As the two beams were of orthogonal polarisations, they could be separated by using high-quality polarisation optics. By using an acousto-optic modulator in the path of the strong beam, the trap could be rapidly modulated in both frequency and intensity without effecting the locking of the weak beam. By doing this, we could not only use the strong beam AOM as a type of “noise-eater” by removing intensity fluctuations of the trap, but also use it to artificially parametrically heat atoms out of the trap and calculate trap frequencies as a result.

Without modulating the strong beam intensity, lifetimes were again limited by parametric heating to 20 ms. However, with high bandwidth feedback lifetimes of between 70 and 300 ms could be achieved (depending on the trapped atom density). Moreover, the two-beam locking scheme allowed the intra-trap intensity to be slowly ramped up for more efficient loading (up to 50% of the MOT) and for more dissipative cooling within the lattice. The intra-trap cavity field could also be rapidly switched off, allowing time-of-flight temperature measurements to be performed and the trapped atom temperature was determined to be 260 μK.

The effect of the high intensities on the cavity mirrors was also characterised. As the intra-cavity intensity increased, the mirrors’ radius of curvature increased at a rate of 116 ± 10 mm/(MW/cm^2). This thermal flexing of the mirrors was enough to perturb the mode-matching into the cavity. However, as it was not necessary to keep the trapping cavity field on for long consecutive periods this did not negatively impact trapping.

8.1.4 Ground state trapping

Trapped metastable atoms were optically quenched down to the ground state by a laser operating at 801.4 nm. Although the ground state atoms could not be directly probed, we detect them by observing the collisional loss of co-trapped metastable argon atoms using a new type of parametric loss spectroscopy.

Two lifetime curves were taken: one where only metastable atoms were loaded into the cavity lattice and one where both ground state and metastable atoms were loaded. By modelling the decay of the case where only metastables were loaded we obtained a one-body loss coefficient (due to background collisions) of 1.3 ± 0.1 s^{-1} and a two-body loss coefficient (due to Penning ionisation) of $(3.3\pm0.8)\times10^{-10}$ cm^{3}s^{-1}.

When both metastable and ground state atoms were loaded into the trap an additional loss channel for metastable atoms was induced. This was attributed to the trapped ground state atoms being colder than the metastable atoms (as the ground state well depth was lower) and thermalising elastic collisions between the two species leading to a cooling of the metastable atoms. Due to this cooling, the metastable atoms were compressed within the lattice leading to a higher average density. From this we modelled this additional loss channel and obtained an approximate total elastic cross-section of $\sim 6\times10^{-11}$ cm^2, the first measurement of its kind at ultracold temperatures.

Moreover, trap frequencies of both ground state and metastable atoms were determined by modulating the intra-cavity trapping intensity (when metastable and ground state atoms were co-trapped). When the trap frequencies for ground state atoms were modulated, a peak in metastable atom number was noted. This was due to the ground state atoms being parametrically heated out of the trap and thereby not having a chance to collide with and therefore cool the co-trapped metastable atoms. A reduction in trapped metastable number was noted when the metastable trap frequencies was modulated. This was simply due to conventional parametric heating out of the trap. Axial trap frequencies of 140 kHz and 890 kHz were noted for the ground and metastable states respectively. This allowed to us to obtain a polarisability ratio $\alpha_{ar^*}/\alpha_{ar}$ of 40±6 and therefore a metastable polarisability of $(7.3\pm1.1)\times10^{-39}$ Cm^2/V at a wavelength of 1064 nm.

8.2 Improvements to the experiment

For sympathetic cooling experiments, thermalisation times can be of the order of several seconds[75,84,85,164]. To trap ground-state argon (or molecules) for this period of time would require a lower vacuum pressure. This could either by achieved by reducing the gas load onto the science chamber or by using a double-MOT system. One method of reducing the gas load would be to magnetically guide[186] the metastable atoms to the science chamber. By doing this, the ground state atoms (that make up the majority of the atomic beam) would not be guided and therefore would not reach the science chamber. An alternative method would be to use a two-dimensional magneto-optical trap[187] to guide a slow beam of cold metastable atoms. Moreover, efficient transfer (~80%) in a double-MOT system[188] has previously been demonstrated. In such a system, the MOT would be loaded in the usual fashion and a "push" beam used to transfer the atoms to a separate vacuum chamber.

This chamber would be differentially pumped, and therefore lower pressures could be readily achieved.

The optical cavity used in the work presented in this thesis would produce well depths of only ∼0.5 mK for molecular hydrogen and ∼1 mK for Benzene. Due to this, a cavity with a higher finesse (and therefore high power build-up) would have to be used to more efficiently trap a fraction of the comparatively "hot" molecules that would be used for sympathetic cooling experiments. Well depths would therefore also be higher for ground state atoms which would, in turn, also be more efficiently trapped.

8.3 Future work

It should be noted that the cooling wavelength from the $4s[3/2]_2$ to $4p[5/2]_3$ state for metastable argon is very close to the cooling transition for metastable krypton. The cooling wavelengths are 811.5 and 811.3 nm for argon and krypton respectively. Due to these wavelengths being very close to one another, the same laser system would be suitable for cooling, trapping and studying metastable krypton. Collisions between metastable and ground-state krypton could similarly be studied, and estimates of the total elastic cross-sections attained.

8.3.1 Spin polarisation study

Spin polarisation to the $|J = 2, m_J = 2\rangle$ "stretched state" has been studied for all of the noble gases except for ^{3}He* and ^{40}Ar*. To achieve spin polarisation of the atomic cloud requires circularly polarised resonant light, and a weak magnetic field. Table 8.1 below compares the inelastic two-body loss rates from both unpolarised and spin polarised atomic samples of all the metastable noble gases. As can be seen, spin polarisation dramatically suppresses Penning ionisation processes for ^{4}He* by a factor of 10^4. The effect on ^{20}Ne* and ^{22}Ne* is less dramatic, with only a ∼80 times reduction in Penning processes. No suppression is noted for ^{84}Kr* or ^{132}Xe*.

This phenomenon can be explained by noting that in any Penning process the total spin of the system should always be conserved. By spin polarising the atomic cloud the total initial spin, S_i, of the initial species (i.e. the cold metastable atoms) is equal to 2. However the maximum total resultant spin, S_f, is equal to 1. Therefore a Penning reaction is forbidden, if S is assumed to be a good quantum number. Indeed, the only way in which

	^{3}He*	^{4}He*	^{20}Ne*	^{22}Ne*	^{40}Ar*	^{84}Kr*	^{132}Xe*
Polarised loss rate (10^{-14} cm^3/s)	N/A	2 ± 1 [78]	650 ± 180 [79]	$1,200 \pm 300$ [79]	N/A	40,000 [81]	6,000 [82]
Unpolarised loss rate (10^{-11} cm^3/s)	38 ± 6 [76]	20 ± 4 [76]	50 ± 30 [77]	100^{+40}_{-50} [189]	33 ± 8 [99]	40 [81]	6 ± 2 [82]

Table 8.1: Table depicting two-body inelastic loss rates for all noble gases in their metastable states. Spin polarisation has been demonstrated to suppress Penning ionisation of ^{4}He*, ^{20}Ne* and ^{22}Ne*, but not for ^{84}Kr* or ^{132}Xe*. This phenomenon has not yet been tested for ^{40}Ar*. References are given under the loss rate values.

a Penning process can occur is via a "spin-flip" of one of the electrons. For helium, this is made possible due to a weak spin-spin dipole interaction. The spins involved in a Penning process are listed below, where one can see that the total of the initial spins is not equal to the total of the final spins.

$$\begin{array}{rcccccccccc}
 & \mathrm{Ar}^* & + & \mathrm{Ar}^* & \rightarrow & \mathrm{Ar} & + & \mathrm{Ar}^+ & + & \mathrm{e}^- \\
\text{Spin :} & s_a = 1 & & s_b = 1 & | & s_a = 0 & & s_b = \frac{1}{2} & & s_c = \frac{1}{2} \\
\text{Total spin :} & & S_i = 2 & & | & & & S_f = 1 & &
\end{array}$$

Theoretical calculations[190] predicted that Penning losses for helium would be suppressed by a factor of 10^5, while current experiments[78] have shown suppressions of 10^4. Indeed, this suppression played a key role in obtaining a Bose-Einstein condensate of metastable helium. For heavier atoms, the suppression is expected to be less dramatic as the likelihood of a "spin-flip" increases. This is primarily due to the LS coupling breaking down due to the presence of orbital angular momentum.

Experimentally this has been proven so far by observing a lessening of Penning suppression in ^{20}Ne* and ^{22}Ne*. Similar experiments for ^{84}Kr* or ^{132}Xe* have also shown no suppression whatsoever. Metastable argon has yet to be studied in this way, and it is not yet clear if spin polarisation would reduce the overall collisional loss between trapped atoms. In the future, our experiment would be suitable for identifying the result of spin polarising metastable argon and furthering our understanding of Penning collisions.

8.3.2 Sympathetic cooling

The dipole trapping of ultracold metastable argon, and the optical quenching to the ground state were milestones towards a general method for the sympathetic cooling of molecules.

Within our research group, work has been ongoing towards the optical Stark deceleration of molecules. A custom laser system has been designed such that two high intensity (10^{12} – 10^{14} Wm^{-2}) beams at 1064 nm can be created. These beams are overlapped at small angles such that they are nearly counter-propagating. The beams therefore create an optical lattice interference pattern in which molecules can be trapped.

The laser system itself consists of a Nd:YVO$_4$ microchip laser, whose frequency can be rapidly chirped by changing the cavity optical path length by applying a voltage to an intra-cavity electro-optical crystal. To suppress the intensity fluctuations caused by this modulation, the output of the microchip laser is used to injection lock a slave diode. This beam is then fed into a fibre amplifier to increase the overall power to 1 W, before being coupled into a custom-built Nd:YAG laser to create pulses at the required intensity.

By frequency-chirping one of these beams the optical lattice be made to decelerate or accelerate, thereby decelerating or accelerating any molecules or atoms trapped within the lattice. This effect has already been successfully demonstrated[68] in our system by using the optical lattice to accelerate ultracold metastable argon atoms to velocities of hundreds of metres per second while maintaining narrow velocity spreads. Currently, work towards the deceleration of molecular hydrogen is ongoing within the group.

8.3.3 Weak measurements and hybrid nanosphere cooling

In the immediate future, the magneto-optical trap described in this thesis will be used for two experiments: the first involving performing weak measurements by double slit interferometry, and the second being a hybrid optomechanical system by coupling the ultracold atoms to a levitated nanosphere.

Weak measurements have already been performed by passing an ensemble of single photons through a double-slit interferometer[191]. Here, a weak measurement is performed on each photon to obtain a small amount of information about its momentum before a strong measurement of its position is made. A similar method is planned for our system to make the first weak measurements in a matter wave system. To achieve this, atoms would first be prepared in the MOT before being spin polarised to the $|J = 2, m_J = 2\rangle$ “stretched state”. The atoms would then be guided (or allowed to fall freely) through a double slit. A superposition of the five possible m_J states can then be created by using an abrupt change in magnetic field direction. From here, the atoms then enter a stage where each atom accumulates a phase dependent on the transverse velocity (momentum). The different m_J states can then be separated by an inhomogeneous magnetic field in a Stern-Gerlach type phase and then detected on a microchannel plate and phosphor screen. This would allow a strong measurement of position.

Another branch of our group's work focusses on the trapping and cooling of levitated nanospheres[192–194]. Previous work has been achieved in coupling ultracold atoms to a micromechanical membrane in order to cool the membrane[195]. Such a system would also be applicable to couple to nanospheres, thereby cooling them.

8.3.4 Concluding remarks

This thesis has presented work towards an ultra-cold atomic source for the sympathetic cooling of molecules. By creating a cold and inert trapped atomic source, in the future we can co-trap molecules and utilise thermalising elastic collisions to cool molecules to sub-milliKelvin temperatures. Work is ongoing within the group to use optical Stark deceleration to slow molecules such that they can be trapped within an optical cavity.

Appendix A

Photographs of experiment

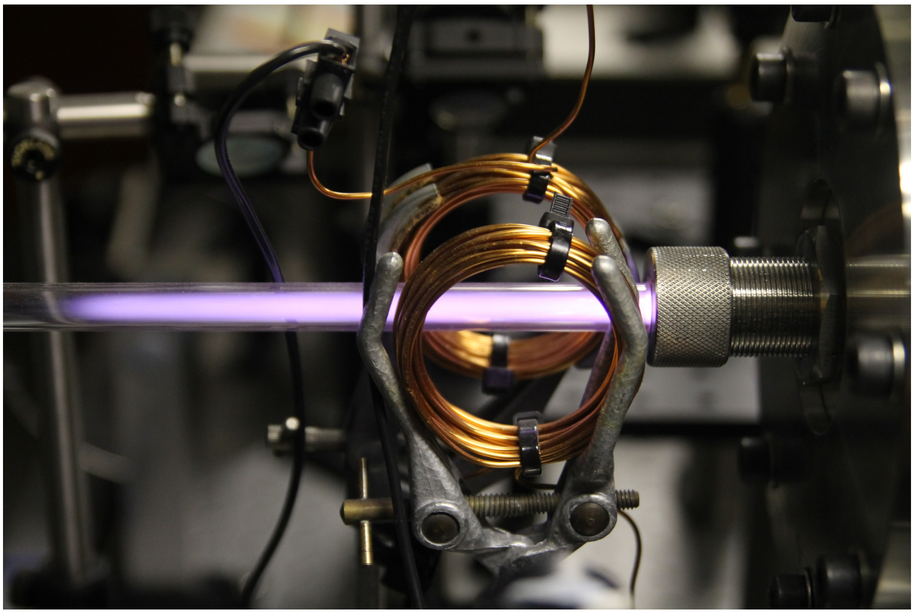

Figure A.1: Here, the RF discharge is shown in operation. The purple glow shows when the discharge is "lit" and produces metastable atoms at an efficiency of $N_{ar}/N_{ar^*} \sim 10^5$. The Helmholtz coils that are used to Zeeman split the resonance transition (necessary for locking the cooling beams) are also shown.

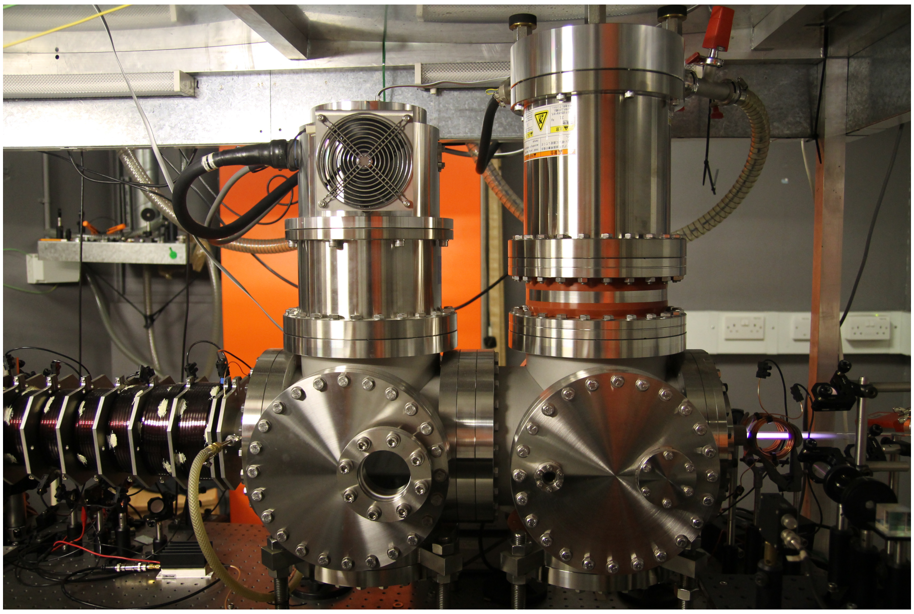

Figure A.2: The RF discharge can be seen feeding into the differentially pumped vacuum system. The two 1000 l/s turbo pumps produce pressures of $\sim 10^{-5}$ mbar in the first chamber and $\sim 10^{-5}$ mbar in the second chamber. The second chamber is then connected to the Zeeman slower.

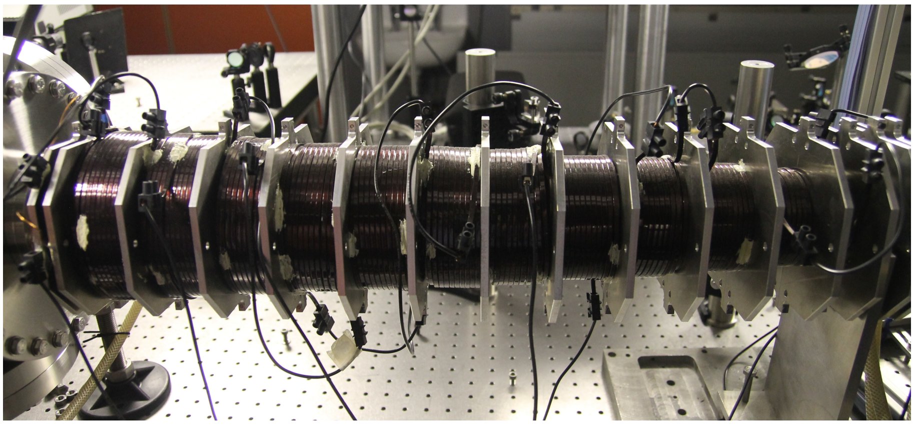

Figure A.3: Photo of the Zeeman slower constructed out of a segmented structure consisting of tapering magnetic field coils of enamelled copper wire. As there are multiple coils, this allowed straightforward tuning of the magnetic field.

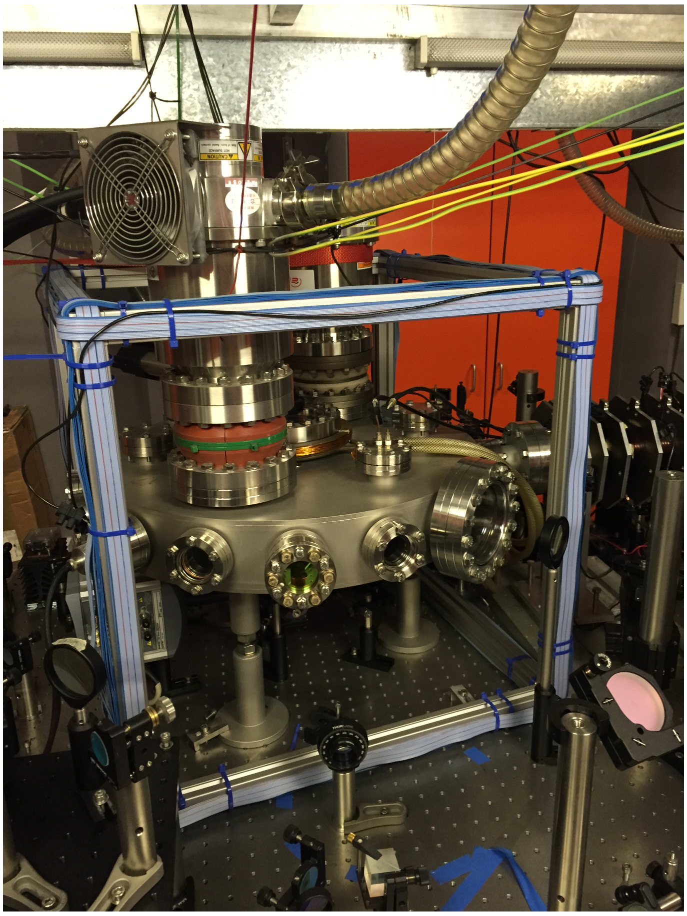

Figure A.4: Here, the science chamber is shown. The Zeeman slower feeds metastable atoms into this chamber from the right-hand side. One of the anti-Helmholtz coils can be seen on top of the science chamber (used to produce the quadrupole magnetic field for the MOT), along with the three sets of square Helmholtz compensation coils. The compensation coils allowed us to cancel out any stray magnetic fields and even move the position of the MOT cloud such that atoms could be loaded into the cavity dipole trap.

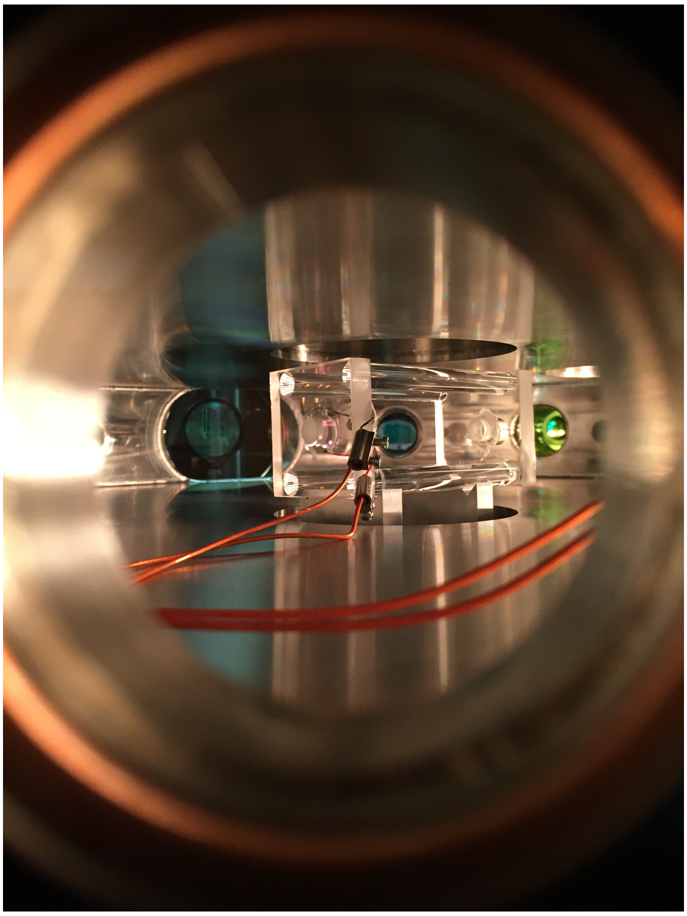

Figure A.5: Photo of cavity mounted inside the science chamber. The cavity spacer was constructed out of fused silica and was mounted on a “V-mount” inside the chamber. The wires are connected to the cavity piezo and used for cavity locking up to a bandwidth of $\sim$3 kHz.

Appendix B

Pound-Drever-Hall electronics

To produce an error signal a custom-made Pound-Drever-Hall (PDH) box (originally designed at Hamburg university) was constructed by the department's electronics technician Rafid Jawad, the electronic circuit of which is shown below:

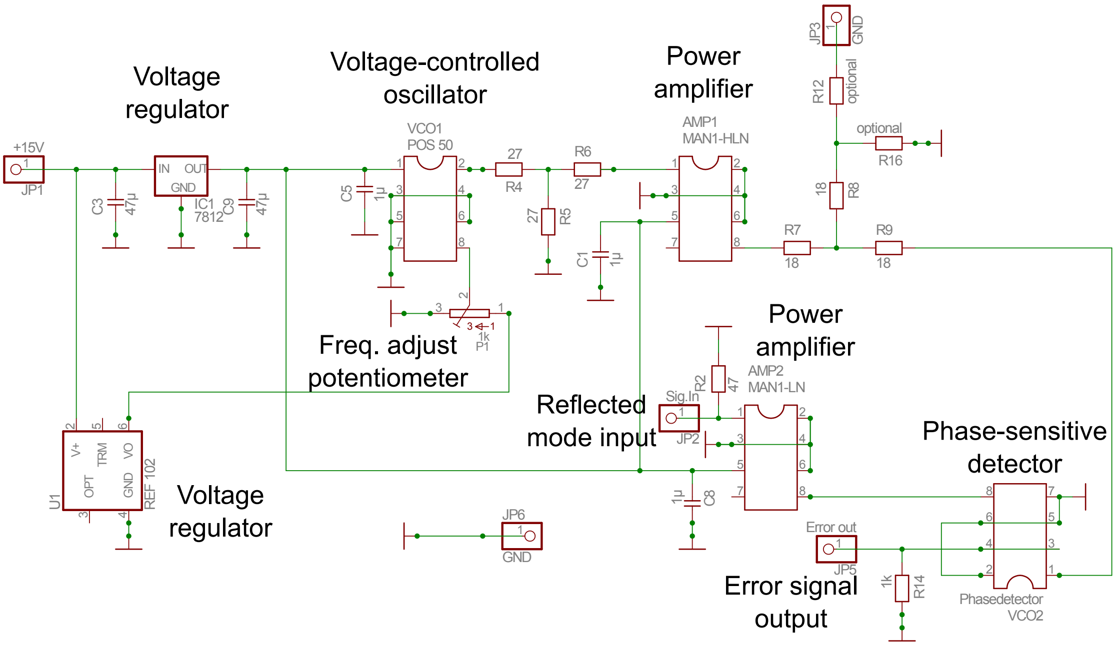

Figure B.1: Electronic schematic of the Pound-Drever-Hall box. The various components are labelled including the inputs for the reflected mode and the error signal output.

Here, a voltage-controlled oscillator first produces a sinusoidal signal at a frequency of tens of MHz. The signal is then amplified and sent across an electro-optic crystal made of lithium tantalate ($LiTaO_3$). Once the laser beam was sent through this electro-optic crystal it had the effect of phase-modulating (and therefore frequency modulating) the beam. A photodiode was then used to monitor the beat signal between the beam directly reflected from the cavity and the beam that is transmitted from the cavity. This signal is then sent to the phase-sensitive detector, which measures the phase of a certain part (the part at the modulation frequency, with the rest filtered out) of this beat pattern. This signal is then multiplied with the reference signal coming from the local oscillator to form an error signal (as derived in equation (5.20)).

Appendix C

Dual-species inelastic loss calculation

To calculate a value for the loss coefficient of a metastable and ground state collision, we need to obtain a solution of the coupled differential equations:

$$\dot{\rho}_e = -\Gamma \rho_e - \gamma_{ge}\rho_g\rho_e - \gamma_{ee}\rho_e^2 \tag{C.1}$$

$$\dot{\rho}_g = -\Gamma \rho_g - \gamma_{ge}\rho_g\rho_e \tag{C.2}$$

where ρ_e and ρ_g are the metastable and ground state densities respectively, Γ is the one-body loss coefficient and γ_{ee} and γ_{ge} are the loss coefficients during a metastable-metastable collision and ground state-metastable collision respectively.

To obtain an approximation to these equations we use the Picard-Lindelöf theorem[179,180], which shows that there is a sequence of functions $\left(\rho_e^{(n)}, \rho_g^{(n)}\right)$ that converge to the solution (ρ_e, ρ_g) of the problem. The sequence is defined as follows: taking the initial values of the densities to be $\rho_e^{(0)}$ and $\rho_g^{(0)}$, and setting $\rho_e^{(0)}(t) = \rho_e(0)$, $\rho_g^{(0)}(t) = \rho_g(0)$

$$\begin{aligned}\rho_e^{(n)}(t) = e^{-\Gamma t}\rho_e(0) - e^{-\Gamma t}\int_0^t \gamma_{ge} e^{-\Gamma s}\rho_e^{(n-1)}(s)\rho_g^{(n-1)}(s)ds \\ - e^{-\Gamma t}\int_0^t \gamma_{ee} e^{-\Gamma s}\left(\rho_e^{(n-1)}(s)\right)^2 ds\end{aligned} \tag{C.3}$$

$$\rho_g^{(n)}(t) = e^{-\Gamma t}\rho_g(0) - e^{-\Gamma t}\int_0^t \gamma_{ge} e^{-\Gamma s}\rho_e^{(n-1)}(s)\rho_g^{(n-1)}(s)ds. \tag{C.4}$$

In this way, we can obtain an approximation to the solution as closely as desired. The first-order approximation is given by:

$$\rho_e^{(1)}(t) = e^{-\Gamma t}\rho_e(0)\left[1 - \frac{1}{\Gamma}\left(1 - e^{-\Gamma t}\right)\left(\gamma_{ge}\rho_g(0) + \gamma_{ee}\rho_e(0)\right)\right] \tag{C.5}$$

and

$$\rho_g^{(1)}(t) = e^{-\Gamma t}\rho_g(0)\left[1 - \frac{\gamma_{ge}\rho_e(0)}{\Gamma}\left(1 - e^{-\Gamma t}\right)\right]. \tag{C.6}$$

The first-order fit was quite good for trapping times of less than a second, but unfortunately broke down after this. A second order approximation was therefore required, and for ρ_e is of the form:

$$\rho_e^{(2)}(t) = (\rho_e(0) - \gamma_{ge}\theta - \gamma_{ee}\Lambda)e^{-\Gamma t} \tag{C.7}$$

where

$$\begin{aligned}\frac{\theta}{\rho_e(0)\rho_g(0)} &= \left(1 - \frac{1}{\Gamma}(\gamma_{ge}\rho_g(0) + \gamma_{ee}\rho_e(0))\right)\left(1 - \frac{\gamma_{ge}\rho_e(0)}{\Gamma}\right)\frac{\left(1 - e^{-\Gamma t}\right)}{\Gamma} \\ &+ \left[\left(\frac{\gamma_{ge}\rho_g(0) + \gamma_{ee}\rho_e(0)}{\Gamma}\right)\left(1 - \frac{\gamma_{ge}\rho_e(0)}{\Gamma}\right)\right. \\ &+ \left.\left(1 - \frac{1}{\Gamma}\right)(\gamma_{ge}\rho_g(0) + \gamma_{ee}\rho_e(0))\frac{\gamma_{ge}\rho_e(0)}{\Gamma}\right]\frac{\left(1 - e^{-2\Gamma t}\right)}{2\Gamma} \\ &+ \left(\frac{\gamma_{ge}\rho_g(0) + \gamma_{ee}\rho_e(0)}{\Gamma}\right)\left(\frac{\gamma_{ge}\rho_e(0)}{\Gamma}\right)\frac{\left(1 - e^{-3\Gamma t}\right)}{3\Gamma}\end{aligned} \tag{C.8}$$

and

$$\begin{aligned}\frac{\Lambda}{(\rho_e(0))^2} &= \left(1 - \frac{(\gamma_{ge}\rho_g(0) + \gamma_{ee}\rho_e(0))}{\Gamma}\right)^2\frac{\left(1 - e^{-\Gamma t}\right)}{\Gamma} \\ &+ (\gamma_{ge}\rho_g(0) + \gamma_{ee}\rho_e(0))\left(1 - \frac{(\gamma_{ge}\rho_g(0) + \gamma_{ee}\rho_e(0))}{\Gamma}\right)\frac{\left(1 - e^{-2\Gamma t}\right)}{\Gamma^2} \\ &+ (\gamma_{ge}\rho_g(0) + \gamma_{ee}\rho_e(0))^2\frac{\left(1 - e^{-3\Gamma t}\right)}{3\Gamma^3}\end{aligned} \tag{C.9}$$

The second-order approximation in equation (C.7) gave a much better fit to the lower curve (where both metastable and ground state atoms are trapped) in figure 7.4. This allowed us to obtain a value for γ_{ge} of $(9 \pm 6) \times 10^{-10}$ cm^{3}s^{-1}.

Bibliography

1. Hänsch, T. W. & Schawlow, A. L. Cooling of gases by laser radiation. *Optics Communications* **13**, 68–69 (1975).
2. Phillips, W. D. & Metcalf, H. Laser deceleration of an atomic beam. *Physical Review Letters* **48**, 596 (1982).
3. Ertmer, W., Blatt, R., Hall, J. & Zhu, M. Laser manipulation of atomic beam velocities: Demonstration of stopped atoms and velocity reversal. *Physical Review Letters* **54**, 996–999 (1985).
4. Neuhauser, W., Hohenstatt, M., Toschek, P. & Dehmelt, H. Optical-sideband cooling of visible atom cloud confined in parabolic well. *Physical Review Letters* **41**, 233–236 (1978).
5. Chu, S., Hollberg, L., Bjorkholm, J. E., Cable, A. & Ashkin, A. Three-dimensional viscous confinement and cooling of atoms by resonance radiation pressure. *Physical Review Letters* **55**, 48 (1985).
6. Raab, E., Prentiss, M., Cable, A., Chu, S. & Pritchard, D. E. Trapping of neutral sodium atoms with radiation pressure. *Physical Review Letters* **59**, 2631 (1987).
7. Dalibard, J. & Cohen-Tannoudji, C. Laser cooling below the Doppler limit by polarization gradients: simple theoretical models. *JOSA B* **6**, 2023–2045 (1989).
8. Ungar, P. J., Weiss, D. S., Riis, E. & Chu, S. Optical molasses and multilevel atoms: theory. *JOSA B* **6**, 2058–2071 (1989).
9. Davis, K. B., Mewes, M.-O., Joffe, M. A., Andrews, M. R. & Ketterle, W. Evaporative cooling of sodium atoms. *Physical Review Letters* **74**, 5202 (1995).

10. Anderson, M. H., Ensher, J. R., Matthews, M. R., Wieman, C. E. & Cornell, E. A. Observation of Bose-Einstein condensation in a dilute atomic vapor. *Science* **269**, 198–201 (1995).

11. Bjorkholm, J., Freeman, R., Ashkin, A. & Pearson, D. Observation of focusing of neutral atoms by the dipole forces of resonance-radiation pressure. *Physical Review Letters* **41**, 1361 (1978).

12. Chu, S., Bjorkholm, J., Ashkin, A. & Cable, A. Experimental observation of optically trapped atoms. *Physical Review Letters* **57**, 314 (1986).

13. Miller, J., Cline, R. & Heinzen, D. Far-off-resonance optical trapping of atoms. *Physical Review A* **47**, R4567 (1993).

14. Takekoshi, T., Yeh, J. & Knize, R. Quasi-electrostatic trap for neutral atoms. *Optics Communications* **114**, 421–424 (1995).

15. O'Hara, K. *et al.* Ultrastable CO_2 laser trapping of lithium fermions. *Physical Review Letters* **82**, 4204 (1999).

16. Thomas, J., Kelly, M., Monchalin, J.-P., Kurnit, N. & Javan, A. Stable CO_2 and N_2O laser design. *Review of Scientific Instruments* **51**, 240–243 (2008).

17. Takekoshi, T. & Knize, R. J. CO_2 laser trap for cesium atoms. *Opt. Lett.* **21**, 77–79 (1996).

18. Takekoshi, T., Patterson, B. & Knize, R. Observation of optically trapped cold cesium molecules. *Physical Review Letters* **81**, 5105 (1998).

19. Weber, T., Herbig, J., Mark, M., Nägerl, H.-C. & Grimm, R. Bose-Einstein condensation of cesium. *Science* **299**, 232–235 (2003).

20. Takasu, Y. *et al.* Spin-singlet Bose-Einstein condensation of two-electron atoms. *Physical Review Letters* **91**, 040404 (2003).

21. Griesmaier, A., Werner, J., Hensler, S., Stuhler, J. & Pfau, T. Bose-Einstein condensation of chromium. *Physical Review Letters* **94**, 160401 (2005).

22. Stellmer, S., Tey, M. K., Huang, B., Grimm, R. & Schreck, F. Bose-Einstein condensation of strontium. *Physical Review Letters* **103**, 200401 (2009).

23. Kraft, S., Vogt, F., Appel, O., Riehle, F. & Sterr, U. Bose-Einstein Condensation of Alkaline Earth Atoms: Ca 40. *Physical Review Letters* **103**, 130401 (2009).

24. Lu, M., Burdick, N. Q., Youn, S. H. & Lev, B. L. Strongly dipolar Bose-Einstein condensate of dysprosium. *Physical Review Letters* **107**, 190401 (2011).

25. Barrett, M., Sauer, J. & Chapman, M. All-optical formation of an atomic Bose-Einstein condensate. *Physical Review Letters* **87**, 010404 (2001).

26. Granade, S., Gehm, M., O'Hara, K. & Thomas, J. All-optical production of a degenerate Fermi gas. *Physical Review Letters* **88**, 120405 (2002).

27. Herbig, J. *et al.* Preparation of a pure molecular quantum gas. *Science* **301**, 1510–1513 (2003).

28. Greiner, M., Regal, C. A. & Jin, D. S. Emergence of a molecular Bose–Einstein condensate from a Fermi gas. *Nature* **426**, 537–540 (2003).

29. Zwierlein, M. W. *et al.* Observation of Bose-Einstein condensation of molecules. *Physical Review Letters* **91**, 250401 (2003).

30. Staanum, P., Kraft, S. D., Lange, J., Wester, R. & Weidemüller, M. Experimental investigation of ultracold atom-molecule collisions. *Physical Review Letters* **96**, 023201 (2006).

31. Zahzam, N., Vogt, T., Mudrich, M., Comparat, D. & Pillet, P. Atom-molecule collisions in an optically trapped gas. *Physical Review Letters* **96**, 023202 (2006).

32. Mosk, A. *et al.* Mixture of ultracold lithium and cesium atoms in an optical dipole trap. *Applied Physics B* **73**, 791–799 (2001).

33. Mudrich, M. *et al.* Sympathetic cooling with two atomic species in an optical trap. *Physical Review Letters* **88**, 253001 (2002).

34. Shuman, E., Barry, J. & DeMille, D. Laser cooling of a diatomic molecule. *Nature* **467**, 820–823 (2010).

35. Zhelyazkova, V. *et al.* Laser cooling and slowing of CaF molecules. *Physical Review A* **89**, 053416 (2014).

36. Hummon, M. T. *et al.* 2D magneto-optical trapping of diatomic molecules. *Physical Review Letters* **110**, 143001 (2013).

37. Jochim, S. *et al.* Bose-Einstein condensation of molecules. *Science* **302**, 2101–2103 (2003).

38. Danzl, J. G. *et al.* Quantum gas of deeply bound ground state molecules. *Science* **321**, 1062–1066 (2008).

39. Ni, K.-K. *et al.* A high phase-space-density gas of polar molecules. *Science* **322**, 231–235 (2008).

40. Lett, P. *et al.* Spectroscopy of Na 2 by photoassociation of laser-cooled Na. *Physical Review Letters* **71**, 2200 (1993).

41. Nikolov, A. *et al.* Efficient production of ground-state potassium molecules at sub-mK temperatures by two-step photoassociation. *Physical Review Letters* **84**, 246 (2000).

42. Sage, J. M., Sainis, S., Bergeman, T. & DeMille, D. Optical production of ultracold polar molecules. *Physical Review Letters* **94**, 203001 (2005).

43. Deiglmayr, J. *et al.* Formation of ultracold polar molecules in the rovibrational ground state. *Physical Review Letters* **101**, 133004 (2008).

44. Van De Meerakker, S. Y., Bethlem, H. L. & Meijer, G. Taming molecular beams. *Nature Physics* **4**, 595–602 (2008).

45. Levy, D. H. Laser spectroscopy of cold gas-phase molecules. *Annual Review of Physical Chemistry* **31**, 197–225 (1980).

46. Bethlem, H. L., Berden, G. & Meijer, G. Decelerating neutral dipolar molecules. *Physical Review Letters* **83**, 1558–1561 (1999).

47. Bethlem, H. L., Berden, G., Van Roij, A. J., Crompvoets, F. M. & Meijer, G. Trapping neutral molecules in a traveling potential well. *Physical Review Letters* **84**, 5744 (2000).

48. van de Meerakker, S. Y., Bethlem, H. L., Vanhaecke, N. & Meijer, G. Manipulation and control of molecular beams. *Chemical Reviews* **112**, 4828–4878 (2012).

49. Bethlem, H. L., Crompvoets, F. M., Jongma, R. T., van de Meerakker, S. Y. & Meijer, G. Deceleration and trapping of ammonia using time-varying electric fields. *Physical Review A* **65**, 053416 (2002).

50. van de Meerakker, S. Y., Smeets, P. H., Vanhaecke, N., Jongma, R. T. & Meijer, G. Deceleration and electrostatic trapping of OH radicals. *Physical Review Letters* **94**, 023004 (2005).

51. Bochinski, J., Hudson, E. R., Lewandowski, H., Meijer, G. & Ye, J. Phase space manipulation of cold free radical OH molecules. *Physical Review Letters* **91**, 243001 (2003).

52. Hudson, E. R. *et al.* Production of cold formaldehyde molecules for study and control of chemical reaction dynamics with hydroxyl radicals. *Physical Review A* **73**, 063404 (2006).

53. Jung, S., Tiemann, E. & Lisdat, C. Cold atoms and molecules from fragmentation of decelerated SO_2. *Physical Review A* **74**, 040701 (2006).

54. Yamakita, Y., Procter, S., Goodgame, A., Softley, T. & Merkt, F. Deflection and deceleration of hydrogen Rydberg molecules in inhomogeneous electric fields. *The Journal of Chemical Physics* **121**, 1419–1431 (2004).

55. Hogan, S., Seiler, C. & Merkt, F. Rydberg-state-enabled deceleration and trapping of cold molecules. *Physical Review Letters* **103**, 123001 (2009).

56. Seiler, C., Hogan, S. & Merkt, F. Trapping cold molecular hydrogen. *Physical Chemistry Chemical Physics* **13**, 19000–19012 (2011).

57. Vanhaecke, N., Meier, U., Andrist, M., Meier, B. H. & Merkt, F. Multistage Zeeman deceleration of hydrogen atoms. *Physical Review A* **75**, 031402 (2007).

58. Hogan, S. D., Sprecher, D., Andrist, M., Vanhaecke, N. & Merkt, F. Zeeman deceleration of H and D. *Physical Review A* **76**, 023412 (2007).

59. Trimeche, A., Bera, M., Cromières, J. P., Robert, J. & Vanhaecke, N. Trapping of a supersonic beam in a traveling magnetic wave. *The European Physical Journal D-Atomic, Molecular, Optical and Plasma Physics* **65**, 263–271 (2011).

60. Narevicius, E. *et al.* An atomic coilgun: using pulsed magnetic fields to slow a supersonic beam. *New Journal of Physics* **9**, 358 (2007).

61. Narevicius, E. *et al.* Stopping supersonic beams with a series of pulsed electromagnetic coils: an atomic coilgun. *Physical Review Letters* **100**, 093003 (2008).

62. Narevicius, E. *et al.* Stopping supersonic beams with a series of pulsed electromagnetic coils: an atomic coilgun. *Physical Review Letters* **100**, 093003 (2008).

63. Hogan, S., Wiederkehr, A., Schmutz, H. & Merkt, F. Magnetic trapping of hydrogen after multistage Zeeman deceleration. *Physical Review Letters* **101**, 143001 (2008).

64. Fulton, R., Bishop, A., Shneider, M. & Barker, P. Controlling the motion of cold molecules with deep periodic optical potentials. *Nature Physics* **2**, 465–468 (2006).

65. Bishop, A., Wang, L. & Barker, P. Creating cold stationary molecular gases by optical Stark deceleration. *New Journal of Physics* **12**, 073028 (2010).

66. Barker, P. & Shneider, M. Slowing molecules by optical microlinear deceleration. *Physical Review A* **66**, 065402 (2002).

67. Coppendale, N., Wang, L., Douglas, P. & Barker, P. A high-energy, chirped laser system for optical Stark deceleration. *Applied Physics B* **104**, 569–576 (2011).

68. Maher-McWilliams, C., Douglas, P. & Barker, P. Laser-driven acceleration of neutral particles. *Nature Photonics* **6**, 386–390 (2012).

69. Weinstein, J. D., Guillet, T., Friedrich, B., Doyle, J. M. *et al.* Magnetic trapping of calcium monohydride molecules at millikelvin temperatures. *Nature* **395**, 148–150 (1998).

70. Schreck, F. *et al.* Sympathetic cooling of bosonic and fermionic lithium gases towards quantum degeneracy. *Physical Review A* **64**, 011402 (2001).

71. Modugno, G. *et al.* Bose-Einstein condensation of potassium atoms by sympathetic cooling. *Science* **294**, 1320–1322 (2001).

72. Willitsch, S., Bell, M. T., Gingell, A. D. & Softley, T. P. Chemical applications of laser-and sympathetically-cooled ions in ion traps. *Physical Chemistry Chemical Physics* **10**, 7200–7210 (2008).

73. Lara, M., Bohn, J. L., Potter, D., Soldán, P. & Hutson, J. M. Ultracold Rb-OH collisions and prospects for sympathetic cooling. *Physical Review Letters* **97**, 183201 (2006).

74. Soldán, P. & Hutson, J. M. Interaction of NH (X Σ-3) Molecules with Rubidium Atoms: Implications for Sympathetic Cooling and the Formation of Extremely Polar Molecules. *Physical Review Letters* **92**, 163202 (2004).

75. Barker, P. *et al.* Sympathetic cooling by collisions with ultracold rare gas atoms, and recent progress in optical Stark deceleration. *Faraday Discussions* **142**, 175–190 (2009).

76. Stas, R., McNamara, J., Hogervorst, W. & Vassen, W. Homonuclear ionizing collisions of laser-cooled metastable helium atoms. *Physical Review A* **73**, 032713 (2006).

77. Kuppens, S. *et al.* Approaching Bose-Einstein condensation of metastable neon: Over 10 9 trapped atoms. *Physical Review A* **65**, 023410 (2002).

78. Tychkov, A. *et al.* Metastable helium Bose-Einstein condensate with a large number of atoms. *Physical Review A* **73**, 031603 (2006).

79. Spoden, P. *et al.* Collisional properties of cold spin-polarized metastable neon atoms. *Physical Review Letters* **94**, 223201 (2005).

80. Busch, H. C., Shaffer, M. K., Ahmed, E. M. & Sukenik, C. I. Trap loss in a dual-species Rb-Ar* magneto-optical trap. *Physical Review A* **73**, 023406 (2006).

81. Katori, H. & Shimizu, F. Laser-Induced Ionizing Collisions of Ultracold Krypton Gas in the 1 s 5 Metastable State. *Physical Review Letters* **73**, 2555 (1994).

82. Walhout, M., Sterr, U., Orzel, C., Hoogerland, M. & Rolston, S. Optical control of ultracold collisions in metastable xenon. *Physical Review Letters* **74**, 506 (1995).

83. Vassen, W. *et al.* Cold and trapped metastable noble gases. *Reviews of Modern Physics* **84**, 175 (2012).

84. Barletta, P., Tennyson, J. & Barker, P. Creating ultracold molecules by collisions with ultracold rare-gas atoms in an optical trap. *Physical Review A* **78**, 052707 (2008).

85. Barletta, P., Tennyson, J. & Barker, P. Direct Monte Carlo simulation of the sympathetic cooling of trapped molecules by ultracold argon atoms. *New Journal of Physics* **12**, 113002 (2010).

86. van Veldhoven, J. *et al.* Decelerated molecular beams for high-resolution spectroscopy. *The European Physical Journal D-Atomic, Molecular, Optical and Plasma Physics* **31**, 337–349 (2004).

87. Gilijamse, J. J. *et al.* The radiative lifetime of metastable CO (aΠ3, v= 0). *The Journal of Chemical Physics* **127**, 221102 (2007).

88. van de Meerakker, S. Y., Vanhaecke, N., van der Loo, M. P., Groenenboom, G. C. & Meijer, G. Direct measurement of the radiative lifetime of vibrationally excited OH radicals. *Physical Review Letters* **95**, 013003 (2005).

89. Hudson, E. R., Lewandowski, H., Sawyer, B. C. & Ye, J. Cold molecule spectroscopy for constraining the evolution of the fine structure constant. *Physical Review Letters* **96**, 143004 (2006).

90. Kajita, M., Gopakumar, G., Abe, M. & Hada, M. Accuracy estimations of overtone vibrational transition frequencies of optically trapped 174 Yb 6 Li molecules. *Physical Review A* **85**, 062519 (2012).

91. Bolokhov, P. A., Pospelov, M. & Romalis, M. Electric dipole moments as probes of C P T invariance. *Physical Review D* **78**, 057702 (2008).

92. Baron, J. *et al.* Order of magnitude smaller limit on the electric dipole moment of the electron. *Science* **343**, 269–272 (2014).

93. Krems, R. V. Cold controlled chemistry. *Physical Chemistry Chemical Physics* **10**, 4079–4092 (2008).

94. Hutson, J. M. Ultracold chemistry. *Science.* **327**, 788–789 (2010).

95. Ospelkaus, S. *et al.* Quantum-state controlled chemical reactions of ultracold potassium-rubidium molecules. *Science* **327**, 853–857 (2010).

96. Gilijamse, J. J., Hoekstra, S., van de Meerakker, S. Y., Groenenboom, G. C. & Meijer, G. Near-threshold inelastic collisions using molecular beams with a tunable velocity. *Science* **313**, 1617–1620 (2006).

97. Sawyer, B. C., Stuhl, B. K., Wang, D., Yeo, M. & Ye, J. Molecular beam collisions with a magnetically trapped target. *Physical Review Letters* **101**, 203203 (2008).

98. Edmunds, P. D. & Barker, P. F. A deep optical cavity trap for atoms and molecules with rapid frequency and intensity modulation. *Review of Scientific Instruments* **84**, 083101 (2013).

99. Edmunds, P. D. & Barker, P. F. Trapping Cold Ground State Argon Atoms. *Physical Review Letters* **113**, 183001 (2014).

100. Metcalf, H. J. & Van der Straten, P. *Laser cooling and trapping* (Springer, 1999).

101. Dos Santos, F. P. *et al.* Bose-Einstein condensation of metastable helium. *Physical Review Letters* **86**, 3459 (2001).

102. Robert, A. *et al.* A Bose-Einstein condensate of metastable atoms. *Science* **292**, 461–464 (2001).

103. Ralchenko, Y., Kramida, A. & Reader, J. NIST atomic spectra database (version 4.0). *National Institute of Standards and Technology, Gaithersburg, MD* (2010).

104. Grimm, R., Weidemüller, M. & Ovchinnikov, Y. B. Optical dipole traps for neutral atoms. *Advances in atomic, molecular, and optical physics* **42**, 95–170 (2000).

105. Chen, C. *et al.* Beam of metastable krypton atoms extracted from a rf-driven discharge. *Review of Scientific Instruments* **72**, 271–272 (2001).

106. Sukenik, C. & Busch, H. A rf discharge cell for saturated absorption spectroscopy of metastable argon. *Review of Scientific Instruments* **73**, 493–494 (2002).

107. Maher-McWilliams, C. *Creation, trapping and manipulation of a cold argon gas.* Ph.D. thesis, University College London (2013).

108. Corwin, K. L., Lu, Z.-T., Hand, C. F., Epstein, R. J. & Wieman, C. E. Frequency-stabilized diode laser with the Zeeman shift in an atomic vapor. *Applied Optics* **37**, 3295–3298 (1998).

109. Stover, H. & Steier, W. Locking of laser oscillators by light injection. *Applied Physics Letters* **8**, 91–93 (1966).

110. Lang, R. Injection locking properties of a semiconductor laser. *Quantum Electronics, IEEE Journal of* **18**, 976–983 (1982).

111. Douglas, P., Maher-McWilliams, C. & Barker, P. Frequency stabilization of an external-cavity diode laser to metastable argon atoms in a discharge. *Review of Scientific Instruments* **83**, 063107 (2012).

112. Maguire, L., Szilagyi, S. & Scholten, R. High performance laser shutter using a hard disk drive voice-coil actuator. *Review of Scientific Instruments* **75**, 3077–3079 (2004).

113. Scholten, R. Enhanced laser shutter using a hard disk drive rotary voice-coil actuator. *Review of Scientific Instruments* **78**, 026101 (2007).

114. Lett, P. D. *et al.* Observation of atoms laser cooled below the Doppler limit. *Physical Review Letters* **61**, 169 (1988).

115. Schneble, D. *Trapping and manipulation of laser-cooled metastable argon atoms at a surface*. Ph.D. thesis, Universität Konstanz (2002).

116. Savard, T., Ohara, K. & Thomas, J. Laser-noise-induced heating in far-off resonance optical traps. *Physical Review A* **56**, R1095 (1997).

117. Gehm, M., Ohara, K., Savard, T. & Thomas, J. Dynamics of noise-induced heating in atom traps. *Physical Review A* **58**, 3914 (1998).

118. Griffin, P. F. *Laser Cooling and Loading of Rb into A Large Period, Quasi Electrostatic, Optical Lattice*. Ph.D. thesis, Durham University (2005).

119. Weatherill, K. J. *A CO_2 Laser Lattice Experiment for Cold Atoms*. Ph.D. thesis, Durham University (2007).

120. Gehm, M. E. *Preparation of an Optically-Trapped Degenerate Fermi Gas of 6Li - Finding the Route to Degeneracy*. Ph.D. thesis, Duke University (2003).

121. Friebel, S., Dandrea, C., Walz, J., Weitz, M. & Hänsch, T. CO 2-laser optical lattice with cold rubidium atoms. *Physical Review A* **57**, R20 (1998).

122. Wu, J., Newell, R., Hausmann, M., Vieira, D. J. & Zhao, X. Loading dynamics of optical trap and parametric excitation resonances of trapped atoms. *Journal of Applied Physics* **100**, 054903 (2006).

123. Chu, S., Bjorkholm, J. E., Ashkin, A. & Cable, A. Experimental Observation of Optically Trapped Atoms. *Physical Review Letters* **57**, 314–317 (1986).

124. Hood, C. J., Kimble, H. J. & Ye, J. Characterization of high-finesse mirrors: Loss, phase shifts, and mode structure in an optical cavity. *Physical Review A* **64**, 033804 (2001).

125. Hansch, T. & Couillaud, B. Laser frequency stabilization by polarization spectroscopy of a reflecting reference cavity. *Optics Communications* **35**, 441–444 (1980).

126. Black, E. D. An introduction to Pound–Drever–Hall laser frequency stabilization. *Am. J. Phys.* **69**, 79–87 (2001).

127. Drever, R. *et al.* Laser phase and frequency stabilization using an optical resonator. *App. Phys. B* **31**, 97–105 (1983).

128. Birkhoff, G. & Rota, G. *Ordinary Differential Equations* (Wiley, 1989).

129. Burkill, J. *The Theory of Ordinary Differential Equations* (Oliver and Boyd, 1956).

130. Watson, G. *Theory of Bessel Functions* (Cambridge Univ. Press, 1944).

131. Siddique, U., Aravantinos, V. & Tahar, S. Formal Stability Analysis of Optical Resonators. *NASA Formal Methods* **7871**, 368–382 (2013).

132. Kogelnik, H. & Li, T. Laser Beams and Resonators. *Appl. Opt.* **5**, 1550–1567 (1966).

133. Sylvester, J. J. *The collected mathematical papers of James Joseph Sylvester*, vol. 3 (Cambridge University Press, 2012).

134. Meschede, D. *Optics, light and lasers* (Wiley, 2008).

135. Meng, L. S., Brasseur, J. K. & Neumann, D. K. Damage threshold and surface distortion measurement for high-reflectance, low-loss mirrors to 100+ MW/cm2 cw laser intensity. *Opt. Express* **13**, 10085–10091 (2005).

136. Uehara, N. & Ueda, K. Accurate measurement of the radius of curvature of a concave mirror and the power dependence in a high-finesse Fabry—Perot interferometer. *Appl. Opt.* **34**, 5611–5619 (1995).

137. Degallaix, J., Zhao, C., Ju, L. & Blair, D. Thermal tuning of optical cavities for parametric instability control. *J. Opt. Soc. Am. B* **24**, 1336–1343 (2007).

138. Lee, S. K., Lee, H. S., Kim, J. M. & Cho, D. Optical dipole trap using a FabryPerot interferometer as a power buildup cavity. *J. Phys. B: At. Mol. Opt. Phys.* **38**, 1381 (2005).

139. Mosk, A. *et al.* Resonator-enhanced optical dipole trap for fermionic lithium atoms. *Opt. Lett.* **26**, 1837–1839 (2001).

140. Cruz, L. S., Sereno, M. & Cruz, F. C. Deep optical trap for cold alkaline-Earth atoms. *Opt. Express* **16**, 2909–2914 (2008).

141. Ricci, L. *et al.* A compact grating-stabilized diode laser system for atomic physics. *Optics Communications* **117**, 541–549 (1995).

142. Wieman, C. E. & Hollberg, L. Using diode lasers for atomic physics. *Review of Scientific Instruments* **62**, 1–20 (1991).

143. Camparo, J. The diode laser in atomic physics. *Contemporary Physics* **26**, 443–477 (1985).

144. Meschede, D. *Optics, light and lasers: the practical approach to modern aspects of photonics and laser physics* (John Wiley & Sons, 2008).

145. Damjanovic, D. Hysteresis in piezoelectric and ferroelectric materials. *The Science of Hysteresis* **3**, 337–465 (2006).

146. Poirson, J., Bretenaker, F., Vallet, M. & Le Floch, A. Analytical and experimental study of ringing effects in a Fabry–Perot cavity. Application to the measurement of high finesses. *JOSA B* **14**, 2811–2817 (1997).

147. Morville, J., Romanini, D., Kachanov, A. & Chenevier, M. Two schemes for trace detection using cavity ringdown spectroscopy. *Applied Physics B* **78**, 465–476 (2004).

148. Brossel, J. Multiple-beam localized fringes: Part I.-Intensity distribution and localization. *Proceedings of the Physical Society* **59**, 224 (1947).

149. Greig, J. & Cooper, J. Rapid scanning with the Fabry-Perot etalon. *Applied Optics* **7**, 2166–2170 (1968).

150. Dangor, A. & Fielding, S. The response of the Fabry-Perot interferometer to rapid changes in optical length. *Journal of Physics D: Applied Physics* **3**, 413 (1970).

151. Li, Z., Bennett, R. & Stedman, G. Swept-frequency induced optical cavity ringing. *Optics Communications* **86**, 51–57 (1991).

152. Li, Z., Stedman, G. & Bilger, H. Asymmetric response profile of a scanning Fabry-Perot interferometer. *Optics Communications* **100**, 240–246 (1993).

153. Layer, H. P. Acoustooptic Modulator Intensity Servo. *Appl. Opt.* **18**, 2947–2949 (1979).

154. Katori, H. & Shimizu, F. Laser cooling and trapping of argon and krypton using diode lasers. *Japanese Journal of Applied Physics* **29**, L2124 (1990).

155. Lee, S. K., Han, B. W. & Cho, D. Automatic system to relock a laser frequency to a Fabry–Perot cavity. *Review of Scientific Instruments* **76**, 026101 (2005).

156. Horak, P., Hechenblaikner, G., Gheri, K. M., Stecher, H. & Ritsch, H. Cavity-induced atom cooling in the strong coupling regime. *Physical Review Letters* **79**, 4974 (1997).

157. Barker, P. & Shneider, M. Cavity cooling of an optically trapped nanoparticle. *Physical Review A* **81**, 023826 (2010).

158. Siegman, A. E. Lasers University Science Books. *Mill Valley, CA* **37** (1986).

159. Molof, R. W., Schwartz, H. L., Miller, T. M. & Bederson, B. Measurements of electric dipole polarizabilities of the alkali-metal atoms and the metastable noble-gas atoms. *Physical Review A* **10**, 1131 (1974).

160. Loh, H. *et al.* Precision Spectroscopy of Polarized Molecules in an Ion Trap. *Science* **342**, 1220–1222 (2013).

161. Henson, A., Gersten, S., Shagam, Y., Narevicius, J. & Narevicius, E. Observation of resonances in Penning ionization reactions at sub-Kelvin temperatures in merged beams. *Science* **338**, 234–238 (2012).

162. Micheli, A., Brennen, G. & Zoller, P. A toolbox for lattice-spin models with polar molecules. *Nature Physics* **2**, 341–347 (2006).

163. André, A. *et al.* A coherent all-electrical interface between polar molecules and mesoscopic superconducting resonators. *Nature Physics* **2**, 636–642 (2006).

164. Barletta, P., Tennyson, J. & Barker, P. Towards sympathetic cooling of large molecules: cold collisions between benzene and rare gas atoms. *New Journal of Physics* **11**, 055029 (2009).

165. McNamara, J., Jeltes, T., Tychkov, A., Hogervorst, W. & Vassen, W. Degenerate Bose-Fermi mixture of metastable atoms. *Physical Review Letters* **97**, 080404 (2006).

166. Eichhorn, M., Mudrich, M., Weidemüller, M. *et al.* Optical dipole trap inside a laser resonator. *Opt. lett.* **29**, 1147–1149 (2004).

167. Blythe, P., Roth, B., Fröhlich, U., Wenz, H. & Schiller, S. Production of ultracold trapped molecular hydrogen ions. *Physical Review Letters* **95**, 183002 (2005).

168. Vuletić, V., Chin, C., Kerman, A. J. & Chu, S. Degenerate Raman sideband cooling of trapped cesium atoms at very high atomic densities. *Physical Review Letters* **81**, 5768 (1998).

169. Poli, N., Brecha, R., Roati, G. & Modugno, G. Cooling atoms in an optical trap by selective parametric excitation. *Physical Review A* **65**, 021401 (2002).

170. Knight, R. & Wang, L.-g. Stark-induced 6s-6d transitions in xenon. *Physical Review A* **32**, 2751 (1985).

171. Zhang, Z., Shneider, M. N., Zaidi, S. H. & Miles, R. B. Experiments on microwave scattering of REMPI in argon, xenon and nitric oxide. In *38th AIAA Plasmadynamics and Lasers Conference In conjunction with the 16th International Conference on MHD Energy Conversion* (2007).

172. Grucker, J. *et al.* Study of low-energy resonant metastability exchange in argon by a pulsed merging beam technique. *Journal of Physics B: Atomic, Molecular and Optical Physics* **41**, 021001 (2008).

173. Batz, M., Nacher, P.-J. & Tastevin, G. Fundamentals of metastability exchange optical pumping in helium. In *Journal of Physics: Conference Series*, vol. 294, 012002 (IOP Publishing, 2011).

174. Robert, J., Bocvarski, V., Colomb de Daunant, I., Vassilev, G. & Baudon, J. n. *J. Phys.* **45**, 225–237 (1984).

175. Kasai, S., Mizutani, R., Kondo, R., Hasuo, M. & Fujimoto, T. Dynamics of metastable argon atoms in a thin discharge cell: Single beam absorption spectroscopy and a Monte Carlo study of the velocity distribution. *Journal of the Physical Society of Japan* **72**, 1936–1942 (2003).

176. Kolts, J. & Setser, D. Decay rates of Ar (4s, 3P2), Ar (4s′, 3P0), Kr (5s, 3P2), and Xe (6s, 3P2) atoms in argon. *The Journal of Chemical Physics* **68**, 4848–4859 (1978).

177. Tachibana, K. Excitation of the 1s5, 1s4, 1s3, and 1s2 levels of argon by low-energy electrons. *Physical Review A* **34**, 1007 (1986).

178. Bogaerts, A. & Gijbels, R. Modeling of metastable argon atoms in a direct-current glow discharge. *Physical Review A* **52**, 3743 (1995).

179. Corduneanu, C. *Principles of differential and integral equations*, vol. 295 (American Mathematical Soc., 2008).

180. Hartman, P. *Ordinary Differential Equations* (Society for Industrial and Applied Mathematics, 2002).

181. Mudrich, M. *Interactions in an optically trapped mixture of ultracold lithium and cesium atoms: Thermalization, spin-exchange collisions and photoassociation.* Ph.D. thesis, Ruperto-Carola University (2003).

182. Delannoy, G. *et al.* Understanding the production of dual Bose-Einstein condensation with sympathetic cooling. *Physical Review A* **63**, 051602 (2001).

183. Jáuregui, R., Poli, N., Roati, G. & Modugno, G. Anharmonic parametric excitation in optical lattices. *Physical Review A* **64**, 033403 (2001).

184. Molof, R. W., Schwartz, H. L., Miller, T. M. & Bederson, B. Measurements of electric dipole polarizabilities of the alkali-metal atoms and the metastable noble-gas atoms. *Physical Review A* **10**, 1131–1140 (1974).

185. Mitroy, J., Safronova, M. & Clark, C. W. Theory and applications of atomic and ionic polarizabilities. *J. Phys. B: At. Mol. Opt. Phys.* **43**, 202001 (2010).

186. Beardmore, J., Palmer, A. J., Kuiper, K. & Sang, R. A hexapole magnetic guide for neutral atomic beams. *Review of Scientific Instruments* **80**, 073105 (2009).

187. Dieckmann, K., Spreeuw, R., Weidemüller, M. & Walraven, J. Two-dimensional magneto-optical trap as a source of slow atoms. *Physical Review A* **58**, 3891 (1998).

188. Scholz, A., Christ, M., Doll, D., Ludwig, J. & Ertmer, W. Magneto-optical preparation of a slow, cold and bright Ne* atomic beam. *Optics Communications* **111**, 155–162 (1994).

189. van Drunen, W. J. *Collisional interaction between metastable neon atoms*. Ph.D. thesis, Technische Universität Darmstadt (2008).

190. Fedichev, P., Reynolds, M., Rahmanov, U. & Shlyapnikov, G. Inelastic decay processes in a gas of spin-polarized triplet helium. *Physical Review A* **53**, 1447 (1996).

191. Kocsis, S. *et al.* Observing the average trajectories of single photons in a two-slit interferometer. *Science* **332**, 1170–1173 (2011).

192. Millen, J., Deesuwan, T., Barker, P. & Anders, J. Nanoscale temperature measurements using non-equilibrium Brownian dynamics of a levitated nanosphere. *Nature nanotechnology* (2014).

193. Pender, G., Barker, P., Marquardt, F., Millen, J. & Monteiro, T. Optomechanical cooling of levitated spheres with doubly resonant fields. *Physical Review A* **85**, 021802 (2012).

194. Monteiro, T. *et al.* Dynamics of levitated nanospheres: towards the strong coupling regime. *New Journal of Physics* **15**, 015001 (2013).

195. Camerer, S. *et al.* Realization of an optomechanical interface between ultracold atoms and a membrane. *Physical Review Letters* **107**, 223001 (2011).